

# Atmospheric calibration for sub-millimeter radio astronomy

Inaugural-Dissertation  
zur  
Erlangung des Doktorgrades  
der Mathematisch-Naturwissenschaftlichen Fakultät der  
Universität zu Köln

vorgelegt von  
**Guan, Xin**  
aus Beijing

Köln 2016

Berichtersteller:

Prof. Dr. Jürgen Stutzki

Prof. Dr. Susanne Crewell

Tag der mündlichen Prüfung: 21 Januar 2016

# Contents

1	<i>Introduction</i>	9
1.1	<i>Background</i>	9
1.2	<i>Application field</i>	10
1.3	<i>Sub-millimeter observatories overview</i>	13
1.4	<i>Calibration for atmospheric attenuation</i>	16
2	<i>Static atmospheric model</i>	23
2.1	<i>Ranges of the physical parameters of the atmosphere</i>	24
2.2	<i>The layered atmosphere, atmospheric effects</i>	25
2.3	<i>Water vapor vertical distribution</i>	26
2.4	<i>Ozone vertical distribution</i>	27
2.5	<i>CO vertical distribution</i>	28
2.6	<i>Atomic oxygen in the atmosphere</i>	29
2.7	<i>N<sub>2</sub> and O<sub>2</sub></i>	30
2.8	<i>N<sub>2</sub>O vertical distribution</i>	30
2.9	<i>Minor absorbers</i>	31
2.10	<i>The P-T profile</i>	31
2.11	<i>Validity of the static atmospheric model</i>	32
3	<i>Radiative transfer model</i>	33
3.1	<i>ATM</i>	34
3.2	<i>ATRAN</i>	35

3.3	<i>MOLIERE</i>	37
3.4	<i>AM</i>	38
3.5	<i>Choice of radiative transfer models</i>	41
4	<i>The calibration procedure</i>	43
4.1	<i>The calibration workflow</i>	43
4.2	<i>Calibration in different observing modes</i>	44
5	<i>Application to NANTEN2 / SMART</i>	51
5.1	<i>Performance characteristics of SMART</i>	51
5.2	<i>NANTEN2 / SMART specific considerations for the static atmospheric model</i>	52
5.3	<i>NANTEN2 / SMART specific considerations for the radiative transfer model</i>	56
5.4	<i>Application of kalibrate to NANTEN2 / SMART</i>	57
5.5	<i>Receiver stability: Test and effect</i>	58
5.6	<i>Effect of forward efficiency error on calibration</i>	60
5.7	<i>Effect of load temperature error on calibration</i>	61
5.8	<i>Effect of using the atm-table to compute radiative transfer</i>	62
5.9	<i>Conclusion</i>	63
6	<i>Application to SOFIA / GREAT</i>	65
6.1	<i>Performance characteristics of GREAT</i>	65
6.2	<i>SOFIA / GREAT specific considerations for the static atmospheric model</i>	66
6.3	<i>SOFIA / GREAT specific considerations for the radiative transfer model</i>	71
6.4	<i>Application of kalibrate to SOFIA / GREAT</i>	72
6.5	<i>Summary</i>	80
7	<i>Summary and outlook</i>	83
	<i>Appendices</i>	87

<i>A</i>	<i>Additional figures for Chapter 5</i>	89
<i>B</i>	<i>Additional figures for Chapter 6</i>	99
<i>C</i>	<i>Program structure of kalibrate</i>	121
<i>D</i>	<i>OpenCL support of the AM atmospheric model</i>	125
	<i>Bibliography</i>	129

# *Abstract*

This thesis is focused on improving the calibration accuracy of sub-millimeter astronomical observations. The wavelength range covered by observational radio astronomy has been extended to sub-millimeter and far infrared with the advancement of receiver technology in recent years. Sub-millimeter observations carried out with airborne and ground-based telescopes typically suffer from 10% to 90% attenuation of the astronomical source signals by the terrestrial atmosphere. The amount of attenuation can be derived from the measured brightness of the atmospheric emission. In order to do this, the knowledge of the atmospheric temperature and chemical composition, as well as the frequency-dependent optical depth at each place along the line of sight is required. The altitude-dependent air temperature and composition are estimated using a parametrized static atmospheric model, which is described in Chapter 2, because direct measurements are technically and financially infeasible. The frequency dependent optical depth of the atmosphere is computed with a radiative transfer model based on the theories of quantum mechanics and, in addition, some empirical formulae. The choice, application, and improvement of third party radiative transfer models are discussed in Chapter 3.

The application of the calibration procedure, which is described in Chapter 4, to the astronomical data observed with the SubMillimeter Array Receiver for Two Frequencies (SMART), and the German REceiver for Astronomy at Terahertz Frequencies (GREAT), is presented in Chapters 5 and 6. The brightnesses of atmospheric emission were fitted consistently to the simultaneous multi-band observation data from GREAT at  $1.2 \sim 1.4$  and  $1.8 \sim 1.9$  THz with a single set of parameters of the static atmospheric model. On the other hand, the cause of the inconsistency between the model parameters fitted from the 490 and 810 GHz data of SMART is found to be the lack of calibration of the effective cold load temperature.

Besides the correctness of atmospheric modeling, the stability of the receiver is also important to achieving optimal calibration accuracy. The stabilities of SMART and GREAT are analyzed with a special calibration procedure, namely the "load calibration". The effects of the drift and fluctuation of the receiver gain and noise temperature on calibration accuracy are discussed in Chapters 5 and 6. Alternative observing strategies are proposed to combat receiver instability.

The methods and conclusions presented in this thesis are applicable to the atmospheric calibration of sub-millimeter astronomical observations up to at least 4.7 THz (the H channel frequency of GREAT) for observations carried out from  $\sim 4$  to 14 km altitude. The procedures for receiver gain calibration and stability test are applicable to other instruments using the same calibration approach as that for SMART and GREAT.

The structure of the high performance, modular, and extensible calibration program used and further developed for this thesis work is presented in the Appendix C.

# Zusammenfassung

Das Ziel der hier vorliegenden Arbeit ist es die Kalibrationsgenauigkeit von astronomischen Beobachtungen im sub-millimeter Bereich zu verbessern. Der Wellenlängenbereich, der durch die beobachtende Radioastronomie abgedeckt wird, wurde in den letzten Jahren durch Fortschritte in der Empfänger-Technologie in den sub-millimeter und Ferninfrarot Bereich ausgedehnt. Sub-millimeter Beobachtungen an luft- und bodengestützten Teleskopen erleiden typischerweise 10% bis 90% Abschwächung des Signals der astronomischen Quelle durch die Erdatmosphäre. Der Umfang der Abschwächung kann aus der gemessenen Helligkeit der atmosphärischen Emission bestimmt werden. Um dies zu ermöglichen, benötigen wir Kenntnis über die Atmosphärentemperatur, die chemische Zusammensetzung, aber auch die frequenzabhängige optische Tiefe an jeder Stelle entlang der Sichtlinie. Die Höhenabhängigkeit der Temperatur und Zusammensetzung der Atmosphäre werden mit Hilfe von parametrisierten, statischen Atmosphärenmodellen abgeschätzt, die in Kapitel 2 beschrieben werden, da direkte Messungen aus technischen und finanziellen Gründen nicht durchführbar sind. Die frequenzabhängige optische Tiefe der Atmosphäre wird mit einem Strahlungstransportmodell basierend auf den Theorien der Quantenmechanik und einigen empirischen Formeln berechnet. Die Wahl, Anwendung und Verbesserung von Strahlungstransportmodellen von Dritten werden in Kapitel 3 diskutiert.

Die Anwendung der Kalibrationsprozedur, beschrieben in Kapitel 4, auf astronomische Daten, die mit dem SubMillimeter Array Receiver for Two Frequencies (SMART) und dem German REceiver for Astronomy at Terahertz Frequencies (GREAT) beobachtet wurden, ist in den Kapiteln 5 und 6 dargestellt. Die Helligkeiten der atmosphärischen Emission wurden konsistent mit einem einzigen Satz von Parametern des statischen Atmosphärenmodells an die simulierten beobachteten multi-band Daten von GREAT bei  $1.2 \sim 1.4$  und  $1.8 \sim 1.9$  THz gefittet. Die Ursache der Inkonsistenz von Modellparametern der 490 und 810 GHz Daten von SMART liegt dagegen in der mangelnden Kalibration der effektiven cold load Temperatur.

Neben der Korrektheit der atmosphärischen Modelle ist auch die Stabilität des Empfängers entscheidend für das Erreichen einer optimalen Kalibrationsgenauigkeit. Die Stabilitäten von SMART und GREAT werden mit einer speziellen Kalibrationsmethode, der sogenannten "load calibration", analysiert. Die Effekte von drift und Fluktuationen des Empfänger-gains und der Empfänger-Rauschtemperatur auf die Kalibrationsgenauigkeit werden in den Kapiteln 5 und 6 diskutiert. Alternative Beobachtungsstrategien zur Bekämpfung von Empfänger-Instabilitäten werden vorgeschlagen.

Die in dieser Arbeit vorgestellten Methoden und Schlussfolgerungen sind auf die atmosphärische Kalibration von astronomischen sub-millimeter Beobachtungen bis mindestens hinauf zu 4.7 THz (der H Kanal Frequenz von GREAT) und für Beobachtungen aus  $\sim 4$  bis 14 km Höhe anwendbar. Die Methoden zur Kalibration des Empfänger-gains und zum Test der Empfänger-Stabilität sind auch für andere Instrumente anwendbar, die den gleichen Kalibrationsansatz wie SMART und GREAT benutzen.

Die Struktur des hoch leistungsfähigen, modularen und erweiterbaren Kalibrationsprogramms, das in dieser Arbeit benutzt und weiter entwickelt wurde, wird in Appendix C vorgestellt.



# 1

## Introduction

This thesis studies the calibration of sub-millimeter and far infrared astronomical data in order to compensate for the extinction caused by the terrestrial atmosphere. In particular, the methods developed during this thesis work have been applied extensively to data calibration and receiver stability analysis from 0.43 to 4.7 THz for one ground based and one airborne observatory. The wavelength ranges of sub-millimeter and far infrared are collectively referred to as sub-millimeter or sub-mm in the following text according to the current convention of the field of observational astronomy due to the fact that similar receiver technologies are used in both cases.

### 1.1 Background

Radio astronomy is the subfield of astronomy that studies celestial objects through their electromagnetic emission using radio techniques<sup>1</sup>, and covers frequencies up to several Terahertz, which are referred to as *radio frequencies* hereinafter. Recent advancement in mixer engineering (Pütz et al., 2013; Graf et al., 2015) made it possible to do heterodyne observations up to 4.74 THz. The energy range of radio frequency photons covers a great number of molecular lines as well as some atomic lines<sup>2</sup>. Therefore, many astrophysical processes can be studied through the observation of celestial objects with radio telescopes. Some of these spectral lines are blocked by atmospheric attenuation, and can only be observed from space. The frequency bands containing these lines that are located between the strong absorption lines of the atmosphere (referred to as the "atmospheric windows" hereinafter) are of particular interest to the study of the astronomical problems such as star formation, evolution of the interstellar medium, and so on. This can be done with the vast majority of sub-mm telescopes that are ground based or airborne<sup>3</sup>.

Although ground-based and airborne sub-mm telescopes suffer from non-negligible attenuation by the terrestrial atmosphere, they

<sup>1</sup> All receivers referred to in this thesis are heterodyne receivers.

<sup>2</sup> There are many sub-millimeter (sub-mm) spectral lines useful to astronomical study, including the rotational lines of CO, the atomic lines of carbon, nitrogen, and oxygen, fine structure lines, and so on. Their frequencies are available from e.g., the "Cologne Database for Molecular Spectroscopy" (Müller et al., 2001, 2005), the "Recommended rest frequencies" database (Lovas, 2004), and etc.

<sup>3</sup> Space telescopes, which are important tools because they are not affected by atmospheric attenuation, and Balloonborne telescopes (Pascale, 2012, and etc.) that operate in the stratosphere above most of the atmospheric water vapor and ozone are out of the scope of this thesis. Only ground based and airborne sub-mm telescopes are discussed below.

have their virtues compared to balloon-borne and space telescopes. The weight, size, and power supply limitations of the payload of high altitude balloons and spacecrafts make it difficult to deploy large telescopes which have better resolution and sensitivity. The planning and launching of space telescopes, usually consume a lot of time and resources. Space telescopes are also hard to service and impossible (or very expensive) to upgrade. Together with the long lead time, this prevents space telescopes from keeping in pace with the advancement of sub-mm and terahertz receiver technology.

In order to use the advantages of ground-based and airborne telescopes, it is necessary to correct for atmospheric attenuation after proper calibration of the received signal. Various studies of receiver calibration and atmospheric calibration had been carried out by, e.g., Kutner and Ulich (1981); Downes (1989), and Paine (2014). This thesis extends the study and application of atmospheric modeling into the high frequency (up to 4.7 THz) and high altitude (4~14 km) range and discuss with sub-mm specific astronomical calibration.

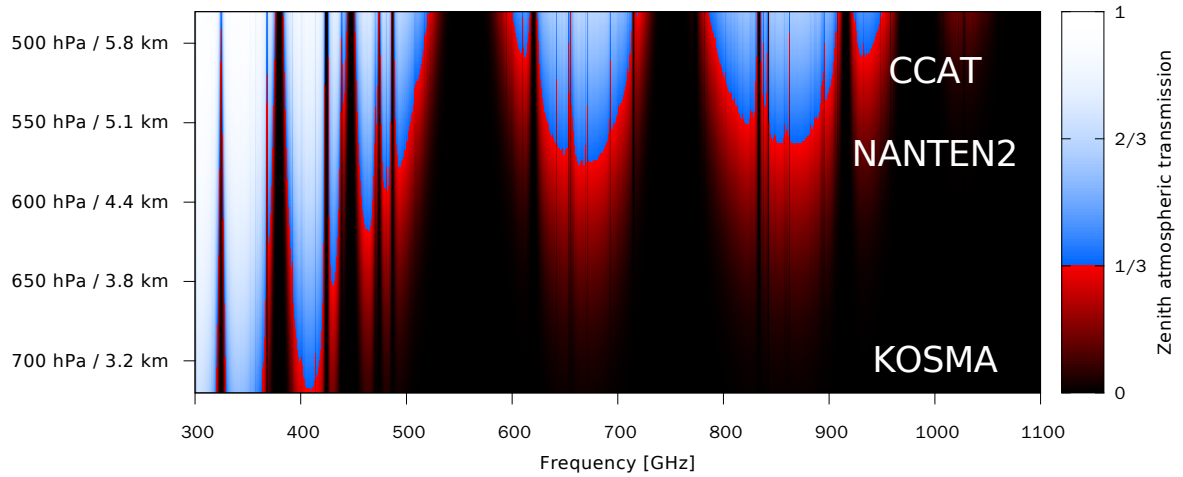
## 1.2 Application field

The main instruments involved in this thesis are heterodyne receivers, i.e. the SMART receiver (Graf et al., 2008) at the 4-meter NANTEN2 telescope (Kawamura et al., 2005) and the GREAT receiver (Heyminck et al., 2012) onboard the 2.5-meter SOFIA (Gehrz and Becklin, 2010). The NANTEN2 telescope in the Atacama desert is jointly operated by University of Cologne, Nagoya University, and others. The SMART receiver developed by University of Cologne has two arrays, each one having eight pixels in a  $2 \times 4$  layout, that operate at 460 ~ 490 and 800 ~ 880 GHz, respectively. In contrast to NANTEN2, SOFIA is an airborne telescope that works at variable altitudes around the tropopause<sup>4</sup>. One of the instruments onboard SOFIA is GREAT, the principal-investigator class multi-band heterodyne receiver that operates at 1.2 ~ 4.7 THz.

For ground based sub-mm observations, the attenuation through atmospheric windows is typically a fraction, but sometimes can be over ~95% of the source signal, as shown in Figure 1.1. (Absorption that is greater than 95% can be normal in, e.g., some ground-based water maser observations.) The amount of correction by atmospheric calibration is thus on the order of  $10^{-1}$ , and up to  $10^2$  in extreme cases. Because radio astronomy projects often aim at an accuracy of a few percent, the same or better accuracy must be achieved during atmospheric calibration.

The knowledge of atmospheric absorption features in certain weather conditions and geographical locations is not only neces-

<sup>4</sup> Despite of its name being the "Stratospheric Observatory for Infrared Astronomy", SOFIA's design goal was to avoid most of the atmospheric water vapor, therefore sometimes does not need to fly over the tropopause. Typical flight altitudes of SOFIA range from 11 to 13.5 km.



sary for postprocessing of observational data, but also helpful to observations planning – For SOFIA / GREAT observations, it helps us to avoid the crowded absorption lines (as shown in Figure 1.2) by choosing either a proper time of observation when the spectral line from the astronomical source Doppler-shifts away from the atmospheric line, or an adequate flight altitude for good enough atmospheric transmission. The same knowledge is also required by site selection of ground based sub-mm observatories for evaluating the weather quality regarding astronomical observation. Literature and web resources on the topic of atmospheric transmission and site survey are widely available, e.g., Tremblin et al. (2012), Schneider et al. (2009), and the online tool <http://irfu.cea.fr/submm>.

The methods in this thesis are intended for daily use at NANTEN2, SOFIA, and KOSMA. The results are also applicable to the future CCAT (Sebring et al., 2006) or other sub-mm observatories at similar altitudes, but must be validated before use at frequencies and altitudes out of the ranges mentioned herein.

Figure 1.1: Zenith atmospheric transmission above different altitudes computed for three ground-based sub-mm telescopes: KOSMA, NANTEN2, and the future CCAT, under typical weather conditions.

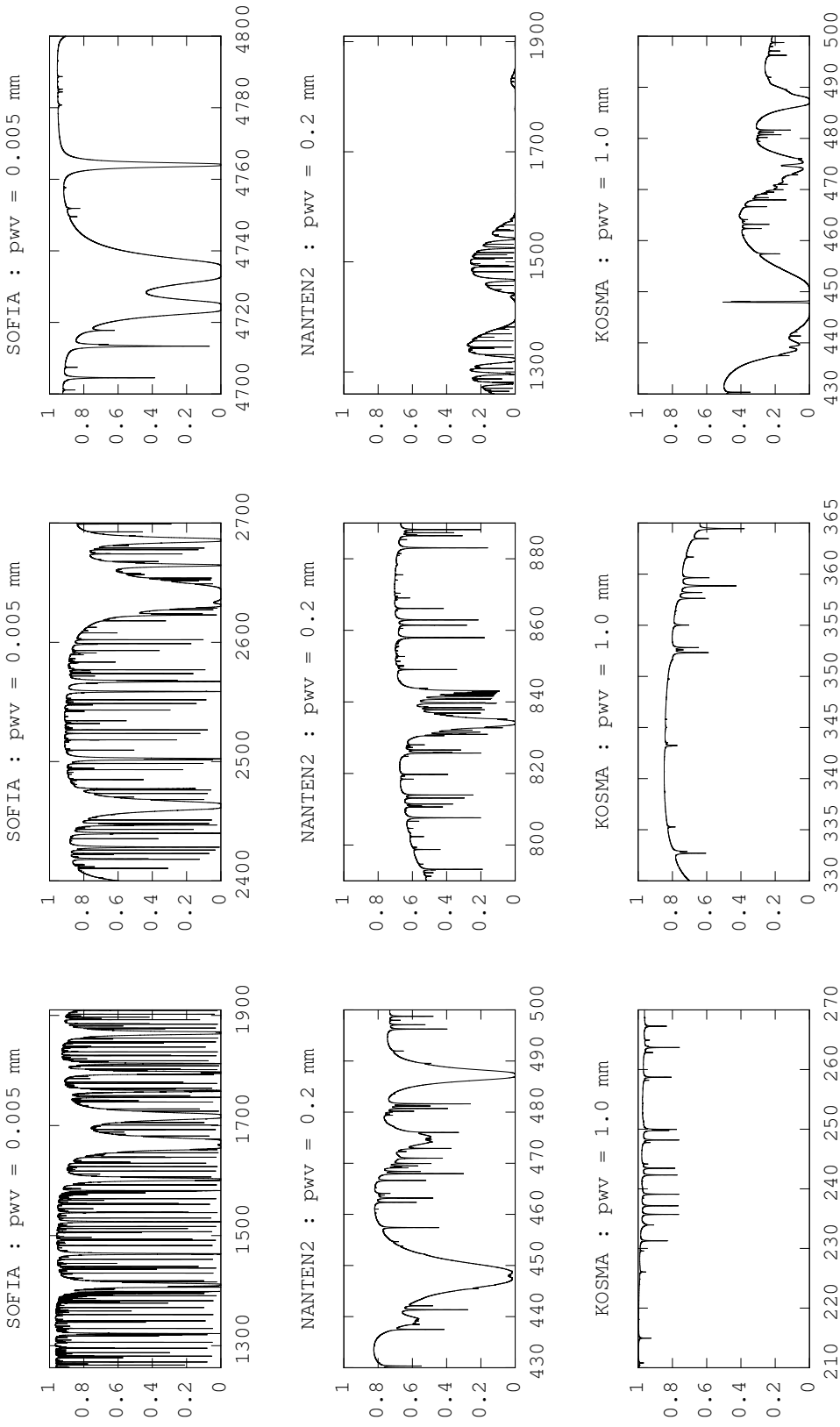


Figure 1.2: Typical atmospheric transmission curves for KOSMA (lower panels, 3.2 km site altitude), NANTEN2 (middle panels, 4.8 km) and SOFIA (upper panels, 12.5 km). Horizontal axis: frequency [GHz]; Vertical axis: atmospheric transmission. The atmospheric transmission is poor from 430 to 500 GHz at KOSMA, and from 1.26 to 1.91 THz at NANTEN2. Observations in these bands should be carried out at higher altitudes. The transmission curves are produced by the AM atmospheric model (Paine, 2014) with a static atmospheric model described in Chapter 2.

### 1.3 Sub-millimeter observatories overview

The working frequencies of a sub-mm observatory are mainly determined by the requirements of astrophysical research, and the location of the observatory is chosen so that the atmospheric transmission is reasonably good during a period that is long enough in each year<sup>5</sup>. The forward beam pattern of a telescope at a given frequency comprises the main beam and the error beams, which include the side lobes, the errors resulting from the precision of the mirror geometry, etc. Because the measurements of the complete forward beam patterns are not available for the telescopes that we use, this thesis takes it for granted that all of the sky emission is picked up from directions near, and including the main beam. In order to achieve higher angular resolution and sensitivity, large aperture (at least a few meters) of the telescopes are widely used in radio astronomy. The sizes of their main beams (Figure 1.3) are no more than two arc minutes at the sub-mm wavelength, which are negligible for the study of atmospheric calibration that aims at a precision of a few percent.

<sup>5</sup> Although observations that are carried out under an atmospheric transmission of a few percent can be calibrated with precision when using some of today's best astronomical receivers, the astronomical community is usually reluctant to spending time for that because most large sub-mm telescopes are shared and not dedicated devices.

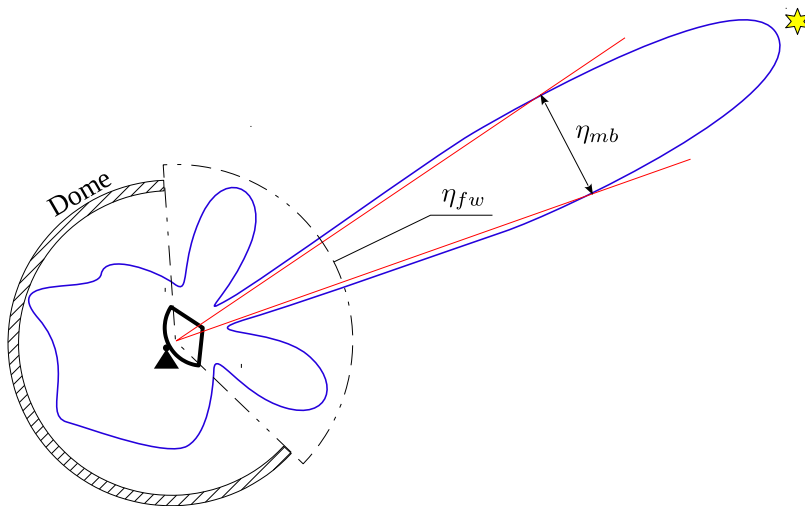


Figure 1.3: Sketch of a radio telescope's beam pattern (blue). The main beam, which is within the half power beam width (red), accounts for  $\eta_{mb}$  part of the total signal pick up. The forward efficiency or  $\eta_{fw}$  is the telescope's coupling factor to the sky. This thesis follows the same convention as that by Hiyama (1998).

The atmospheric transmission along the line of sight varies with the elevation of the telescope because of different line of sight air-masses. In radio astronomy, the telescope's elevation, or El for short, is defined as  $90^\circ$  minus the zenith angle.

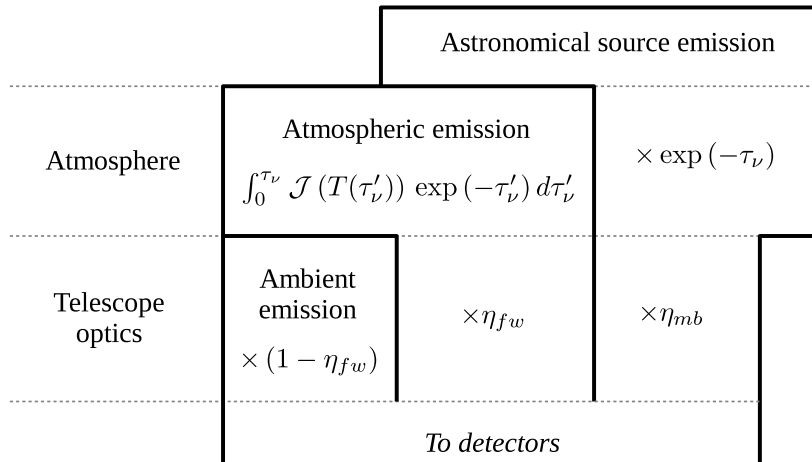
Observations are usually done at an elevation between about 20 and 80 degrees except in the cases that the source never rises high enough above horizon. This elevation range is preferred for better time efficiency. The time efficiency is given by the observing time needed to achieve a given S/N ratio of the source signal. The total

observing time is roughly in direct proportion to the integration time, or exposure time on the source<sup>6</sup>. Because the level of random noise is inversely proportional to the square root of integration time, and the received source signal is proportional to the atmospheric transmission, the required observing time will be

$$t_{obs} \propto \exp(-2 \tau_{v,zenith} / \sin(El)), \quad (1.1)$$

where  $\tau_{v,zenith}$  is the optical depth through the atmosphere towards the zenith, whose value is the logarithm of the ratio of incident to transmitted radiant power, and equals to the integral of absorption coefficient (scattering is ignored). The choice of observing frequency usually ensures that the optical depth along the telescope's line of sight is often less than unity, and rarely rises above two in order to observe efficiently. The optical depth is proportional to  $1/\sin(El)$  at a given zenith opacity. In *kalibrate*<sup>7</sup>, the term airmass is defined as  $1/\sin(El)$ .

The refraction of sub-mm waves by the atmosphere increases with decreasing elevation. For observations close to the horizon ( $El \gtrsim 0^\circ$ ), the refraction can reach up to a few arc minutes, which is comparable to or a little larger than the beam width. Although this is a considerable amount for pointing corrections, it can be safely ignored for atmospheric calibration because the targeted calibration accuracy is much more relaxed (a few percent), and there are a number of more significant sources of errors as shown in Chapters 5 and 6. The absorption and scattering by clouds are not considered.



After passing through the atmosphere, the source signal will be collected by the telescope and fed into the detectors (Figure 1.4). Some telescopes, such as the NANTEN2 and KOSMA, are protected

<sup>6</sup> The rest of the observing time is counted as overhead.

<sup>7</sup> *Kalibrate* is the calibration utility in *KOSMA Software*. *KOSMA Software* is a software collection that is used to control the following telescope and receivers: KOSMA with the DualSIS receiver, NANTEN2 when using SMART, and SOFIA when using GREAT and upGREAT.

Figure 1.4: Signal path of a telescope for the source signal, atmospheric emission, and ambient emission. Each signal is coupled to the detectors with a different coupling factor  $\eta$ . The source signal in addition suffers from an atmospheric attenuation of  $\exp(-\tau_\nu)$ . It is assumed that the source fills up the main beam, which may not be the true for compact sources.

by a PTFE membrane of a few millimeters' thickness against snow, dust, and direct sunlight (which may cause overheating). The transmission curve of this membrane is flat enough within the receiver passband. The effect of this protection is therefore equivalent to a decreased main beam and forward efficiency. The same applies to other kind of losses of the telescope optics. Both the forward efficiency ( $\eta_{fw}$ ) and the main beam efficiency ( $\eta_{mb}$ ) in Figure 1.4 are dependent on frequency and elevation, besides other mechanical parameters, and are "effective" values (instead of geometric parameters) that have already taken the losses introduced by the foil and telescope optics into account.

Through the optical path described above, the sky signal, including the emission from the astronomical source, the terrestrial atmosphere, and the ambient material, reaches the detector, i.e the first mixer of the heterodyne receiving system, where it is down converted to an intermediate frequency (IF). The mixer may have a non-unity ratio of gains between the signal and image sidebands. While sideband separation may be as high as e.g., 10 dB or more for some receivers (Carter et al., 2012), both of the SMART and GREAT instruments are typical double-sideband receivers that have a sideband ratio near unity.

The IF signal from the mixer output is amplified and / or processed by a second frequency converter, and then fed into the spectrometers. The receiver system in the signal path before the first IF stage is referred to as the frontend, which includes the mixer and the local oscillator (LO) electronics and optics. In this thesis, "backend" refers to the spectrometer, though it also includes a secondary frequency conversion stage in some context.

The 88.5 kHz frequency resolution of our spectroscopic data<sup>8</sup> is far beyond the widths of the narrowest atmospheric lines ( $\sim 500$  kHz) in our observation data. The level of spurious spectrum, which is caused by the non-linearity of analog-to-digital conversion, is about 0.2% of the signal level according to Radiometer-Physics GmbH (2011). At a typical receiver noise level of  $\sim 3 \times 10^3$  K for the GREAT L channel receivers, and a maximum sky brightness on the order of  $2 \times 10^2$  K, this typically translates to an error of a few K in the measured brightness of atmospheric emission:

$$\Delta T_{sky} \approx \frac{T_{sky}}{\text{SFDR}} \cdot \left[ \left( 1 + \frac{T_{sky}}{T_{rec}} \right)^n - 1 \right], \quad (1.2)$$

where SFDR is the spurious-free dynamic range of the spectrometer, and  $n$  is the order of the strongest harmonics. There is no other limitation by the spectrometer for use in atmospheric modeling.

<sup>8</sup> This is actually the resolution of the spectrometer (Radiometer-Physics GmbH, 2011). According to Urs U. Graf, the LO spectrum is fairly narrow (except for the GREAT H channel receiver, whose data is not used for atmospheric modeling), the resolution of the spectrometer can be considered as the frequency resolution of the system.

## 1.4 Calibration for atmospheric attenuation

The online calibration procedure<sup>9</sup> of ground-base and airborne sub-mm observations comprises reference measurement, gain calibration, and atmospheric calibration. The effect of atmospheric attenuation is compensated for in the last step.

In reference measurements (referred to as OFF measurements because they are measured towards positions on the sky *off* the source position), the atmospheric emission<sup>10</sup> as well as the noise from the telescope system are recorded and later subtracted from the source signal. Gain calibration is done by measuring blackbodies at different temperatures – the hot and cold loads, to monitor the gain drift of the receiver and apply the gain factor to calibration. Both reference measurement and gain calibration are done so often that the atmospheric emission, the noise and gain of the telescope system is expected to have very little change in the meantime<sup>11</sup>.

In contrast to reference measurement, the parameter needed for atmospheric calibration – the optical depth, is not directly measurable<sup>12</sup>. Atmospheric calibration also differs from gain calibration in the sense that the structure of the atmosphere is less well known than that of the receiver system. This makes the calibration for atmospheric attenuation prone to unnoticed error. Experiences with SMART and GREAT observations show that the emission and absorption of the atmosphere often change by more than a few percent over a few minutes. It is economically infeasible to directly measure the temperature and chemical composition at different altitudes so frequently. The only method of atmospheric calibration at sub-mm wavelengths is to derive the optical depth of the atmosphere from OFF measurements<sup>13</sup> with the help of an atmospheric model.

### *The need for an atmospheric model*

As mentioned at the end of last paragraph, an atmospheric model is needed to derive attenuation from measured emission. This is a very common *inverse problem* in atmospheric science, but is less studied for the physical condition specific to sub-mm astronomical observations.

For an SSB receiver whose sideband ratio is greater than  $\sim 20$  dB, the atmospheric transmission may be calculated channel by channel without using a sophisticated atmospheric model<sup>14</sup> if its spectral resolution is sufficient to resolve the atmospheric lines. However, with the help of a proper model, the sky transmission can be determined much more precisely as the modeled transmission is free from random noise and ripples caused by the telescope system. Besides, modeling is the only way to for a DSB receiver to distinguish the at-

<sup>9</sup> Calibrations that are usually done offline, such as that for main beam efficiency, is not part of our calibration procedure.

<sup>10</sup> Atmospheric emission is also measured with SKY measurements. Since OFF has to be measured anyway to monitor the instability of the receiver system, it is almost always done more often than SKY, and is used for atmospheric calibration.

<sup>11</sup> Though unexpected, they do happen in some cases according to the analysis of SMART and GREAT data in Chapters 5 and 6.

<sup>12</sup> In fact, the the optical depth of the atmosphere can be measured with calibration sources, or celestial sources whose spectral energy distributions are known. However, there are so few calibration sources at the sub-mm wavelengths that they are almost always far from the source being observed on the celestial sphere. It is impractical to use them for atmospheric calibration of sub-mm observations.

<sup>13</sup> Although water vapor radiometers are widely used for such calibration, they usually gives only the column density of water vapor, which is not enough.

<sup>14</sup> This can be implemented, e.g., with a very simple static atmospheric model (see next paragraph of the main text) that assumes a homogeneous atmosphere, and a radiative transfer model that assumes frequency independent absorption and spectral intensity of the atmosphere. This calibration method is not discussed in this thesis.

atmospheric emission in one sideband from that in the other sideband. When the receiver cannot resolve the spectral features of the atmospheric emission, e.g., the FIFI LS (Klein et al., 2006) receiver onboard SOFIA, an atmospheric model is also needed for accurate calibration.

An atmospheric model consists of a static model that gives the temperature profile along altitude (the pressure-temperature profile, or the P-T profile) as well as the chemical composition of the air, e.g., the water vapor column density (referred to as the precipitable water vapor or pwv), ozone, and etc.<sup>15</sup>, and a radiative transfer model that computes the emission (which is measured towards the OFF-source position) and absorption (which is used for atmospheric calibration) of the atmosphere.

<sup>15</sup> The atmosphere is assumed to be horizontally homogeneous. The effects of other parameters from the output of a static atmospheric model, such as the zonal wind and pressure-altitude profile, are negligible in particular for ground based and airborne sub-mm observations.

### *Setting up a static atmospheric model*

A static atmospheric model is used to derive the P-T profile from  $\sim 4$  to  $\sim 100$  km altitude, which corresponds to the part of the atmosphere that includes the upper troposphere, the stratosphere, and the mesosphere, as shown in Figure 1.5. The thickness of the atmosphere that has noticeable influence on sub-mm calibration is so small compared to the earth radius ( $\sim 6.4 \times 10^3$  km), that it can be assumed to be a plane parallel layer instead of spherical shell. This layer of air has strong vertical stratification along the line of sight. The temperature ranges from  $\sim 180$  K to  $\sim 320$  K, while the number densities of the major absorbing species (water vapor and ozone) can change by several orders of magnitude. For precise modeling of its radiative transfer, the atmosphere must be divided into a number of sub-layers, each having roughly homogeneous pressure, temperature, and chemical composition. The exact setup of the static atmospheric model in our case is dependent on observatory altitude, spectral data quality of the measured atmospheric emission, and the computing resource, as explained in Chapter 2.

As of this writing, the modeling scheme of *kalibrate* derives the P-T profile from observation data together with a reference atmosphere (CIRA: Barnett and Chandra (1990)), and does not make use of the geographical longitude and date, time information<sup>16</sup> which usually appear in meteorological research because such detailed modeling is too complex and complicated to implement and difficult to prove to be correct. The model that we use to derive the P-T profile is easy to implement, and allows for cross checking with the results of relevant meteorological studies.

<sup>16</sup> Geographical latitude and month are used for interpolation with the CIRA model.

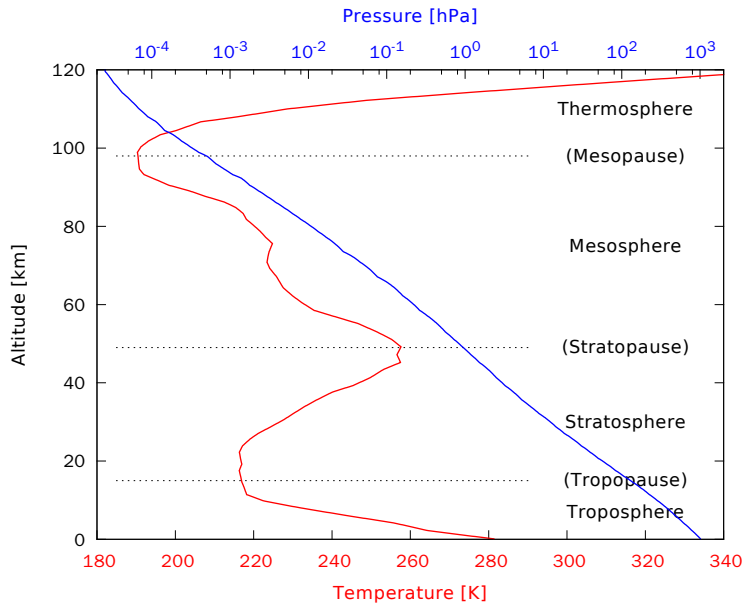


Figure 1.5: A typical P-T profile of the terrestrial atmosphere showing the troposphere, stratosphere, mesosphere, and the lower part of the thermosphere from the COSPAR International Reference Atmosphere (Barnett and Chandra, 1990). This thesis only attempts to model the part below the mesopause.

### *Choice of radiative transfer model*

A static atmospheric model, as explained above, provides the information of the P-T profile and chemical composition of the atmosphere. In order to compute the frequency dependent atmospheric emission and transmission from this information, we also need a radiative transfer model that is based on the theory of quantum mechanics and possibly some empirical formulae in addition. A number of radiative transfer models that suits sub-mm calibration are available because they can be theoretically derived and verified in laboratory. In a publication (Guan et al., 2012) that presented some preliminary work for this thesis we have evaluated several models available for use in radio astronomical calibration, including AM (Paine, 2014), ATM (Pardo et al., 2001), ATRAN (Lord, 1992), and MOLIERE (Urban et al., 2004). Because our goal is to obtain better calibration accuracy by improving the atmospheric model itself, we have chosen to use AM, whose code is well organized and can be easily interfaced with KOSMA-Software, and is intended to work with user defined static atmosphere.

According to the comparisons by Paine (2014), the spectra computed from the radiative transfer formulas in the AM atmospheric model are consistent with laboratory measurements within a few percent in the pressure and temperature range of the atmosphere during sub-mm observations. This amount of inconsistency is acceptable because it is of the same order as our aimed calibration accuracy.

### *Previous problems in sub-mm calibration*

The KOSMA<sup>17</sup> and NANTEN2<sup>18</sup> telescopes had already been operating for years in the 230 (mm wavelength), 345, 460, 490, and 810 GHz (sub-mm) bands before this study was carried out. During the calibration of KOSMA and NANTEN2 data using *kalibrate*, it had been observed that the precipitable water vapor (pwv) values derived from fitting the model to hot-cold-sky observations were different between different bands (e.g., 460 GHz and 810 GHz). While it is physically impossible for different bands to see different pwv's because their lines of sight are almost the same, it stayed unclear whether this comes from errors of the instrument the imperfection of the static atmospheric model and the physical parameters and formulas employed by the radiative transfer model. Finding out the cause to this problem can improve calibration accuracy, and may be also useful to receiver development.

Another problem of *kalibrate* was its computing performance. The calibration throughput measured in scans per second decreased drastically with the increasing number of spectrometer channels as well as the number of pixels<sup>19</sup>. As multi-pixel receivers (array receiver) and high resolution spectrometers had become common in sub-mm observatories, *kalibrate* was no longer capable of online calibration.

For these reasons, a faster and more flexible calibration tool (an updated version of *kalibrate*) was needed to speed up the calibration as well as the investigation of the atmospheric model. This is partly the work of this thesis.

### *Introduction to the calibration procedure*

Atmospheric calibration of sub-millimeter data depends on proper gain calibration in the first place. The calibration procedure is briefly described below. A detailed description is available in the Appendix of Guan et al. (2012). In most spectroscopic receiving systems for sub-mm radio telescopes, a single conversion heterodyne receiver is employed to convert the sky signal to the intermediate frequency. Radio astronomers often use the antenna brightness temperature,

$$T_{A,\nu} = \frac{\lambda^2}{2k} I_\nu \quad (1.3)$$

where  $I_\nu$  is the specific intensity, as a measure of the brightness of the celestial object because its value can be compared with the values of hot load, cold load, and receiver noise temperatures directly. Suppose we point the telescope to an empty sky position (i.e., no astronomical source, only consider the atmospheric emission) whose intensity

<sup>17</sup> <http://www.astro.uni-koeln.de/kosma>

<sup>18</sup> <http://www.astro.uni-koeln.de/nanten2>

<sup>19</sup> The previous version of *kalibrate* reads input data at a time complexity of  $O(n^2)$ , where  $n$  is the number of receiver pixels. The time to fit the model was  $O(b/\delta_f)$ , where  $b$  is the receiver's bandwidth, and  $\delta_f$  is the frequency resolution of the model.

corresponds to an antenna temperature  $T_{A,sky,\nu}$ , the total intensity of the narrow frequency bands around the signal and image frequencies  $\nu_s$  and  $\nu_i$  will be

$$\begin{aligned}
T_A = & \eta_{mb} t_{a,\nu_s} G_s x_s T_{MB,\nu_s} + \eta_{mb} t_{a,\nu_i} G_i x_i T_{MB,\nu_i} + & (1.4) \\
& (1 - f_{amb}) \left[ (1 - t_{a,\nu_s}) G_s x_s \tilde{T}_{sky,\nu_s} + (1 - t_{a,\nu_i}) G_i x_i \tilde{T}_{sky,\nu_i} \right] + \\
& f_{amb} [G_s x_s \mathcal{J}_{\nu_s}(T_{amb}) + G_i x_i \mathcal{J}_{\nu_i}(T_{amb})] + \\
& (1 - x_s) G_s \mathcal{J}_{\nu_s}(T_{term}) + (1 - x_i) G_i \mathcal{J}_{\nu_i}(T_{term}),
\end{aligned}$$

in which the corresponding variables are defined as

$T_{amb}$	physical temperature of ambient material
$f_{amb}$	fraction of ambient material in sky beam
$T_{term}$	termination temperature of sideband filter, or 0 if no sideband filter
$\eta_{mb}$	main beam efficiency
$T_{mb,s,i}$	source main beam brightness temperature in signal (image) sideband
$\mathcal{J}_\nu(T)$	brightness temperature of a blackbody at temperature $T$ measured at frequency $\nu$ ,
	$\mathcal{J}_\nu(T) = \frac{h\nu}{k} \left[ e^{h\nu/kT} - 1 \right]^{-1}$
	This formula gives the Rayleigh – Jeans correction at frequency $\nu$ .
$\tilde{T}_{sky,\nu}$	effective sky brightness temperature at frequency $\nu$ ,
	$\tilde{T}_{sky,\nu} := T_{A,sky,\nu} / (1 - t_{a,\nu})$
$t_{a,\nu}$	atmospheric transmission at frequency $\nu$
$G_{s,i}$	signal (image) sideband gain: $G_s + G_i = 1$
$x_{s,i}$	signal (image) response in sky beam,
	with coupling to sideband filter termination: $(1 - x_{s,i})$ .

The forward efficiency and main beam efficiency are assumed to be sideband-independent because its values at  $\nu_s$  and  $\nu_i$  are almost the same. The forward efficiency can be derived from atmospheric calibration when necessary.

The brightness of the input signal is a linear function of the back-end output<sup>20</sup>. The conversion coefficients (the receiver gain and noise temperature) are usually calibrated by measuring two black bodies at different temperatures – the hot and cold loads. The mixers are coupled to the load and sky through different optical paths, so  $\eta_{fw}$  and  $\eta_{mb}$  are unrelated to gain calibration. The effect of the optics that couples the load to the mixer is equivalent to a modulated load temperature<sup>21</sup>. For this reason, an “effective load temperature” is introduced to encapsulate the effect of the load emission, the warm optics, and ambient pick up. All of the reference to “load temperatures” hereinafter are “effective load temperatures” that denote the load brightness seen by the mixer.

<sup>20</sup> Direct detection effect affects the linearity of load calibration. However, for the commonly used load temperatures (about 70 to 300 K), the resultant non-linearity is typically small. Examples are shown by Lobanov et al. (2009) and other literature.

<sup>21</sup> The window transmission of the receiver Dewar (and the load, if applicable), is strongly frequency dependent, and typically changes by more than 50% across the whole range of the receiver’s operating frequency. However, it is assumed that the frequency dependency is negligible across the both sidebands because  $\nu_s$  and  $\nu_i$  are very close.

After gain calibration, the properties of the atmosphere, including the pwv, water vapor scaling height, and etc. can be fitted to the sky brightness temperature with the atmospheric model. In practice, we fit the difference of sky and hot load temperatures<sup>22</sup> because the receiver noise is mixed up with the measured sky signal, and can be canceled out by comparing with the measured hot load signal which includes the same amount of receiver noise, provided that the receiver is stable between the hot load and sky measurements. The parameters fitted with model are then used to compute the atmospheric transmission, and do the final calibration.

<sup>22</sup> Although the cold load measurement can be used for the same purpose, it is not used because the cold load temperature is less accurate.



## 2

### *Static atmospheric model*

In radiative transfer studies of the atmosphere, it is more convenient to define the air temperature as a function of pressure rather than altitude. The absorption coefficients, which depends on air pressure and temperature, have no simple relationship to altitude. The altitude is expressed in pressure in this thesis unless otherwise noted. The terms pressure and altitude are often used interchangeably.

A static atmospheric model defines the air temperature within the atmosphere as a function of altitude and possibly other parameters, including geographic latitude, date, time, and etc. Some models, such as the U.S. Standard Atmosphere (NASA, 1976) and NRLMSISE-00 (Picone et al., 2002), also define the density of each constituent of the air. The air species modeled by these models do not include water vapor and ozone, which are the primary absorbers at sub-mm wavelength. Therefore, we only use the P-T profiles from the models that are already publicly available, e.g., the CIRA shown in Figure 1.5 on page 18, and figure out the volume mixing ratios<sup>1</sup> of the minor species by other means as explained in later sections of this chapter.

Sub-mm calibration benefits from the usage of existing static atmospheric models because these models provide the altitudes of temperature minima and maxima, and a reasonable starting point to fit the lapse rate of the P-T profile. In this way the number of free parameters is reduced, which makes the fit more easily to converge. The drawback is that the model may systematically deviate from the real P-T profile due to the reduced number of freedoms, though this deviation is insignificant in our observations due to the limited signal-to-noise ratio.

As explained above, the mixing ratios of each air species and the additional lapse rate and offset added to the P-T profile must be figured out independently of the external static atmospheric model. The mixing ratios of the primary absorbing species (apart from molecular nitrogen and oxygen), water vapor and ozone, change significantly with altitude. Meteorological observations of these mixing

<sup>1</sup> The volume mixing ratio, also referred to as the mixing ratio in this thesis, of a gas species is the ratio between the number density of this species and that of the air.

Table 2.1. Ranges of the key parameters of the atmosphere

Name	Range	Description
$P_{\text{amb}}$	700 ~ 140 hPa	Pressure at the observatory
$P$	$P_{\text{amb}} \sim 0.01$ hPa	Pressure range of the model
$T_{\text{atm}}$	200 ~ 300 K	Air temperature outside the observatory
$T$	180 ~ 320 K	Typical temperature range of the model
$x_{\text{H}_2\text{O}}$	$< 10^{-3}$	Mixing ratio of water vapor
$x_{\text{O}_3}$	$< 10^{-5}$	Mixing ratio of ozone
$t_s$	$> 30\%$	Zenith transmission at the signal frequency

ratios above the telescope at the time of the astronomical observation are usually not available. Thus, their vertical distributions need to be modeled in order to reduce the number of fitted parameters. Modeling simplifies the problem under investigation, and naturally involves approximations to the real world. To keep errors under control, we need a clear understanding of the temperature structure and chemical composition of the air, physical processes that control them or affects astronomical calibration before building such an atmospheric model.

### 2.1 Ranges of the physical parameters of the atmosphere

The ranges of pressure, temperature, air mixing ratios, as well as the physical states of the absorbing species, are application specific.

For sub-mm astronomical calibration in particular, the lower 3~4 km of the troposphere, which is also the atmospheric layer where most active weather phenomena take place, need not be considered because all sub-mm telescopes are located at more than three kilometers above the sea level. As an early step to approach fast and accurate sub-mm calibration, this thesis only tries to deal with typical cases, which cover most of our observations.

The sky is usually clear during sub-mm observations<sup>2</sup>, and the Doppler effect of the wind on atmospheric line profiles is negligible because the atmospheric line widths, if expressed in velocity, have much larger absolute values than the wind speed. So we are going to model a completely stationary, gaseous atmosphere which is in hydrostatic equilibrium<sup>3</sup>. The typical ranges of the physical parameters of the atmosphere under conditions of interest is listed in Table 2.1.

<sup>2</sup> Clouds, which consists of liquid water and ice, in the atmosphere contributes a quasi-continuum component to the sub-mm absorption (Bertie and Lan, 1996; Warren and Brandt, 2008).

<sup>3</sup> Hydrostatic equilibrium is assumed to simplify conversion between pressure and altitude. This is not used for calibration but only for user interaction (generating figures).

## 2.2 *The layered atmosphere, atmospheric effects*

A static atmospheric model may use either an analytical representation of the atmospheric P-T profile (e.g., as in the U.S. Standard Atmosphere), or divide the atmosphere into a finite number of layers, each layer having a local temperature (e.g., as in the CIRA (Barnett and Chandra, 1990)). A continuous analytical P-T profile can be converted to a set of discrete pressure and temperature points. We choose to use the discrete representation to make it easy to use different reference P-T profiles. As explained in Section 1.4, the atmosphere is modeled with a number of plane-parallel layers. The division should be fine enough so that adding additional layers to the model does not result in significant changes<sup>4</sup> to the atmospheric absorption and emission profiles. On the other hand, the number of layers should be as few as possible to shorten the time of radiative transfer computing.

The algorithm that we are currently using to setup the static atmospheric model allocates one layer to fix the top boundary conditions, one layer for the mesospheric CO (Ruzmaikin et al., 2014), one layer between the mesospheric CO and the ozone layers, six layers for stratospheric ozone, and three or eight layers for the air below for airborne and ground based observatories, respectively. This setup gives a reasonable precision when fitting the water and ozone line profiles, and allows the radiative transfer model to run fast enough during online calibration.

With a given model setup, the precision is determined by the atmospheric effects on radio waves, including absorption, refraction, scattering, and etc. We attempt to model atmospheric absorption only because the other effects are negligible for calibration.

As shown in Figure 1.1, ground based sub-mm telescopes suffer from atmospheric attenuation mostly from the atmospheric water vapor near the ground, besides some broadband collision-induced absorption (CIA)<sup>5</sup> and some minor absorption by the gases, such as water vapor, ozone, carbon-monoxide, and etc. from high altitude. For airborne telescopes, the ozone absorption from the mid- to high-stratosphere becomes comparable to the absorption by water vapor. In GREAT/SOFIA observations, ozone often contributes to most of the sky brightness across a large portion of the passband, followed by water vapor absorption and the broadband CIA, as well as absorptions by other species that extend to even higher altitudes, such as atomic oxygen and mesospheric CO. The distributions of these absorbing species are discussed in separate sections.

At present there is no indication that the atmospheric absorption above the mesosphere need to be considered in sub-mm observations.

<sup>4</sup> The change is insignificant if the difference between the atmospheric emission profiles is smaller than the random noise, standing waves, and other imperfections of the measured spectrum.

<sup>5</sup> See page 39.

The air below the mesopause is assumed to be locally well mixed and in thermal equilibrium. That is, each absorbing species has the same P-T profile.

The temperature structure, chemical composition, and other characteristics of the terrestrial atmosphere are maintained by complex processes, of which radiative heating and cooling, and large scale circulation are dominant. Less prominent phenomena such as volcanic and human activities, solar events, etc. may greatly modulate the atmospheric CO and ozone content. All these complex processes need more thorough study. Our model deals with the distribution of different absorbing species in an empirical way without considering its cause.

### 2.3 *Water vapor vertical distribution*

The atmosphere mainly constitutes of molecular oxygen ( $\sim 21\%$  of the dry air), nitrogen ( $\sim 78\%$  of the dry air), a small portion of water vapor, which is typically less than 1% above sub-mm observatories, and other minor species. It is referred to as the dry atmosphere with water vapor taken apart. The dry atmosphere constitutes of  $N_2$ ,  $O_2$ , and some minor species such as Ar,  $CO_2$ , Ne, He, Kr, Xe,  $CH_4$ ,  $H_2$  and etc., which take up less than one percent of the total volume. Here we focus on the vertical distribution of water vapor, and leave the discussion over the dry atmosphere to the following sections.

One of the meteorological processes that controls the water vapor, as well as ozone, etc.'s distribution above both tropospheric and stratospheric sub-mm observatories is the Brewer-Dobson circulation (Brewer, 1949; Dobson, 1956) as well as related chemical reactions. Within the mid- to high-troposphere, the mixing ratio of water vapor is roughly proportional to the third order of pressure (Herbin et al., 2009). The power law index decreases around the tropopause. The stratospheric mixing ratio of water vapor can be assumed constant for calibration of ground based observations (Mastenbrook, 1968; Herbin et al., 2009) because the stratospheric water vapor is typically less than one percent of the total pwv, and the mesosphere is almost dry (Orsolini et al., 2010; Harries et al., 1996). However, this assumption is not accurate enough for airborne observations. In the case of SOFIA, a major part of the pwv comes from the stratosphere. HALOE, the Halogen Occultation Experiment (Russell et al., 1993) shows that, similar to that in the troposphere, the stratospheric water vapor mixing ratio also has a power law correlation with pressure, but with a small negative index (Harries et al., 1996) in low- and mid-stratosphere. The mixing ratio becomes constant in the high stratosphere between 1 and 0.1 hPa. Due to this coincidence<sup>6</sup>, the

<sup>6</sup> The physics behind this characteristic vertical profile of water vapor mixing ratio is a meteorologic research topic.

water vapor vertical profile of our static atmospheric model can be expressed in the same empirical formula for both tropospheric and stratospheric observations<sup>7</sup>:

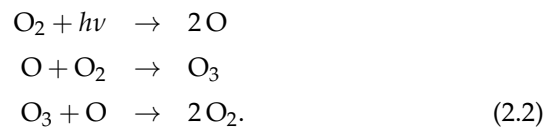
$$x_{\text{H}_2\text{O}}(s) = \begin{cases} x_c (P/P_e)^{P_s}, & P \geq P_e \\ x_c, & P < P_e \end{cases} \quad (2.1)$$

The  $x_c$ ,  $P_e$ , and  $P_s$  in Equation 2.1 have different meaning for tropospheric and stratospheric observations. In the former case,  $x_c$  represents the average mixing ratio of water vapor within the stratosphere, typically a few ppm (part-per-million) (Mastenbrook, 1968; Harries et al., 1996; Randel et al., 2006),  $P_e$  is the tropopause altitude, where  $x_{\text{H}_2\text{O}}$  comes to a minimum, and  $P_s$  is the power law index of mixing ratio vs. air pressure, typically around  $3 \sim 4$  (Herbin et al., 2009). This definition is roughly consistent with that in Guan et al. (2012) except that the altitude is expressed in air pressure. The modeled  $x_{\text{H}_2\text{O}}$  may not coincide with the humidity measured by the weather station of the observatory because weather stations are usually located close to the ground, and tend to be affected by evaporation.

For stratospheric observations,  $x_c$  is the average mixing ratio in the high stratosphere,  $P_e$  is the altitude where  $x_{\text{H}_2\text{O}}$  stops increasing with altitude (at about 1 hPa), and  $P_s$  is the negative power law index of mixing ratio vs. air pressure, typically between 0 and -1 (Harries et al., 1996).

#### 2.4 Ozone vertical distribution

In the high mid- to high-stratosphere where the short wave ultraviolet (high frequency UV-B, UV-C and shorter waves) solar radiation is strong (compared to the troposphere), and the density of oxygen is high enough (compared to the mesosphere and above), the mixing ratio of ozone can rise over a few ppm when the following reactions reach equilibrium

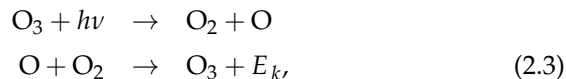


The lifetime of ozone molecules in the stratosphere is so long that the ozone density is mainly regulated by the Brewer-Dobson circulation, and has a seasonal variation<sup>8</sup>.

<sup>7</sup> The exception is observation taken closely below the tropopause. This case is not covered by the methods in this thesis, and will be dealt with by future work.

<sup>8</sup> Some events, such as solar flares and volcanic eruptions, do change ozone mixing ratio in short time. These unpredictable events are not considered when modeling the atmosphere. However, their effects on ozone enrichment or depletion can be reflected by our model.

The ozone-oxygen cycle maintains a potential temperature<sup>9</sup> profile that increases with altitude in low- an mid-latitude, which preventing violent convection from happening, with the following reactions



where  $E_k$  is the kinetic energy released. The stratospheric ozone produced by the ozone-oxygen cycle thus do not suffer from significant loss or down-transfer to the troposphere by convection. This makes it possible for the stratosphere to maintain a relatively stable ozone level.

The vertical distribution of ozone is more complex than that of water vapor. Its profile is highly variable<sup>10</sup> because the equilibrium point of reactions 2.2 is sensitive to many factors. For example, the peak ozone level decreases regularly by more than ninety percent every spring in the Antarctic, but only occasionally in the Arctic region, as reported by World Meteorological Organization (2014). We haven't carried out any observation under ozone holes as of this writing. As a first approach, we assume the mixing ratio of ozone to have a single peaked vertical profile between 1.6 and 120 hPa, or roughly 15 and 45 km in altitude, according to the data from the GOME-2 (Callies et al., 2000) and NEUBrew (Disterhoft et al., 2008) atmospheric science projects, and various literature, such as Wang et al. (2006) and Steinbrecht et al. (2006).

The non-depleted, single-peak ozone profile does have a diurnal variation of a few percent according to many meteorological experiments. As the stratospheric air circulates from tropical regions to higher latitudes, and subsides to the troposphere, ozone accumulates at the bottom of the polar stratosphere and forms a thicker layer than the tropical ozone layer. This is modeled in our calibration procedure by adding a linear scaling and skew factor to a typical profile of temperate latitude<sup>11</sup>.

## 2.5 CO vertical distribution

Atmospheric carbon-monoxide often shows up as bright (more than ten Kelvins) and narrow (less than 0.7 km/s, much narrower than the receiver passband) lines (in the GREAT frequency range, see Figure 2.1) in astronomical observations because, as the second abundant molecule in the universe, CO is frequently observed by radio astronomers. The atmospheric CO below the mesosphere is usually undetected at the S/N ratio of typical astronomical observations because they appear as very weak broad wings due to pressure broadening. Its narrow spectral lines from higher altitude are mainly ther-

<sup>9</sup> The potential temperature  $\theta$ , whose vertical profile is a direct measure of the hydrostatic stability, is defined as  $\theta := T (P_0/P)^{R/c_p}$ .

<sup>10</sup> By an order of magnitude, as shown by World Meteorological Organization (2014).

<sup>11</sup> This approach leaves us the convenience to adjust individual mixing ratios for each model layer by tuning the typical profile itself, thus making it possible to model an ozone hole without changing the algorithm.

mally broadened and have almost the same widths in velocity. They can affect the atmospheric calibration of the celestial signal of nearby frequencies. Therefore, the carbon-monoxide we need to model is in the mesosphere.

The carbon-monoxide in the middle atmosphere (stratosphere and mesosphere) is mostly a photolysis product from carbon-dioxide<sup>12</sup>, and has a lifetime of several weeks in the mesosphere. This production mechanism gave the CO mixing ratio a vertical profile that increases with altitude middle atmosphere, which is shown by many studies, such as Dupuy et al. (2004); Pumphrey et al. (2007); Hoffmann et al. (2011); Forkman et al. (2012) and etc. It also gives the vertical distribution of CO a simple, prominent annual cycle (Forkman et al., 2012) with less significant variations on both longer and shorter timescales (Ruzmaikin et al., 2014).

Because the atmospheric CO line only affects very narrow frequency bins, and is often shifted away from the astronomical CO line due to the Doppler-effect, we do not attempt to fit its spectral profile<sup>13</sup>. In our static atmospheric model, carbon-monoxide is assumed to reside around an altitude of 0.01 hPa and has a mixing ratio of 15 ppm, which is a typical value from Forkman et al. (2012). The altitude (or pressure) is not really important because, as mentioned before, pressure broadening is insignificant.

<sup>12</sup> Other production or enhancement mechanisms, such as volcanic activities, are difficult to model. We do not consider their effects.

<sup>13</sup> However, because the absorption by atmospheric CO is non-negligible and does affect calibration when they overlap with astronomical spectra, we will try to model it's distribution in future work.

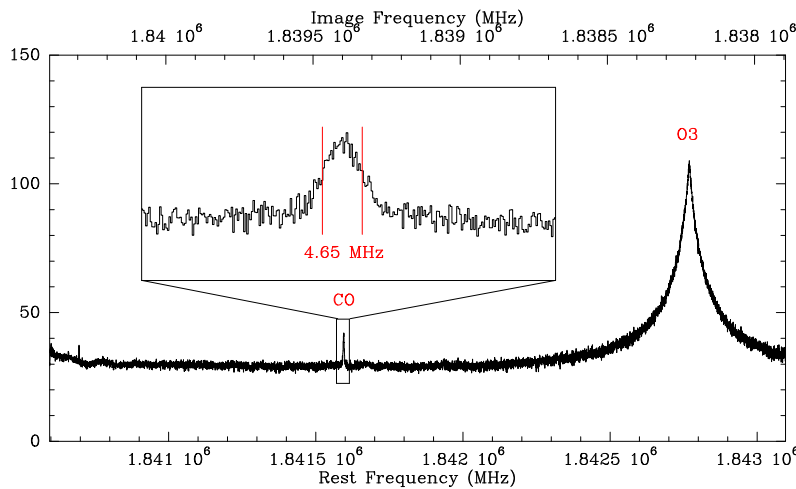


Figure 2.1: Atmospheric ozone and CO lines of an observation using the GREAT L2 channel receiver. The figure shows the spectra over the whole pass-band with signal (image) frequencies marked on the lower (upper) axes. The temperatures (vertical axis, in Kelvins) are in double-sideband scale with a sideband ratio of 1:1.

## 2.6 Atomic oxygen in the atmosphere

The [OI] line at 4.7 THz is an important cooling line in both astrophysics and atmospheric physics study (Rezac et al., 2015, and references therein). However, the radiative transfer model that we currently use (the AM model from Paine (2014)) does not include the

[OI] line. Modeling of the atmospheric [OI] emission is difficult also because of the instability of the local oscillator (LO) of the GREAT receiver, which problem is expected to be solved in the near future. The atmospheric [OI] line in our model only serves as a frequency calibrator for the LO, and is not considered in calibration against atmospheric attenuation. That said, the somewhat large line width of the atmospheric [OI] line (see Figure 2.2) does show the necessity of modeling because the same celestial line is often located on the wings of the former. This part of work is however not included in this thesis.

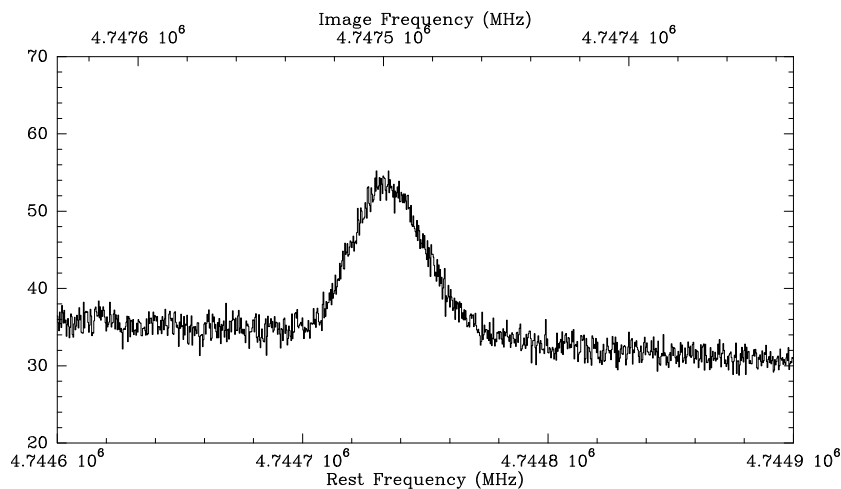


Figure 2.2: Atmospheric [OI] line observed with the GREAT H-channel receiver, zoomed in to 12% of the passband. The temperatures are in double-sideband scale with a sideband ratio of 1:1.

## 2.7 $N_2$ and $O_2$

The most abundant species of the terrestrial atmosphere,  $N_2$  and  $O_2$ , contributes a broadband collision induced emission and absorption profile to the atmospheric spectrum. These two species are well mixed in the mesosphere and below. We assume constant mixing ratios of  $N_2$  and  $O_2$  throughout the whole range of altitude in our model.

## 2.8 $N_2O$ vertical distribution

Atmospheric  $N_2O$  has relatively weak lines at the sub-mm wavelengths (Paine, 2014). Its spectral features are often covered by the random noise and baseline imperfections of the receiving system. The reason that we included  $N_2O$  in our atmospheric model was for debugging purpose, that one candidate of the radiative transfer models to be used for SOFIA / GREAT calibration produced  $N_2O$

lines that were several orders of magnitude stronger than the other models (Guan et al., 2012). We therefore assume a constant mixing ratio of 0.3 ppm below the altitude of 50 hPa, which is reduced to 0.1 ppm between 50 and 20 hPa, and no N<sub>2</sub>O at all above the altitude of 20 hPa. This is a rough approximation of the observed N<sub>2</sub>O distributions (Fabian et al., 1979; Taylor et al., 1996; Strong et al., 2008). Anyway, the attenuation by N<sub>2</sub>O has no measurable effect on atmospheric calibration with the S/N ratio of our observations.

## 2.9 *Minor absorbers*

The contribution of other minor species, such as CO<sub>2</sub>, CH<sub>4</sub>, and etc. to the atmospheric absorption profile is several orders of magnitude lower than that of water vapor, ozone, and the CIA by N<sub>2</sub> and O<sub>2</sub> at sub-mm wavelengths. They are ignored in our modeling process.

## 2.10 *The P-T profile*

The distribution of water vapor, ozone, CO, and atomic oxygen determines which part of the atmosphere is related to sub-mm calibration, limiting the air pressure and temperature range of our model. The U.S. Standard Atmosphere was used for the reference P-T profile until SOFIA / GREAT became ready, when we switched to the CIRA in order to model mesospheric water and CO emission. In our calibration scheme, the atmospheric P-T profile is derived from a *reference atmosphere* by tuning its tropospheric and stratospheric lapse rates. An accurate tropospheric lapse rate is important to atmospheric modeling for ground based observations because in this case most of the absorption come from the water vapor (as explained in the previous section) in the lowest a two or three kilometers (Herbin et al., 2009). By contrast, an accurate stratospheric lapse rate is important to GREAT observations because SOFIA flies around the tropopause. The P-T profile above the stratopause is difficult to model and also less important. As explained in Section 2.5, the vertical distribution of CO has a relatively simple pattern of annual variation. Therefore, it is possible to model both the temperature structure of the mesosphere and the vertical profile of CO mixing ratio using multi-band CO observation<sup>14</sup>. However, multi-band CO observation may not be always possible because astrophysical projects often require tuning to other frequencies. Considering that an accurate mesospheric P-T profile is almost irrelevant to sub-mm calibration except at the frequencies near the atmospheric CO lines, and that we are not going to put effort on modeling atmospheric CO anyway as explained in Section 2.5, we do not attempt to model the mesospheric P-T profile accurately.

<sup>14</sup> The excitation temperature, or simply the air temperature if assuming local thermal equilibrium, can be derived from multi-band observation more precisely than single-band observation. However, this is out of the scope of this thesis.

The publicly available static atmospheric models depict the atmosphere in coarse granularity. Their output parameters are calculated empirically as a global or regional average over more than a few degrees' latitude. These outputs are either independent of time or as an estimation over a period that is much longer than that of a typical sub-mm astronomical observation. A temperature offset is added to it before the P-T profile is used for radiative transfer computing in order to satisfy the measured boundary condition.

While the Brewer-Dobson circulation contributes to stratospheric heating and cooling (Brewer, 1949, Section 10), the ozone-oxygen cycle (see Section 2.4), obviously has more influence over the stratospheric temperature structure (Revathy et al., 2001). Considering that the tropospheric lapse rate may also be different from the reference atmosphere, we introduced two additional parameters to adjust the tropospheric and stratospheric temperature gradients of the reference atmosphere. In conjunction with the temperature offset mentioned above, the atmospheric P-T profile can be derived from the P-T profile of the reference atmosphere.

### 2.11 *Validity of the static atmospheric model*

The static atmospheric model described above is intended to cover the physical conditions of the upper troposphere up to the mesopause at any location<sup>15</sup> as long as no geophysical event that has significant effects on the physical and chemical properties of the atmosphere occurs. This is probably not a real limitation because the lifetime of a radio observatory is short on geographical time scale.

The modeling experiments we have done are based specifically on the observations of the terrestrial atmosphere during last few years, while the meteorological literature we have referred to come from the past century. The calibration scheme has been tested with temperate and tropical data observed by GREAT onboard SOFIA across a wide range of geographical locations, and is expected to be valid for at least several decades.

For the reason of receiver stability, a measurement (or integration of the signal), cannot last much longer than one minute. Therefore, the fitted model parameters are usually used to calibrate the observations from the previous or next minute. We have not observed significant change of atmospheric emission with either ground based or airborne telescopes within such a short time, so a non-simultaneously measured sky can be used for atmospheric calibration of the source signal without any problem.

<sup>15</sup> An exception is the (possibly particular) atmospheric properties of the polar regions. There are promising sites in the Antarctica (e.g., Sims et al. (2012)) for sub-mm observation, which are not covered by the atmospheric model in this thesis due to both the incompleteness of the reference atmosphere used (CIRA86) and the high variability of ozone concentration.

### 3

## *Radiative transfer model*

A static atmospheric model with one or more plane parallel layers, as shown in Chapter 2, is used for radiative transfer computation. The air in every layer of the model has a specific chemical composition, pressure and temperature denoted by the parameters in Table 3.1, where the first layer ( $i = 0$ ) is the topmost layer<sup>1</sup> of the model, and the last layer is just above the telescope. Once the static atmospheric model is defined, we can use an existing radiative transfer model to compute the absorption spectrum of the atmosphere.

It is necessary to model the radiative transfer process of the atmosphere because there are a number of unresolved problems on this topic. The overall problem is the discrepancy between the observed spectra and the spectra from theoretical predictions. Paine (2014) has listed some of these discrepancies and dealt with them in Chapters 3 and 4 of his atmospheric model. Apart from the efforts to model the CIA and the quasi-continuum component of water vapor spectra (Paine, 2014, Chapter 4), the shapes of the individual molecular lines are modeled with various profile functions by taking into account their broadening mechanisms, coupling, and etc. The parameters used to compute these functions are provided by the model for use in the pressure and temperature range of the atmosphere listed in Table 2.1 on page 24. The choice of the formulae and their parameters used to model the atmospheric absorption spectrum is the main dif-

<sup>1</sup> The topmost layer is used to fix the upper boundary condition, and contains minimal amount of air whose effects on hydrostatic equilibrium and atmospheric attenuation of the astronomical signal are negligible.

Table 3.1. Layer parameters of static atmospheric model

Name	Description
$P_i$	Pressure at the bottom or base of the $i$ -th layer
$T_i$	Temperature at the bottom of the $i$ -th layer
$x_{k,i}$	Mixing ratio of the $k$ -th species across the $i$ -th layer

ference between different atmospheric models, besides that they may have different built-in static atmospheric models, which we don't use.

There are a few models that have been widely used for atmospheric radiative transfer computation at sub-mm wavelengths. Among them we investigated ATM (Pardo et al., 2001), ATRAN (Lord, 1992), MOLIERE (Urban et al., 2004), and the AM model (Paine, 2014). These models chosen as candidates for use in *kali-brate* for different reasons. The advantages and disadvantages of each model are discussed in individual sections of this chapter. All of these models use the parameters in the HITRAN database (Rothman et al., 2009) to calculate the spectral line profiles.

### 3.1 ATM

ATM is the atmospheric model used for atmospheric calibration at the Atacama Large Millimeter Array (Planesas, 2013). Historically, the KOSMA observatory, which operates at 230 and 345 GHz, used ATM (Pardo et al., 2001) to generate a tabular database (the "atm-table") which defines the atmospheric opacity as a linear function of the pwv at each frequency:

$$\tau_\nu = b_\nu \cdot pwv + c_\nu, \quad (3.1)$$

as explain by Guan et al. (2012), which paper is part of this thesis work. ATM is therefore the first radiative transfer model we have tested for use at sub-mm wavelengths.

ATM is being used to model the sky transmission at KOSMA and NANTEN2. It makes use of the U.S. Standard Atmosphere (NASA, 1976) to derive the P-T profile and the chemical composition of the air. The static atmospheric model and the radiative transfer formulae in ATM are fine tuned to fit with the FTS measurements from 0.17 to 1.1 THz (Pardo et al., 2001). The scientific data taken by KOSMA and NANTEN2, and are calibrated with the help of ATM are widely used in astrophysical research without showing noticeable inconsistencies with other literature, showing that the model is reliable from 230 to 810 GHz to some extent.

#### *Using the ATM model*

In order to compute the atmospheric transmission across a given frequency range, the user of ATM must specify the site altitude and the the total pwv. The P-T profile, the vertical distribution of water vapor as well as other species (ozone and etc.) are pre-defined. This level of flexibility is acceptable by KOSMA and NANTEN2 because water vapor, as the predominant absorber for these observatories, is mostly concentrated near the ground. The amount of systematic

error coming from the difference between the actual and the pre-defined temperature lapse rates, water vapor scaling factors, and etc. are not large enough to produce significantly different astrophysical results than that from other observatories<sup>2</sup>. When we come to higher altitude, it becomes important to model the P-T profile because the absorbing species (mainly water vapor and ozone) are more widely distributed along altitude. The ATM model lacks of such flexibility.

By analyzing the executable file of ATM (since the model is no longer supported by its author, and its source code is unavailable), it was found that the model may also allow user defined P-T profile and vertical distributions of one of ozone, CO, N<sub>2</sub>O, and etc. This feature is helpful to modeling stratospheric air regarding sub-mm radiative transfer, but not flexible enough when we need to model more than one minor species (ozone, CO, and atomic oxygen). Moreover, the ATM model is neither tested nor expected to be used at the frequency as high as 4.7 THz.

### *Feasibility of application in sub-mm calibration*

The ATM model cannot be improved due to lack of documentation, source code, and support from its author. Therefore, we eliminated ATM from our list of candidates for high altitude sub-mm atmospheric calibration.

## 3.2 ATRAN

Since this thesis is related to SOFIA / GREAT observations in many aspects, and ATRAN (Lord, 1992) is the atmospheric model officially chosen for SOFIA observations<sup>3</sup>, the ATRAN model naturally became one of our candidates. Similar to ATM, ATRAN also includes a static atmospheric model. ATRAN includes a tabulated model of the static atmosphere with four ozone profiles at different latitudes. The choice among ozone profiles is particularly useful for GREAT. In this sense, it is a simple to use and more flexible than ATM.

### *Problems of the model*

There are mainly two problems in the spectra computed by ATRAN: one is the spurious N<sub>2</sub>O lines that are impossibly strong, and the other is the lack of the quasi-continuum CIA component.

An artifact of ATRAN was found in the N<sub>2</sub>O spectra it produced when we were trying to apply it to GREAT calibration. According to several atmospheric experiments, the vertical distribution of nitrous oxide (N<sub>2</sub>O) is roughly constant in the troposphere, with a mixing ratio of about 300 ppb (Fabian et al., 1979) at all altitudes,

<sup>2</sup> This kind of error is, however, large enough to cause discrepancy between different frequency bands that are absent from a more sophisticated model.

<sup>3</sup> ATRAN is used for atmospheric modeling on the official webpage of SOFIA: <https://atran.sofia.usra.edu>. However, it is not the model used for calibration of GREAT data.

and decreases almost linearly from tropopause till 30 or 40 km (the mid-stratosphere), tapering into a trace amount (Strong et al., 2008). The spectra produced by ATRAN, however, indicates an  $\text{N}_2\text{O}$  concentration of about  $10^3$  more than observed, as shown in Figure 3.1 in a layer that is one or two kilometers thick just above the altitude of 50 hPa (or about 20 km). i.e., Only with this increased mixing ratio could other models produce similarly strong absorption lines of  $\text{N}_2\text{O}$ . There was no evidence that this artifact has affected KOSMA and NANTEN2, but this is potentially a risk for all, and especially wide band observations that we are going to calibrate.

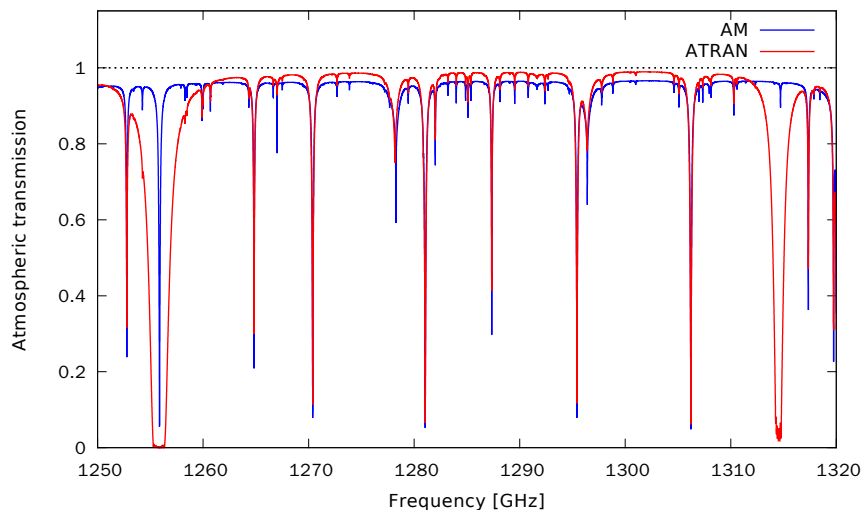
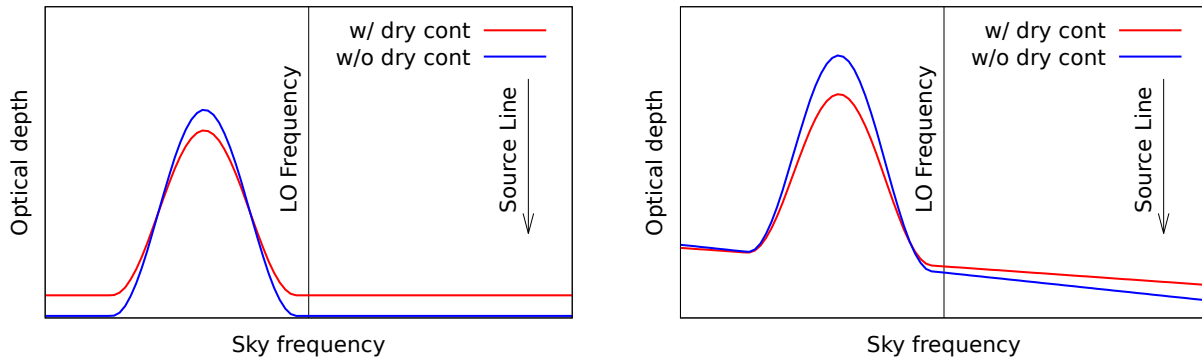


Figure 3.1: Spurious  $\text{N}_2\text{O}$  lines at 1256 and 1315 GHz from ATRAN compared to the spectra produced by AM.

The spectral line profiles produced by ATRAN are based on the HITRAN database. These line spectra are similar as those of the other models (except that of  $\text{N}_2\text{O}$ ). However, the quasi-continuum CIA component of the dry air is missing (Guan et al., 2012). The spectral power of this dry continuum is “transferred” to narrower lines, resulting in stronger water and ozone lines than that from other models. This much of error is not crucial to observation planning because its influence on observing time estimation is only a few percent, while a large operational overhead (of 100%, as suggested by the official GREAT time estimator) must be taken into account anyway<sup>4</sup>. While the model serves both observation planning and final calibration, the latter usage is aimed at higher accuracy. The complete absence of dry continuum from the model may yield calibrated data that is only marginally acceptable when a strong atmospheric line comes into the receiving bandpass, in which case the modeled atmospheric transmission may be too low at frequencies far from that atmospheric line center, as explained in Figure 3.2.

<sup>4</sup> Apart from the integration time, the observing time must also include some overhead for telescope mechanical movements, calibrations, human (operator) reactions, and so on. The overhead on observing time varies across different observing modes such as pointed position switch, OTF position switch, beam switch, load switch, and etc.



### *Feasibility of application in sub-mm calibration*

Besides these two problems, the flexibility of ATRAN, though better than ATM, is still not optimal. Given a highly variable ozone profile of the terrestrial atmosphere, together with the distributions of absorbing species that are unexpected by the ATRAN model, e.g., the varying distributions of water vapor and carbon monoxide in the middle atmosphere, the atmospheric model must also allow easy adaptation to new measurement results in order to improve data quality with least effort. Restructuring the ATRAN code (which is written in a Fortran dialect that cannot be understood by recent compilers) to serve this purpose requires too much work, and is therefore unrealistic. A model with a sophisticated mechanism for changing the air composition, P-T profile, and other parameters was looked for, hence come MOLIERE and AM as our candidates.

### 3.3 MOLIERE

The MOLIERE model (Urban et al., 2004) is a sophisticated forward and inversion model that we put much hope on, particularly because of its flexibility, and that one of its authors, Nicola Schneider, had tight cooperation with (and is now a member of) the KOSMA group, and can integrate the model with KOSMA-Software. It can compute atmospheric radiative transfer in the limb-sounding, nadir-sounding, and up-looking geometries<sup>5</sup>, and takes atmospheric refraction into account as opposed to our simpler atmospheric model described in Chapter 2. Because this model is intended for use on the middle atmosphere, it is expected to fully cover the altitude range to be modeled for the atmospheric calibration of GREAT data.

Figure 3.2: Left panel: Fictitious atmospheric opacities produced by a model with dry continuum and another model without. Right panel: The least squares fit with water vapor as the only free parameter gives different calibration factors at the frequency of the astronomical line to be observed.

<sup>5</sup> Atmospheric calibration for radio telescope observation falls in the last case.

*Advantages and disadvantages*

MOLIERE supports modeling of many more air species than the other candidates, of which the support for the atomic oxygen line [OI] is vitally important for GREAT calibration because [OI] observation is the only scientific goal of the GREAT H-channel receiver. The P-T profile and vertical distributions of minor species are defined in separate text files, giving the user full flexibility of defining a customized static atmospheric model.

The MOLIERE model satisfies all of the scientific requirements by sub-mm astronomical data calibration. However, the model code is mostly written in Fortran, with comments written in French, both languages the author of this thesis could hardly understand. This makes it difficult to integrate this promising candidate in *kalibrate*.

*Feasibility of application in sub-mm calibration*

With the kind help from Nicola Schneider, Guan et al. (2012) were able to compare MOLIERE with other models and found discrepancies among their modeling results. Further collaboration has been proposed to incorporate MOLIERE as one of its atmospheric models in KOSMA-Software in the future.

### 3.4 AM

The last candidate, AM, is the radiative transfer code used by SMA, "the Sub-millimeter Array", located at the summit of Mauna Kea, 4080 m above sea level. The AM model is different from the other models mentioned above in that it does not come with a pre-defined static atmospheric model<sup>6</sup>. The lack of a pre-defined atmosphere may cause trouble to a casual user, but is an important virtue for atmospheric study because it implies that the modeling results from different versions (including future versions) of the same model will only come from radiative transfer computation, essentially decoupling the two steps of atmospheric modeling – setting up a static atmospheric model and computing its radiative transfer process.

<sup>6</sup> Actually, AM does provide default mixing ratios of various gases including crude values of some minor species, but we always explicitly specify the mixing ratios of the minor species that have non-negligible effects on sub-mm calibration. These minor species are listed in the previous chapter.

*Radiative transfer formulae adopted by AM*

There are two categories of spectral profiles in AM: spectral lines and quasi-continuum components. Most spectral features of the atmosphere, including that from O<sub>3</sub>, CO, N<sub>2</sub>O, CH<sub>4</sub>, OCS, CO<sub>2</sub>, and etc. are modeled with various line shapes using the parameters from the HITRAN database. The line shape formulae in AM produce spectral line profiles under the affection by pressure, line coupling,

and etc. For water vapor, ozone, and CO, the Voigt-Kielkopf profile (Kielkopf, 1973) is used to model their line shapes in order to take thermal broadening into account, while their default line shape in the model ignores thermal broadening.

The quasi-continuum, collision induced absorption (CIA) is computed from the formulae and parameters from Borysow and Frommhold (1986)<sup>7</sup> and Boissola et al. (2003), with simplifications for the terrestrial atmosphere as explained by Paine (2014). Some parameters from the references therein have been modified by Paine (2014) in order to fit to experimental results. In addition, the difference between the measured spectra of water vapor and the sum of the dipole-allowed transition lines with simple impact-broadened collisional line shapes is taken care of with the “water continuum” component. Because of the difficulties in theoretical efforts, computation of water continuum is based on the semi-empirical MT\_CKD model (version 2.5). As shown by the comparison with laboratory measurement data in the manual of the AM model, the radiative transfer formulae for line and continuum spectra are accurate enough under the physical conditions of the terrestrial atmosphere. The model is valid at frequencies up to 15 THz (Paine, 2014).

<sup>7</sup> See also Borysow and Frommhold (1987).

### *Using the AM model through an atm-table*

The user interface of the AM atmospheric model is very simple and straightforward. Like most common Unix tools, AM reads the input and writes its output using the three standard I/O streams<sup>8</sup>. In our modeling procedure, the default abundances of molecular nitrogen and oxygen, as well as that of gaseous absorbers which have negligible effect on sub-mm calibration, are used.

<sup>8</sup> The modified version of AM in the KOSMA Software repository can be used through library calls, saving the need for conversion between raw and formatted output.

In KOSMA-Software, the AM model is used in two ways – either by feeding a static atmospheric model to the AM program, as explained by (Paine, 2014) in the manual, or in the traditional way of KOSMA-Software, through an atm-table that contains the ‘b’ and ‘c’ coefficients in Equation 3.1. The former method was impractical until the year of 2015 due to computer hardware restrictions. The other method that calculates the optical depth of the atmosphere with a linear function of the pwv has been used for many years. Its validity can be proven analytically but with the bold assumption (Guan et al., 2012) that the air temperature does not change with altitude because our algorithm converts the atmospheric opacity into sky brightness with the following formula

$$T_{sky,\nu} = (1 - e^{-\tau}) T_{atm} + e^{-\tau} T_{bg}, \quad (3.2)$$

where the  $T_{atm}$  and  $T_{bg}$  are the air temperature just outside the ob-

servatory and the temperature of the cosmic background radiation, respectively. Years of experience have shown that the systematic error introduced by this assumption is acceptable because nobody would notice the inconsistency resulted from this calibration method in astronomical research. Although the approximation of an altitude independent air temperature is likely too crude in the case of GREAT calibration especially near the center of ozone, CO, and weak water lines<sup>9</sup>, this was our only choice due to the tight schedule before the observatory characterization flights of SOFIA / GREAT.

The atm-table was generated by computing the model at two different pwv's, and solving the "b" and "c" coefficients from the optical depths. Because the atm-table is calculated only once and looked up many times, we chose to divide the static atmospheric model into as many layers as possible, so that further division of the model layers do not give different atmospheric emission and transmission that are differ by more than a few percent<sup>10</sup>. The cost was that running the model on the whole frequency range covered by GREAT takes more than twenty-four hours because the "b" and "c" coefficients are computed at nine different ambient pressures, or altitudes. The actual coefficients used for GREAT calibration are interpolated to the measured ambient pressure of each observation.

The method of using the atm-table as an intermediate step for radiative transfer computation is the default choice in *kalibrate*.

### *Using the AM model directly in the calibration procedure*

The availability of a local data storage and compute server to the KOSMA group starting from early 2015 enabled us to implement and test for performance and stability using the AM model directly in our calibration procedure with large datasets. This electric power consumption of the server is well within limit put by SOFIA. The calibration procedure, once tested, can be used immediately for online calibration during GREAT observations.

There are two differences in the strategy of setting up the static atmospheric model compared to the approach of using the AM model through an atm-table. Firstly, the computing time of the model must be reduced. In the atm-table approach, the atmospheric transmission on a total bandwidth of 4 THz is computed in one or two days. When fitting the measured sky brightness, each call to the model to compute the atmospheric model over a total bandwidth of 5 GHz including the signal and image sidebands must not exceed a fraction of a second<sup>11</sup>. This means that the time to compute the model on the same frequency grid must be reduced by an order of magnitude when the absorption coefficients are missing from the disk cache of

<sup>9</sup> Most of the actual GREAT observations are targeted to astronomical lines far away from the center frequencies of these lines for better atmospheric transmission. Therefore, the astrophysical publications based on GREAT observations remain trust worthy despite of the calibration approach.

<sup>10</sup> This translates to less than one percent in the calibration accuracy because the typical atmospheric attenuation for a SOFIA / GREAT observations is about ten to twenty percent.

<sup>11</sup> For comparison, the time needed to compute the atmospheric brightness from the atm-table is on the order of milliseconds.

the AM model With the improved capability of parallel processing of our new server, the running time of the model is still marginal for of-line calibration, and insufficient for online calibration. The tightened run time limit requires that the static atmospheric model can have only a limited number of layers under any weather condition, resulting in the second difference in the model setup strategy – the number of model layers is reduced to a minimum in this case. In order to setup the static atmospheric model automatically under different ambient pressures for both ground based and airborne observations, we divided the atmosphere into a fixed number of layers above the tropopause and a variable number of layers below. The layers above tropopause are adapted to the vertical distribution of ozone and CO. Most of the layers below the tropopause are close to the observing altitude, where the change of water vapor mixing ratio with altitude is likely to be significant.

Apart from the strategy of setting up the static atmospheric model, we also moved to the COSPAR International Reference Atmosphere (CIRA, Barnett and Chandra (1990)) from the U.S. Standard Atmosphere (NASA, 1976) in order to model the mesospheric P-T profile. The rest is as described in the previous chapter.

There is one problem in the model fitting process – During the iteration, the pwv can be too low or too high such that Equation 2.1 on page 27 has no solution with a given residue mixing ratio above a certain altitude ( $x_c$ ). In this case, we calculate a minimum or maximum pwv for the given  $x_c$ , and scale the whole vertical profile of water vapor distribution linearly to accommodate to the give pwv. This “scaling” is intended to guarantee the stability of the automatic model setup algorithm, and not expected to happen after the fit has converged. In other words, the residue mixing ratio  $x_c$  should be fitted as a free parameter if the scaling does happen with the fitted pwv at the given  $x_c$ .

The method of using the AM model directly for radiative transfer computation is not the default choice of *kalibrate* but can be activated with a command line option.

### 3.5 Choice of radiative transfer models

The MOLIERE model is the one candidate that completely satisfies the scientific requirements of GREAT calibration. The AM model is also fine, though lacking the capability to model the atmospheric [OI] line<sup>12</sup>. We chose to use the AM model in KOSMA-Software and leave the possibility of interfacing with MOLIERE as well we other models in the future. This was basically because the author of this thesis could manage to use the AM model but not MOLIERE before

<sup>12</sup> The inclusion of the [OI] line will be included in the next release (version 9.0) of the AM atmospheric model.

the first GREAT observation. As Guan et al. (2012) showed, there are large discrepancies between the modeled collision induced absorption and emission between AM and MOLIERE. Therefore, MOLIERE may become be another option besides AM as the radiative transfer model used by *kalibrate*.

# 4

## *The calibration procedure*

Among the various utilities of KOSMA-Software, *kalibrate* is the component that processes the raw data of the observations that have arbitrary units, and produces calibrated output in terms of brightness temperatures. The calibration process also produces two byproducts: the physical conditions of the atmosphere from atmospheric modeling, and the data that can serve as an input for the online display utility to show the result of the previous observation and the status of the telescope system.

The *kalibrate* program can run in either online or offline mode. In online mode, it follows the progress of the observation and calibrates the latest data with previous calibration scans. The calibration of one observation, which may be one scan or subscan depending on the observing mode, is expected to finish before the end of the next observation. This reason is why *kalibrate* must be a real-time program, and the running time of the atmospheric model is limited. When running in offline mode, *kalibrate* processes the ranges of scans specified by the user. Compared to online mode, the offline mode has an additional advantage, among others, that it can make use of the off-source sky subscan after the on-source subscan, and interpolate the observed sky brightness before fitting the atmospheric model. This presumably leads to more accurate atmospheric calibration.

The workflow of *kalibrate*, the procedures in which the data of various observing modes are processed, and the content of the output data<sup>1</sup> are described in this chapter.

### *4.1 The calibration workflow*

On start-up of *kalibrate*, it reads in the data of the reference atmosphere (the CIRA86), the tabular radiative transfer model (the atm-table, see the previous chapter)<sup>2</sup>, and collects the instructions from the command line and the configuration files.

After this has been finished, the program proceeds with the next

<sup>1</sup> The content of the input data is defined by *kosma\_control*, which is another component of the KOSMA-Software that controls the operation of the telescope and collects the raw data from the backends.

<sup>2</sup> Although loaded on every start-up, the CIRA86 and the atm-table may not be used if the command line options instructs *kalibrate* to use other models.

step and loads the raw data files of each scan into memory to do the calibration. Depending on the observing mode of the scan loaded, the program may read in additional scans that are needed for calibration.

The raw data of the calibration scan and sky measurements (which may be interpolated across observing date and time) are then used to compute the gain of the telescope system and the atmospheric attenuation. In the end of the calibration procedure, the raw data of the on-source subscan are converted to brightness temperatures using the gain and attenuation obtained above.

Various callback functions can be defined in the configuration files of *kalibrate*. These functions will be called before or after each step of the calibration workflow. In this way, a user of *kalibrate* can manipulate the internal data structures and the parameters of the algorithms. In this sense, the configuration files of *kalibrate* can be considered as command files, and are therefore named as *kalibraterc*.

Detailed descriptions of the implementation of the calibration steps, the data structures and function interfaces exposed to *kalibraterc*, and the format of the output data are available as self-documented source code in the *KOSMA-Software* repository<sup>3</sup>.

## 4.2 Calibration in different observing modes

The observing modes supported by *KOSMA-Software* can be categorized as calibration scans and sky measurements. Calibration scans, or LOAD scans are used to calibrate the gain of the telescope system<sup>4</sup>. During a calibration scan, the receiver only measures the signals from within the telescope system, and does not make use of the signal from the sky. A scan that measures the signal from the sky can be as simple as a LOAD scan followed by a subscan towards the sky<sup>5</sup>, pointed or on-the-fly (OTF) position switch total power observations, beam switch or load switch observations. The calibration formulae for these observing modes are listed below.

### Calibration of LOAD scan

The LOAD scan, sometimes referred to as calibration scan, is used to obtain the calibration factor that converts the raw backend output into brightness temperatures. A LOAD scan comprises an optional subscan that measures the quiescent output  $Z$  of the backend<sup>6</sup>, a subscan on the cold load, and a subscan on the hot load in sequence. The hot and cold loads are blackbodies whose temperatures are uniform and known as  $T_{\text{hot}}$  and  $T_{\text{cold}}$ , respectively. The raw data of the backend output are digitized by analog-digital converters. Because they

<sup>3</sup> The *KOSMA-Software* repository is password protected. Instructions to access the repository is available at <http://www.astro.uni-koeln.de/nanten2/node/106>.

<sup>4</sup> Another observing mode that calibrates the center frequency and resolution of the system, namely the COMB mode, is deprecated with the retirement of the acousto-optical spectrometers (AOS). It is supported for backward compatibility but not discussed in this thesis.

<sup>5</sup> The observing mode comprises the COLD / HOT / SKY sequence is called SKY scan.

<sup>6</sup> The quiescent output comes from e.g., the dark current of the CCD for an AOS backend. For backends that have no quiescent output,  $Z$  is exactly zero.

are 32-bit integer values by convention, the raw backend output of hot and cold load measurements are called the hot and cold “counts”, and are denoted by  $C_{\text{hot}}$  and  $C_{\text{cold}}$ .

The raw counts  $C$  and the counts of the quiescent output  $Z$  are both proportional to the exposure time of the observation, provided that the backend does not saturate. All the raw counts in the following formulae denote the values normalized to an exposure time of one second.

$$C = \gamma (T_A + T_{\text{rec}}) + Z, \quad (4.1)$$

where  $T_{\text{rec}}$  is the noise temperature of the system, and  $T_A$  is the antenna temperature of the input signal, which can come from the load (in a LOAD scan), or from the sky<sup>7</sup>. The system gain  $\gamma$  defined as the ratio between the differences in of the input brightness temperatures and output raw counts:

$$\Delta C = C_2 - C_1 = \gamma (T_{A,2} - T_{A,1}) = \gamma \Delta T_A. \quad (4.2)$$

The  $T_A$ , or the brightness of the input signal seen by the mixer during a load scan, is

$$T_{A,\text{cold}}^{\text{hot}} = G_s x_s \mathcal{J}_{v_s}(T_{\text{cold}}^{\text{hot}}) + G_i x_i \mathcal{J}_{v_i}(T_{\text{cold}}^{\text{hot}}) + (1 - x_s) G_s \mathcal{J}_{v_s}(T_{\text{term}}) + (1 - x_i) G_i \mathcal{J}_{v_i}(T_{\text{term}}), \quad (4.3)$$

where the terms follow the same notation as in Equation 1.5, explained on page 20. The system gain at each spectrometer channel can be expressed as

$$\gamma = \frac{C_{\text{hot}} - C_{\text{cold}}}{T_{A,\text{hot}} - T_{A,\text{cold}}}, \quad (4.4)$$

where the indices of spectrometer channel is omitted from each term.

The receiver noise temperature  $T_{\text{rec}}$  can be obtained from gain calibration with Equation 4.1. In practice, only the parts of the passband where the receiver response to input signal is high enough to derive a system gain with satisfactory S/N ratio, and the  $T_{\text{rec}}$  is low enough so that its drifts and fluctuations do not have negative impacts on calibration accuracy (see Sections 5.5 and 6.4 for explanation), are used for fitting the atmospheric model. The rest of the bandpass, where the receiver response to the input signal is low due to the limited bandwidth or interference and etc., or the where receiver noise is so high that its drift and fluctuation may introduce significant errors to observation, is identified as “bad channels”. A spectrometer channel is identified as bad where the gain is below the threshold

$$\gamma_{\text{th}} = \alpha \cdot \gamma_{\text{max}}, \quad (4.5)$$

or the receiver noise exceeds the frequency dependent threshold of receiver temperature

$$T_{\text{rec},\text{th}} = \beta \cdot \frac{h\nu_{\text{LO}}}{k}, \quad (4.6)$$

<sup>7</sup> It should be noted that the term of “antenna temperature” is a general concept in electrical engineering and has nothing to do with the primary and secondary mirrors of a Cassegrain telescope, or any of the main beam and forward efficiencies in the case of a LOAD scan. The emission of the load at a known load temperatures (effective, see page 20) is coupled to the mixer through different optical paths than that of the sky signal.

or found to contain a single-channel spike. The  $\gamma_{max}$  is the maximum receiver response across the passband, and  $\alpha$  is an arbitrary factor which defaults to 0.01. The  $\nu_{LO}$  is the LO frequency<sup>8</sup>, and the factor  $\beta$  defaults to 200. Both  $\alpha$  and  $\beta$  can be configured independently for each frontend-backend combination.

<sup>8</sup> The LO frequency is used to approximate  $\nu_s$  and  $\nu_i$  because they are close enough for the accuracy needed for bad channel identification.

### Calibration of SKY scan

The SKY scan is essentially a LOAD scan followed by a measurement (subscan) towards the sky. It is used to determine the atmospheric transmission with the help of an atmospheric model. The measured antenna temperature

$$\begin{aligned} T_{A,sky} &= (1 - f_{amb}) \times (G_s x_s T_{A,sky,\nu_s} + G_i x_i T_{A,sky,\nu_i}) \\ &+ f_{amb} [G_s x_s \mathcal{J}_{\nu_s}(T_{amb}) + G_i x_i \mathcal{J}_{\nu_i}(T_{amb})] \\ &= \gamma^{-1} (C_{sky} - C_{hot}) + T_{A,hot}, \end{aligned} \quad (4.7)$$

where  $C_{hot}$  is subtracted from  $C_{sky}$  in order to remove the receiver noise level from the spectrum of a SKY measurement. Other terms follow the same notation as in Equation 1.5, explained on page 20. The sky brightnesses on the signal and image frequencies,  $T_{A,sky,\nu_s}$  and  $T_{A,sky,\nu_i}$ , are computed with an atmospheric model and fitted to the measured  $T_{A,sky}$ .

### Calibration of total-power position-switch observations

In a *total-power* (TP) pointed *position-switch* (PSW) observation, the telescoped measures single on-source (ON) and off-source (OFF) positions on the sky. The OFF is then subtracted from the ON, creating a difference which is essentially the response of the telescope system to the signal of the celestial source<sup>9</sup>

$$T_{A,source} = \frac{C_{on} - C_{off}}{\gamma \exp(-\tau_{\nu,s})}, \quad (4.8)$$

where  $\tau_{\nu,s}$  is the optical depth of the atmosphere at the signal frequency fitted with an atmospheric model to the OFF measurement. The OFF is measured shortly before or after the ON within the duration limited by receiver stability. There may be one or more ONs between adjacent OFFs. The contributions of the quiescent output and the receiver noise in  $C_{off}$  are expected to be close to that in  $C_{on}$ . The OFF position is also chosen to be as close to the ON as possible especially in elevation so that both measurements measure nearly the same column of air through the atmosphere, and most of the atmospheric emission can be canceled out.

<sup>9</sup> This is the ideal case. In practice, the difference also includes the drift of the receiver system and the difference of the atmospheric emission between the line of sight towards the ON and OFF positions. It also includes the negated celestial signal at the OFF position, which is very weak when the OFF position is *clean*.

A variant of the total-power position-switch observing mode is the *on-the-fly* (OTF) mode. In an OTF observation, ON and OFFs are interleaved just as in the pointed observing mode, but the telescope slews continuously during the ON subscans, resulting in an equivalent beam shape that is elongated. This effect makes no difference in atmospheric calibration.

#### *Calibration of beam-switch observations*

Beam-switch (BSW) is the observing mode that the telescope beam is switched between two positions on the sky during observation by driving the secondary mirror (the “subreflector”) to pre-selected end limits periodically. The secondary mirror is more lightweight compared to the primary mirror, allowing the beam to switch or move faster than in total power observations. However, the spatial distance between ON and OFF in the BSW mode is also smaller, typically only a few arc-minutes, than that in PSW mode, which can be up to one degree in most cases. For this reason, the BSW mode is used to observe compact sources that are known to be smaller than the chop throw of the subreflector. The advantages of the *beam-switch* (BSW) observing mode over total-power position switch are that the ON and OFFs are close in time, and the overhead of the observing time used to move between ON and OFF is reduced. The time to move between ON and OFFs are usually reduced from about half a minute (which is of the same order as the integration time of the ON and OFF measurements) to about one second<sup>10,11</sup>.

In *kalibrate*, it is possible to specify the range of OFF measurements within a BSW mode OTF scan that is used for atmospheric model fitting. This is useful when the chopper phase which is supposed to be off the source is not always pointing to a position that is free from astronomical signals (e.g., in the case when the chop throw is along the direction of the OTF scan). All the OFF measurements within the specified range are averaged before being fitted by the atmospheric model in order to get higher S/N ratios. The formula that converts raw data into antenna temperature of the source is the same as Equation 4.8, which is for PSW observations. However, the atmospheric opacity  $\tau_{v,s}$  is fitted to the sky brightness averaged over the whole OTF scan instead of that from the previous, closest, or interpolated OFF measurement (depending on the command line options of *kalibrate*).

#### *Calibration of load switch observations*

In all the observing modes discussed above, the sky brightness to which the atmospheric model is fitted is calibrated with the previous

<sup>10</sup> Generally, both switching times are longer for larger telescopes and vice versa.

<sup>11</sup> These values are typical for the NANTEN2 telescope. The time to move between ON and OFF has been reduced to a few seconds, and the beam switching time is a few hundred milliseconds for the SOFIA telescope.

HOT and COLD measurements. For PSW and BSW observations,  $C_{hot}$  comes from the previous LOAD scan, which is usually up to ten or fifteen minutes ago. The level of  $T_{rec}$  may have drifted by a significant amount compared to that of  $T_{A,sky}$ . This tends to be more problematic when  $T_{rec}$  is much higher than  $T_{A,sky}$ . In the case of GREAT observations, for example,  $T_{rec}$  is typically two orders of magnitude higher than  $T_{A,sky}$ . A drift of  $T_{rec}$  by  $10^{-3}$  will translate into a ten percent error of the modeled atmospheric transmission, which is intolerable. The drift of  $T_{rec}$  between the hot load measurement and the sky measurement from which the atmospheric transmission is derived (either the OFF subscan or the SKY subscan) can be minimized by measuring the hot load more frequently.

During a load switch (LSW) observation, the ON and OFFs are measured just like in the PSW mode except that the hot load is measured after each ON and OFF. Consequently,  $T_{A,source}$  is given by

$$T_{A,source} = \frac{(C_{on} - C_{hot,on}) - (C_{off} - C_{hot,off})}{\gamma \exp(-\tau_{v,s})}, \quad (4.9)$$

where  $C_{hot,on}$  and  $C_{hot,off}$  are the raw counts of the hot load measurements after the ON and OFF, respectively. The optical depth of the atmosphere,  $\tau_{v,s}$ , is fitted with the atmospheric model on the sky brightness derived from Equation 4.7 after replacing  $C_{hot}$  with  $C_{hot,off}$ .

The problem that LSW observation is intended to handle can also be solved by improving receiver stability. In practice, the LSW observation mode is rarely used because of its low time efficiency. During a LSW scan, only 25% of the integration time is spent on the celestial source. The overhead of the observing time also increases due to the frequent switching between sky and load.

#### *Frequency switch, sky dips, and etc.*

Some observing modes supported by the telescope hardware and the telescope controlling utilities in KOSMA-Software are not discussed in the following chapters.

The BSW observing mode improves observing time efficiency over TP / PSW by reducing the time needed to move between the ON and OFF positions. Frequency switching, or FSW, further reduces overhead by switching the LO frequency, which needs no mechanical operation. However, the atmospheric transmission at the sub-mm band changes very fast over frequency. The basic idea of FSW that the atmospheric transmissions of nearby frequencies are almost the same is invalid at sub-mm wavelengths. Therefore, FSW calibration is not discussed in this thesis.

The observing sequence of sky dip scan is the same as that of SKY scan, which is discussed in Section 4.2, except that the measurement on the SKY is not a pointed observation towards a specific direction, but an OTF scan along the elevation direction. In the next chapters where the application of this calibration scheme to NANTEN2 / SMART and SOFIA / GREAT is discussed, pointed measurements at different elevations using SKY scans are used instead of skydips<sup>12</sup> to study the properties of the atmosphere. The analysis of skydips is expected to be a future work as an extension of this thesis.

<sup>12</sup> For some time the SOFIA telescope did not support skydips when using the GREAT receiver.



## 5

# *Application to NANTEN2 / SMART*

The NANTEN2 observatory is located at Pampa la Bola of the Atacama desert in Chile at  $-67^{\circ}42' E$ ,  $-22^{\circ}58' N$ , at an altitude of 4865 m<sup>1</sup>. It is a joint operation by University of Cologne, University of Bonn, Nagoya University, Osaka University, University of Chile, ETH Zürich, University of New South Wales, and Seoul National University. The University of Cologne has contributed the SMART receiver which operates at 460 ~ 490 and 800 ~ 880 GHz<sup>2</sup>. Apart from the SMART sub-millimeter array receiver, NANTEN2 also has a millimeter receiver that has been built at Nagoya University and can observe at 115 and 230 GHz. This millimeter receiver observes during most of observing season when the atmospheric transmission is too low for sub-mm observations. The telescope of NANTEN2 is a four-meter Cassegrain reflector. Only the total power position switch observing modes (pointed and OTF, see Section 4.2) are used for NANTEN2 / SMART.

<sup>1</sup> <http://www.astro.uni-koeln.de/nanten2>

<sup>2</sup> These are the tuning ranges of SMART local oscillator claimed by Graf et al. (2008). The actual tuning ranges are 435 ~ 495 GHz and 795 ~ 880 GHz.

### *5.1 Performance characteristics of SMART*

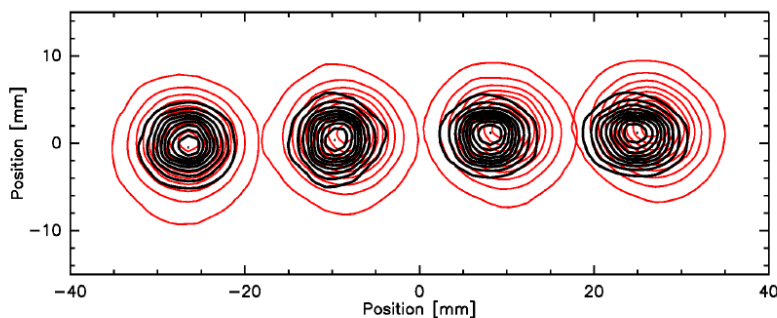
The sub-mm receiver of NANTEN2 is SMART, which consists of two  $4 \times 2$  arrays of pixels working in the 460 / 490 and 810 GHz bands, respectively. The corresponding pixels of the two arrays are aligned in telescope beams as shown in Figure 5.1. Each pixel points to nearly the same position on the sky as that of the corresponding pixel on the other band. The local oscillator (LO) frequencies of both bands can be tuned continuously without gaps. Therefore, the 460 / 490 array receiver is also referred to as the 460 GHz (or 490 GHz) receiver. The LO can be considered as monochrome because its spectral line width is much narrower than the frequency resolution of the spectrometers. Calibration of the system gain is done by measuring hot and cold loads as explained in Section 4.2. The hot load is at ambient temperature and is nearly a blackbody at sub-mm wavelengths. The cold load is about 200 K colder than the hot load. The atmospheric transmission needs to be determined within an accuracy of a few

percent. This translates to an accuracy of a few Kelvins in  $T_{A,sky}$ . The data quality of the 460 GHz receiver is good enough for use in atmospheric calibration. However, the stability of the 810 GHz receiver is suboptimal. The 810 GHz data must be calibrated with the parameters of the atmospheric model fitted from the 460 GHz data as explained below.

## 5.2 NANTEN2/SMART specific considerations for the static atmospheric model

One of the advantages of an array receiver over a single-pixel receiver is that an array receiver allows for cross-checking of the calibrated sky brightnesses among different pixels that work at the same frequency. On the other hand, a multi-band receiver allows cross-checking of the fitted model parameters of the atmosphere between different frequencies. In this sense, a multi-band array receiver like SMART is a perfect instrument because it can help us to determine the origin of the systematic and random errors in atmospheric modeling, i.e., whether the model is imprecise, or the instrument is not stable enough, or both. For this perfect instrument, there are some specific considerations in atmospheric modeling.

### *Line-of-sight airmass of the array receiver*



The beams of the SMART high and low band receivers are spatially aligned as in Figure 5.1 so that the envelop of the half power beam widths of the sixteen pixels covers a roughly rectangular area of size  $0.05^\circ \times 0.1^\circ$  on the sky. Considering an elevation between 20 and 85 degrees, the maximal difference between the airmasses seen by different pixels is less than 0.5%. This difference is much smaller

Figure 5.1: Beam pattern of the  $1 \times 4$  dual band (eight-pixel) SMART receiver measured before being upgraded to sixteen pixels (figure from the NANTEN2 website <http://www.astro.uni-koeln.de/nanten2>). Black and red contours are for the 810 and 490 GHz receivers, respectively. The current SMART receiver has sixteen pixels in a  $2 \times 4$  pattern aligned in the same way. (A plot of the measured beam pattern of the current, sixteen-pixel SMART receiver is not available.)

than the error of the estimated P-T profile, which is typically larger than one percent. The difference in airmass among different pixels is also smaller by an order of magnitude than the uncertainty from the instrument according to the analysis in Section 5.3. As a result, the different pixels of the SMART receiver can be assumed to be observing through the same column of air in the atmosphere.

### *Water vapor above NANTEN2*

For SMART observations, the precipitable water vapor (pww) contributes most of the atmospheric attenuation. Its distribution is the most important factor of atmospheric modeling for NANTEN2 / SMART. The pww under good weather conditions may fall below 0.4 mm, giving a typical atmospheric transmission above fifty percent for most of the observations in the 460 GHz band. The time efficiency of 460 GHz observation becomes too low, and the calibration error increases significantly, when the pww rises above  $\sim 0.7$  to 1 mm. Observations in the 490 and 810 GHz bands require even better weather conditions.

The value of pww can be obtained in two ways: 1) Directly calculated from the humidity near the ground using a given vertical profile of water vapor, such as that in Equation 2.1, or 2) Fitted from the observed sky brightness with an atmospheric model.

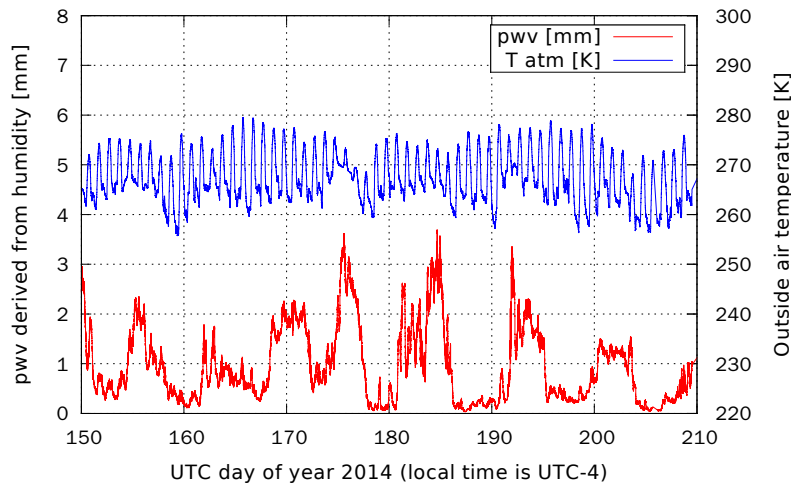


Figure 5.2: Modeled precipitable water vapor according to Equation 2.1, based on the humidity measured by the ground-based weather station at NANTEN2 with model parameters  $x_c = 2.5 \times 10^{-6}$ , and  $P_s = 3.5$ .

The pww's derived from the relative humidity measured with the weather station of NANTEN2 using Equation 2.1 with a typical value of the scaling factor  $P_s = 3.5$ , and according to the empirical formulae of saturated water vapor mixing ratio by Buck (1981), are shown in Figure 5.2. The modeled pww has a diurnal variation that

is superimposed over a strong, non-periodic fluctuations resulting from regional weather changes. The weather changes are visible from the envelope of the temperature curve, e.g., on the 174 and 192th day of the year 2014. The pwv's calculated with this method are coarse estimations that are expected to be accurate within one order of magnitude because it is affected by the error of  $P_s$  and by the evaporation from the ground, which can increase the measured humidity significantly.

As shown in Figure 5.3, the estimated values are roughly consistent with the values fitted from SMART observation data using an atmospheric model except in a few occasions, e.g., from the 163 to 166th and the 187 to 190th day of the year 2014. This means that the typical  $P_s$  is usually accurate enough for the estimation of pwv, but the occasional large discrepancy between the pwv values indicates that the ambient humidity measured near the ground cannot be used as a reliable indicator of the atmospheric transmission. The measured humidity is therefore not useful for site survey. For this purpose, a radiometer must always be used to determine the quality of the site regarding atmospheric transmission.

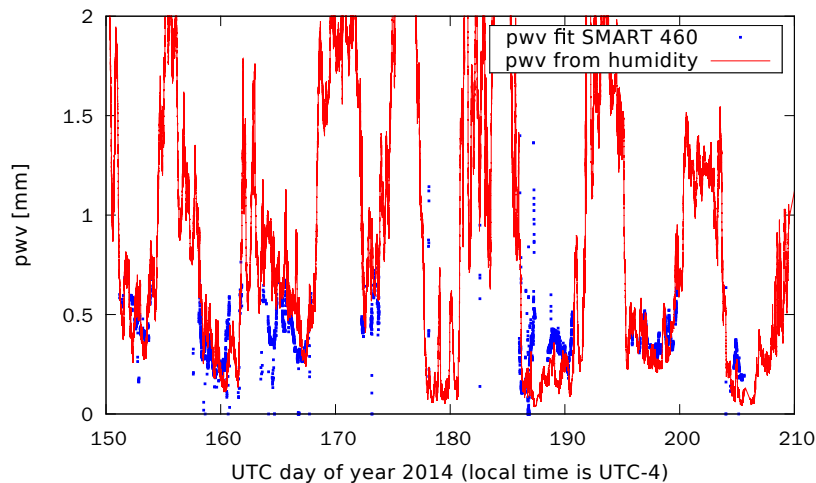


Figure 5.3: The pwv derived from the ambient humidity compared to that fitted with 460 / 490 GHz SMART data. No fitted data is available when the pwv is too high for SMART observations.

For ground based telescopes, fitting the sky brightness observed by the astronomical receiver with an atmospheric model is our only way of obtaining a quantitatively correct pwv and atmospheric transmission. The discrepancy of the typical value of  $P_s$  (see Equation 2.1) from its actual value has little effect on calibration accuracy in this case.

### Ozone above NANTEN2

Most of the NANTEN2 observations are focused on CO and CI. Unless the observation is affected by a large Doppler shift or velocity dispersion, these lines are almost unaffected by atmospheric ozone. Besides, the absorption by water vapor is so strong in typical weather, as seen in Figure 5.4, that it is rather difficult to derive the vertical distribution of ozone from the weak ozone lines observed. The strong absorption from water vapor across the whole passband also makes it possible to derive the total pwv as well as the water vapor vertical distribution despite of the slight inaccuracy in the ozone vertical profile. Therefore, we always use a reference ozone profile (see Section 2.4) for atmospheric calibration.

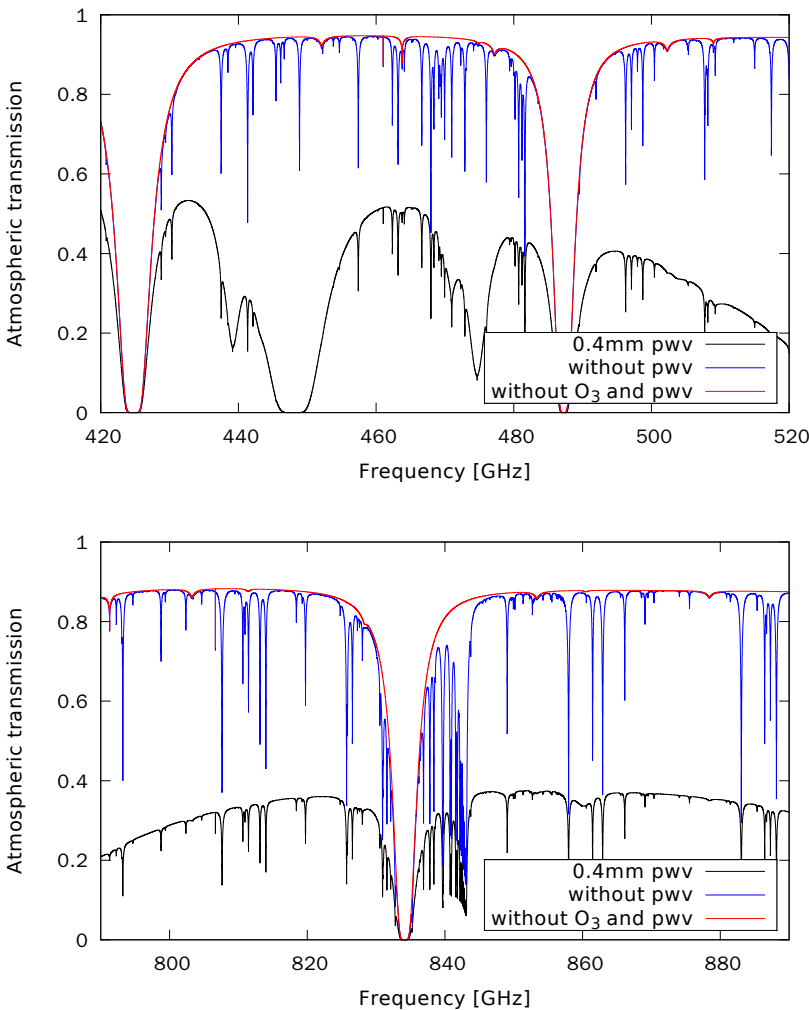


Figure 5.4: Atmospheric transmission at a typical telescope elevation ( $45^\circ$ ) above the NANTEN2 site in typical weather for SMART observations (pwv = 0.4 mm), through completely dry atmosphere (without pwv), and through a completely dry atmosphere without ozone. For most of the observations, the major absorbing species are water vapor (the difference between the black and blue spectra) and molecular oxygen (the wide red spectral lines, two in the 460 GHz band and one in the 810 GHz band).

*CO and other minor species*

There are two atmospheric CO lines within the frequency bands of SMART at 461.041 and 806.652 GHz. These are very narrow lines that come from the mesosphere. Similar to the stratospheric ozone lines, the mesospheric CO lines become very weak in the presence of the strong water vapor absorption from the troposphere. We do not attempt to model the vertical distribution of CO for SMART observations.

The effects of other minor species, such as N<sub>2</sub>O and CH<sub>4</sub>, on the atmospheric transmission are negligible, and invisible in the plots in Figure 5.4. The distribution of these gases are not considered in the atmospheric calibration of SMART observations.

### 5.3 NANTEN2/SMART specific considerations for the radiative transfer model

*Broadband CIA*

The broadband collision induced absorption (CIA, mainly by molecular nitrogen and oxygen) that accounts for the quasi-continuum component, or the “continuum level” of the dry air absorption at frequencies far from the spectral lines in Figure 5.4 is typically less than 20% of the total atmospheric absorption. Although Paine (2014) shows that the modeled CIA is a few percent different from lab measurements, the inconsistency is unimportant for SMART observations.

*Computing time limitation of online calibration*

Because the atmospheric CO lines are only one or two Megahertz wide at the frequencies of SMART, we have to model the atmospheric transmission of NANTEN2 at a resolution that is too high for real-time modeling with the AM model<sup>3</sup>. Online calibration with the AM model is impractical. Therefore, part of the code of the AM model was modified to make use of OpenCL<sup>4</sup> acceleration. Using OpenCL acceleration, online calibration with the AM model at sufficiently high frequency resolution can be made possible with minimal effort (i.e., by installing a supported graphics card at the NANTEN2 site).

<sup>3</sup> Optimization is possible, e.g., with varying frequency resolution across the passband. However, this has not been implemented yet.

<sup>4</sup> Open Computing Language (OpenCL) is a programming standard on heterogeneous systems used for massive parallel data processing.

## 5.4 Application of kalibrate to NANTEN2 / SMART

### *Sky brightness as a measure of atmospheric transmission*

Because the largest part of the atmospheric absorption comes from the broad water and oxygen lines as shown in Figure 5.4, the sky brightness changes little over the receiver passband ( $\sim 1$  GHz wide). The average sky brightness can be used as a measure of weather quality – the brighter the atmospheric emission, the lower the atmospheric transmission.

Large variation of the sky brightness take place on a timescale from half an hour to a few hours as shown in Figure 5.5, from about 50 to over 200 K.

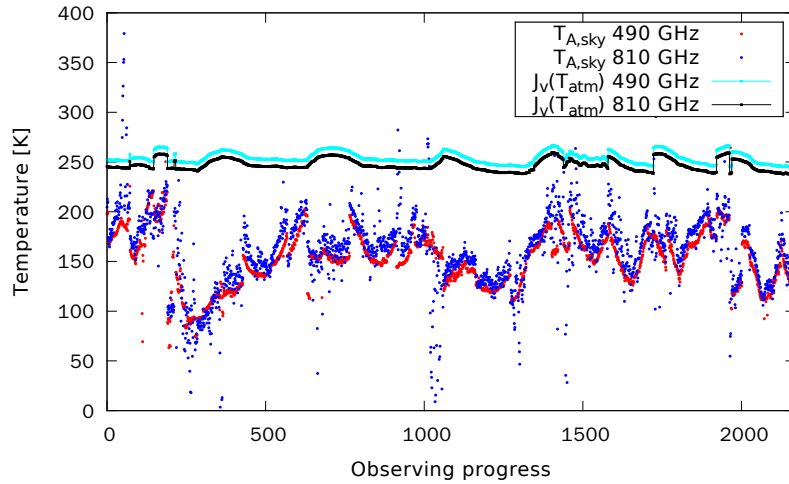


Figure 5.5: Average sky brightnesses from 2014-06-22 to 2014-07-25 over the passbands on the 490 (red dots) and 810 GHz (blue dots) bands compared to the ground-level air temperature after Rayleigh-Jeans corrections at the corresponding frequencies. The sky brightnesses are measured with pixel Nos. 6 and 14. The horizontal axis is the progress of observations, represented by sub-scan numbers towards the empty sky (OFF-source sub-scan). The typical interval between successive OFF measurements is about three minutes.

The variation of sky brightness is dependent on both the weather conditions, which can be measured by zenith transmission, and the telescope elevation, which is determined by the astronomical project (i.e., the source to be observe). The line of sight atmospheric transmission corresponding to the sky brightness in Figure 5.5 is less than 30% for most of the observations.

Because the atmosphere is so opaque (less than 30% transmission), and most of the attenuation comes from water vapor, which is concentrated close to the ground, it is reasonable to assume an altitude independent air temperature for the purpose of error estimation. Under this assumption, the measurement error of  $T_{A,sky}$  translates to a relative calibration error of

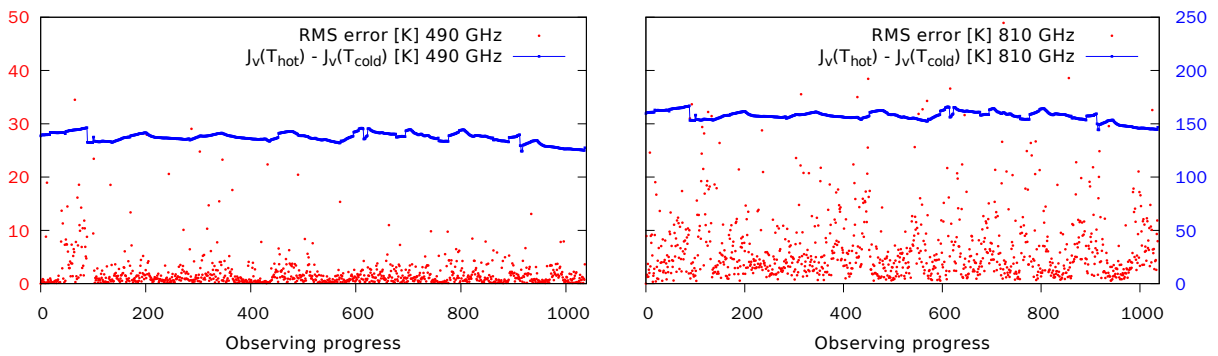
$$\Delta \approx -t_v^{-2} \Delta t_v, \quad (5.1)$$

where  $t_v$  is the atmospheric transmission:

$$t_v \approx 1 - T_{A,sky} / \mathcal{J}_v(T_{atm}). \quad (5.2)$$

At an atmospheric transmission below 30%, the error in  $T_{A,sky}$  is amplified by approximately an order of magnitude in the calibrated source spectra. Therefore, it is important to have an accurate gain calibration and keep the gain of the receiver system stable between successive LOAD scans.

### 5.5 Receiver stability: Test and effect



The brightness of the atmosphere is measured about every minute with an OFF measurement during regular telescope operations. During such short intervals, the receiver can be considered stable. The factors that affect the accuracy of the calibrated source brightness are the stability of the system gain,  $\gamma$ , and the accuracy of the sky transmission,  $\exp(-\tau_{v,s})$  in Equation 4.8. The calibration error is proportional to the relative error of  $\gamma$ , which is considered to be stable between frequent enough ( $\sim$  every 10 minutes) LOAD scans, and is sensitive to the error of  $T_{A,sky}$  in NANTEN2 / SMART observations as explained in the previous section.

#### Gain stability: Test and effect

The drift of system gain can be measured with “load calibrations”, which calculates the temperature difference between hot and cold loads according to gain measured by the previous calibration scan. The calibration formula is the same as Equation 4.8 except that the ON and OFF counts are substituted with HOT and COLD, and the forward efficiency is set to unity, i.e., the  $f_{amb}$  set to zero in Equation 4.7.

Figure 5.6: Gain drift shown by self-calibrated load temperature difference between the same pixels and during the same observing session as in Figure 5.5. Horizontal axes: Sequence number of calibration scan; Vertical axes: See legend. The frequency resolution is downgraded to 1.22 MHz by binning the spectrometer channels. The amount of drift is divided by  $(t_i/100s)^{1/2}$  before plotting, where  $t_i$  is the interval between the current load and the previous load that the current one is calibrated with (typically from about ten minutes ago). The same comparison for all pixels across several months can be found in Appendix A.

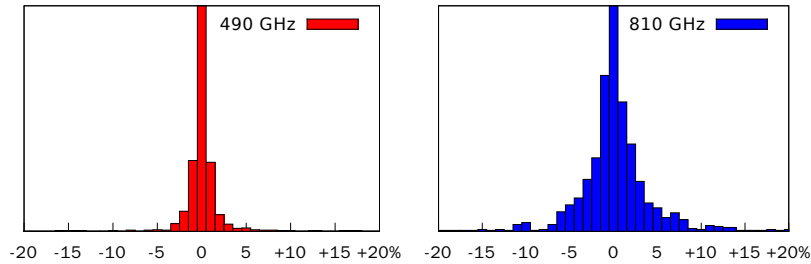


Figure 5.7: Same as Figure 5.6 but shows the number of *load calibrations* in histograms that represents the average gain drifts over the passband. Gain drifts in the central bin are less than 1%, the stability which is required when the atmospheric transmission is lower than  $\sim 30\%$ . The same comparison for all pixels across several months can be found in Appendix A.

In typical weather for SMART observations, the sky brightness as shown in Figure 5.5 is close to the temperature difference between the hot and cold loads. Therefore, the effect of gain variation on the measured sky brightness is expected to be similar to the error of calibrated  $\mathcal{J}_v(T_{hot}) - \mathcal{J}_v(T_{cold})$  in Figure 5.6, which is usually no more than two or three Kelvins. The plots in Figure 5.6 show the RMS difference over the passband between the HOT / COLD temperature difference calculated with load calibration, and that calculated from the temperature sensors' output (the cold load temperature measured by the sensor is corrected for the loss at the telescope optics, see explanation on page 20). The RMS values are used instead of the average value over the whole passband in order to detect frequency dependent gain variations, e.g., standing waves. With a stable receiver, the RMS errors in Figure 5.6 are expected to stay close to zero. At an atmospheric transmission below 30%, the calibration error of the source signal will likely<sup>5</sup> rise over 10% if the RMS of the load temperature difference over the passband exceeds 1  $\sim$  2%, or about 2 K. Therefore, gain stability is particularly important for observations under low atmospheric transmission.

Instead of showing the system stability between successive LOAD scans, the histogram of the relative variation of the average gain over the passband in Figure 5.7 allows the operator to quickly identify defective pixels<sup>6</sup>. The histogram should be symmetric, which means the gain drift does not impose a bias on calibration. An asymmetric histogram that indicates that the receiver is not well tuned.

In order to reduce the error of atmospheric calibration especially at low atmospheric transmission, the LOAD scans must be done more often than usual. The exact frequency needed to do LOAD scans can be determined by regular tests of gain stability using "load calibration".

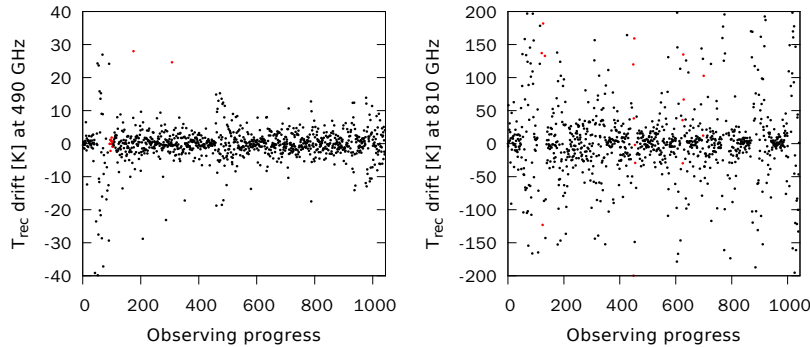
<sup>5</sup> This method of bad data detection is subject to false positives because the RMS can come from ripples over the passband, which usually does not affect atmospheric calibration.

<sup>6</sup> In contrast to the method of using the plot of RMS error which gives false positives, as explained in Footnote 5, using histograms is prone to false negatives in bad data detection because the instability may be averaged out over the passband.

### Receiver temperature stability: Test and effect

As mentioned above, the accuracy of atmospheric calibration is also affected by the error of  $T_{A,sky}$ . Because  $T_{A,sky}$  is calculated from the system gain and the hot load measurement, as seen in Equation 4.7, both the gain and the receiver noise must be stable in order to obtain an accurate  $T_{A,sky}$ . The effect of gain variations on the atmospheric calibration was analyzed above. The drift of the receiver noise temperature  $T_{rec}$  may also impact the calibration accuracy because measurements toward the sky can occur up to 10 or 15 minutes after the hot load measurement. In this time the  $T_{rec}$  may have drifted by more than a few Kelvins, resulting in an error of over  $\sim 1\%$  on the  $T_{A,sky}$  calculated from Equation 4.7<sup>7</sup>. For NANTEN2, which is incapable of doing load switch observations (see Section 4.2)<sup>8</sup>, the only way for an observer to reduce this kind of error is to do LOAD scans more often, especially at low atmospheric transmission.

The typical receiver noise temperatures (SSB scale) of SMART are 200 to 600 K for the 460 / 490 GHz band and 800 to 1600 K for the 810 GHz band. The precise value depends on LO frequency, adjustment of the LO optics, mixer bias, etc. Figure 5.8 shows the drift of  $T_{rec}$  for the same observing days as in Figure 5.5. The drift of  $T_{rec}$  affects  $T_{A,sky}$  via Equation 4.7.



A comparison between Figures 5.6 and 5.8 indicates that the error introduced to  $T_{A,sky}$  by gain drift and  $T_{rec}$  drift is on the same order of magnitude in each band.

### 5.6 Effect of forward efficiency error on calibration

The forward efficiency

$$\eta_{fw} \equiv 1 - f_{amb}$$

is different for different pixels. However, the same  $\eta_{fw}$  is assumed for all pixels of SMART. The discrepancy between the actual and

<sup>7</sup> This kind of instability is less a problem in the data reduction of other observing modes, e.g., for Equation 4.8, because ON and OFFs are close in time.

<sup>8</sup> Load switch observation with NANTEN2 / SMART can be implemented by changing KOSMA-Software. However, whether the possible decrease of time efficiency introduced by this observing mode is an issue or not must be considered.

Figure 5.8: Same as Figure 5.6 but shows the median values of the receiver temperature (single-sideband scale, same below for receiver temperatures) differences between successive calibration scans in Kelvins. Horizontal axes: Sequence number of calibration scan. The interval between successive data points (load scans) is typically about ten minutes. The few red dots mark bad data where more than 2/3 of the passband consists of bad channels (see the definition of “bad channel” on page 45). The same comparison for all pixels across several months can be found in Appendix A.

the assumed forward efficiencies should not be much more than 1% because  $f_{amb}$  itself is only 7%. Assuming an altitude independent air temperature,

$$T_{A,sky} = \mathcal{J}_v(T_{atm}) (1 - e^{-\tau}). \quad (5.3)$$

Consider the error of measured  $T_{A,sky}$  due to a small error in  $\eta_{fw}$ ,

$$\begin{aligned} \because \eta_{fw} dT_{A,sky} &= -\mathcal{J}_v(T_{amb}) df_{amb} \\ \therefore \frac{d\tau}{d\eta_{fw}} &= \frac{e^{\tau} \mathcal{J}_v(T_{amb})}{\eta_{fw} \mathcal{J}_v(T_{atm})}. \end{aligned} \quad (5.4)$$

Because the optical depth of the atmosphere is almost linearly dependent on the pwv according to Equation 3.1, the fitted pwv is expected to deviate from the average value, which is expected to be a close estimation of the real pwv, especially at higher pwv's according to Equation 5.4. This kind of deviation is visible in Figure 5.9, e.g., for pixels 4 and 5 of the 490 GHz band.

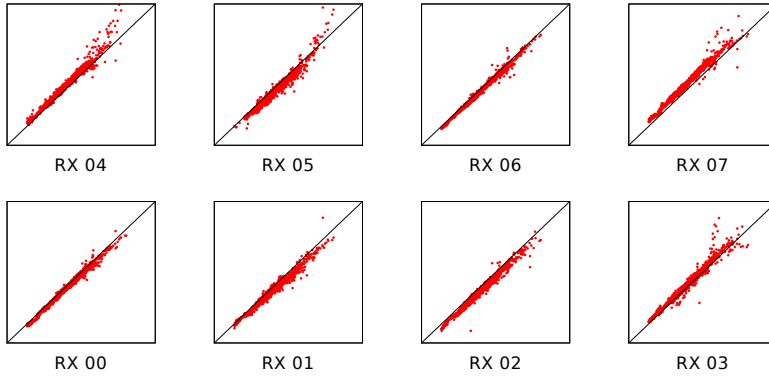


Figure 5.9: Fitted pwv's from each pixel of the 490 GHz band compared to the pwv averaged over all 490 GHz pixels except pixel 5. For pixel 5, no valid data from a period of observations at very good weather (pwv less than 0.2 mm) is available. Axis limits are 0 to 1 mm for both axes.

### 5.7 Effect of load temperature error on calibration

The conversion factors between the temperature of the cold load and the "effective cold load temperatures (see Section 1.4)" for the 460 / 490 GHz receiver pixels have been measured before. The same measurement have not been done for the 810 GHz pixels.

The fact that the fitted pwv's from different pixels of the 460 / 490 GHz band are consistent (as shown in Figure 5.9), and that they are usually also consistent with the estimated pwv from the humidity (shown in Figure 5.3) shows that the effective load temperatures are reasonably accurate.

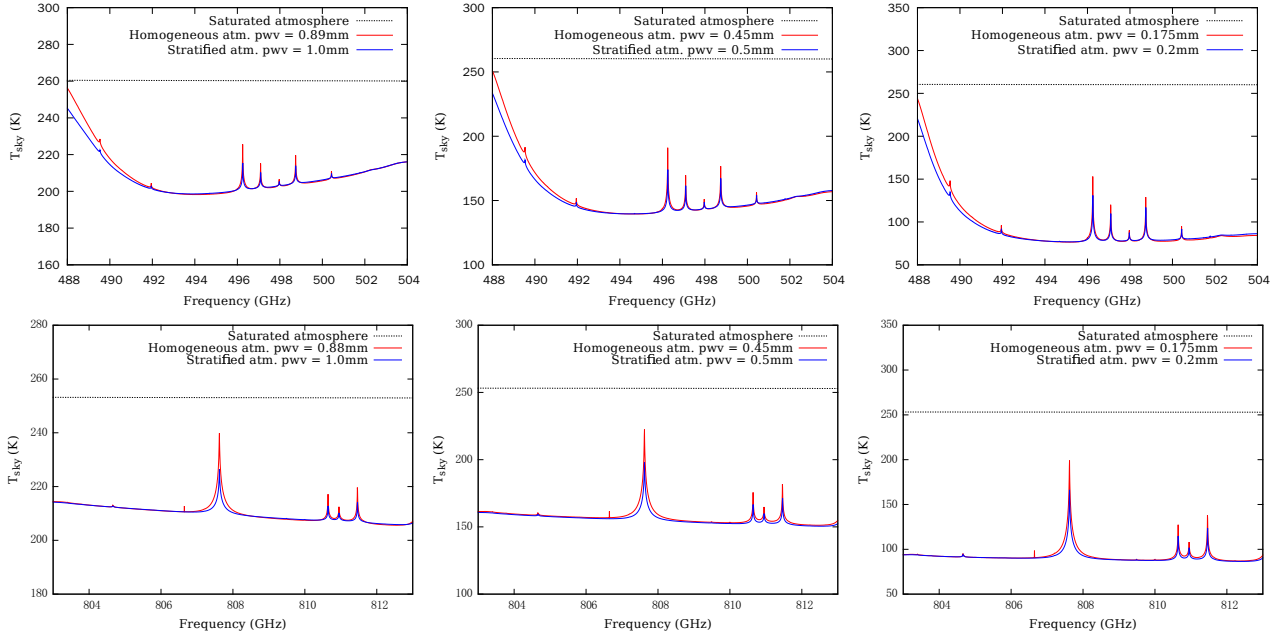
Similar corrections are not applied to the 810 GHz load temperatures. Assuming Equation 5.3, and let  $C_{sky}$  be the raw counts of

the sky measurement where the effect of the emission from ambient material has already been removed, then

$$\begin{aligned} \therefore T_{A,sky} &= \mathcal{J}_v(T_{hot}) + \frac{C_{sky} - C_{hot}}{C_{cold} - C_{hot}} \cdot (\mathcal{J}_v(T_{cold}) - \mathcal{J}_v(T_{hot})) \\ \therefore \frac{\mathcal{J}_v(T_{cold}) d\tau}{d\mathcal{J}_v(T_{cold})} &= \frac{\mathcal{J}_v(T_{hot})/\mathcal{J}_v(T_{cold}) + 1 - e^\tau}{\mathcal{J}_v(T_{hot})/\mathcal{J}_v(T_{cold}) - 1}. \end{aligned} \quad (5.5)$$

For NANTEN2, Equation 5.5 is close to zero when the line of sight optical depth is a little bit smaller than unity. According to Figure 5.4, this corresponds to about 0.4 mm pwv at typical elevation. Figure 5.10 also shows that the 490 and 810 GHz fitted pwv's are consistent around 0.4 mm. (The data points in Figure 5.10 are more dispersed at pwv's over  $\sim 0.5$  mm, where the atmospheric transmission is low. This is due to the amplified effect of receiver instability discussed in the previous two subsections.)

### 5.8 Effect of using the atm-table to compute radiative transfer



For all the analysis above we have used the AM model directly with the static atmospheric model discussed in Chapter 2. However, the default radiative transfer model used at NANTEN2 is the atm-table approach as explained in Section 3.4 but with a table generated using the ATM instead of the AM model. This approach assumes a constant air temperature for all altitudes.

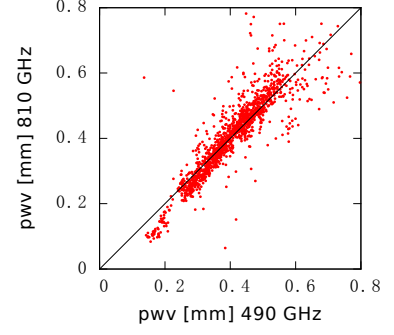


Figure 5.10: Comparison between the fitted pwv's from 490 and 810 GHz data. The 490 GHz pwv's are averaged over pixels 0  $\sim$  4, 6, and 7, while the 810 GHz pwv's are averaged over pixels 12  $\sim$  15.

Figure 5.11: Homogeneous and stratified atmospheric temperature model resulting in nearly the same sky brightness at different pwv's (assuming the dry adiabatic lapse rate).

Assuming a typical water vapor scaling factor of  $P_s = 3.5$ , only about 40% of the water vapor is concentrated in the bottom 1 km of the atmosphere. The weather data of NANTEN2 and CCAT<sup>9</sup> give a temperature gradient of about 6 to 8 K/km along altitude. Most of the water vapor must be in the higher layers that are more than 6 K colder than the air temperature near the ground. It is therefore expected that the fitted pwv is underestimated by fitting the atmospheric emission with the radiative transfer model using atm-table. The underestimation is strongly dependent on the temperature gradient, and varies with frequency. For the 492 [500] and [806]809 GHz (signal [image] sideband) atmospheric windows, as seen in Figure 5.11, the underestimations fall between 10% and 13% across a wide pwv range of 0.2 to 0.9 mm. This systematic error is intolerable for the calibration accuracy aimed by our calibration procedure.

<sup>9</sup> CCAT meteorological data is available from its website: <http://www.ccatobservatory.org>.

At present, the software setup at NANTEN2 uses the atm-table approach by default. The AM model can be used directly with the command line switch `"-a //am"` when running *kalibrate*. The AM model should be used for the final data calibration, while the atm-table approach, which is less computationally intensive, can be used for online monitoring.

## 5.9 Conclusion

For the gain calibration and atmospheric calibration in the particular case of NANTEN2 / SMART, the drifts of both the system gain and the receiver temperature pose a problem to accurate atmospheric calibration. As a result, the calibration accuracy under typical weather conditions is marginal regarding the aim of a few percent calibration error for the 460 / 490 GHz band if LOAD scans are done every about 100 s. The actual interval between LOAD scans is 600 ~ 900s in almost all SMART observations. Measuring a LOAD more often than every two minutes will severely impact time efficiency. Assuming that the atmospheric transmission changes on a longer timescale, typically on the order of ten minutes, a workaround is to use the OFF measurement for ON / OFF subtraction only, and use the atmospheric transmission measured by a SKY scan (see Section 4.2 on page 46) for atmospheric calibration.

A more consistent model fit of the 460 / 490 GHz data among all the pixels is necessary to measure the actual forward efficiency for each pixel individually.

The stability of the 810 GHz receiver is not sufficient for atmospheric modeling. Therefore, the parameters of the atmospheric model derived from the 460 / 490 GHz data should be used for

810 GHz calibration.

The effective cold load temperature of the 810 GHz band should be measured (the bare load temperature without correction for the loss at the optics is used at present) because the calibration is significantly off in very good weather, and only accurate at medium water vapor as shown in Figure 5.10.

Using the atm-table for atmospheric modeling can result in a systematic calibration error over 10% (see Figure 5.11). The AM model can be used instead to achieve better accuracy.

# 6

## *Application to SOFIA / GREAT*

The Stratospheric Observatory for Infrared Astronomy (SOFIA) is an airborne observatory that operates at an altitude around the tropopause (Gehrz and Becklin, 2010). SOFIA flies above most of the atmospheric water vapor, allowing sub-mm observations at higher frequencies than using ground-based telescopes. One of the instruments onboard SOFIA is the German REceiver for Astronomy at Terahertz frequencies (GREAT) whose working frequency ranges from 1.2 to 4.7 THz (Heyminck et al., 2012). The implementation of the atmospheric model, an analysis of the calibration results and the conclusions are presented in this chapter.

### *6.1 Performance characteristics of GREAT*

GREAT has only one pixel per frequency band. There are four frontends, or “channels” available, at most two of which can be configured to operate simultaneously before each flight. The frequency ranges covered by each frontend are listed in Table 6.1. The LO frequencies are so stable that they can be considered monochrome<sup>1</sup>, i.e., the spectral line width of the LO is beyond the resolution of the XFFTS backend (88.5 kHz).

<sup>1</sup> Except for the H channel, whose data we do not use for atmospheric modeling.

Table 6.1. Working frequencies of GREAT

Frontend	LO Freq. [THz]	Used for this thesis
L1	1.25 ~ 1.39 1.42 ~ 1.52	Y
L2	1.80 ~ 1.90	Y
Ma	2.49 ~ 2.56	Y
Mb	2.67 ~ 2.68	N
H	4.745	Y

The receiver temperatures of GREAT are of the order of  $10^3$  K for all channels, about  $10^2$  times of the sky brightness at the observing frequency, or an order of magnitude higher than the sky brightness near saturated (optically thick) atmospheric lines. As of early 2015, most spectroscopic data of GREAT are available from both the AFTTSes and XFTTSes<sup>2</sup>. Because the XFTTS has larger bandwidth, higher resolution, similar baseline quality and noise level (when smoothed to the same resolution) compared to the AFTTS, our investigation into atmospheric calibration is based on XFTTS measurements exclusively. It is assumed that the FFTS backends do not introduce instability and non-linearity to the system.

<sup>2</sup> These are the Fourier Transform spectrometers used in GREAT observations.

The main beam of the SOFIA telescope, which is about 20" for the GREAT L1 channel, and smaller for the other channels, accounts for more than half of the forward efficiency. For atmospheric calibration, we take it for granted that almost all of the power picked up by the forward beams (main beam and error beams) come from a very narrow solid angle in which the line-of-sight airmasses and the properties of the air can be considered the same, respectively.

## 6.2 *SOFIA/GREAT specific considerations for the static atmospheric model*

Atmospheric calibration for GREAT data relies on multi-band model fitting to get reliable results. The model parameters to fit and their ranges are quite different from that of atmospheric model for SMART calibration. There are mainly two problems in the atmospheric calibration for GREAT. One is that the profiles of some strong and narrow (as compared to the receiver's bandwidth) atmospheric lines, mostly from water and ozone, do not fit well between model and observation using the reference P-T profile and typical profiles of vertical distribution. The other problem, which has already perplexed us in ground based observations<sup>3</sup>, is the inconsistency of fitted pwv between different bands. The second problem is worse for GREAT because the modeled sky brightness is often either higher than observed even with a completely dry atmospheric model, or can only fit to observation with a pwv that is several times more than expected by meteorological knowledge. Both extreme cases are physically impossible, and will definitely degrade calibration accuracy, either across the whole band, which inevitably affects the source signal, or within a portion of the bandpass, which makes accurate calibration a risky task. The impact of these problems can be minimized with a more complex static atmospheric model.

<sup>3</sup> See Figure 5.10 on page 61.

### *Water vapor above SOFIA, effect on observation planning*

The water vapor column density above the tropopause, which is a few microns, always makes up more than 10%, and sometimes all of the total pwv. Because the major part of the pwv is widely distributed along altitude, both its vertical distribution and the P-T profile have major influence on atmospheric calibration.

In order to model a reasonably accurate vertical profile of water vapor mixing ratio, the scaling factor  $P_s$  in Equation 2.1 must be fitted<sup>4</sup>. The value of  $P_s$  should usually fall between -1 and 4, as explained in Section 2.3.

For SOFIA observations closely below the tropopause, neither the positive value that is for the troposphere nor the negative value that is for the stratosphere is a good approximation to use for  $P_s$ . In this case, another scaling factor may need to be introduced to Equation 2.1<sup>5</sup>. In this thesis, however, we are dealing with either low flights or high flights, and a single  $P_s$  is usually sufficient. With a given P-T profile, the water vapor scaling factor can be obtained by fitting the profiles of water lines.

However, most of the observations are carried out at frequencies far from strong water lines. The water vapor emission in an observation typically appear as a weak, slow slope across the passband. One can often fit the slope with virtually any  $P_s$ . The values of  $P_s$  and the total pwv are no longer independent in this case. i.e., The sky emission can be fitted with little residue in a wide range of  $P_s$ . For reliable model fitting of water vapor distribution, the LO frequency should be carefully chosen to include proper water lines in the image or signal sideband, while still puts the source signal to an optimal range of the passband where the receiver temperature is low.

### *Ozone above SOFIA, effect on observation planning*

The ozone layer, which holds most of the atmospheric ozone, extends from about 15 km (just above the SOFIA flight altitude), to about 40 km<sup>6</sup>. According to meteorological experiments performed by, e.g., the NEUBrew network (Disterhoft et al., 2008) and GOME-2 (Callies et al., 2000), the range on the P-T profile that the ozone layer occupies is roughly between 200 and 270 K from 1 to 140 hPa.

The FWHM widths of all the ozone lines observed by SOFIA / GREAT are less than a few hundred megahertz, much narrower than the bandpass of the instruments (1 to 4 GHz depending on configuration). The atmospheric transmission across the whole bandpass may vary from a few percent to 80 or 90% when a strong ozone line is present. The frequency of the source spectra is sometimes on the line wing of ozone, where the atmospheric transmission is poor.

<sup>4</sup> Except for the few very low flights where the case degenerates to the same for ground based observations.

<sup>5</sup> A model with this second scaling factor is planned for future work.

<sup>6</sup> The ozone layer is lower at polar regions. However, SOFIA / GREAT have never observed at a latitude above 70°.

Even when the source lines are far away from strong ozone lines, an improperly modeled ozone line can be strong enough to affect the fitted pwv and the modeled water vapor absorption, which affects the calibration accuracy across the whole passband. Therefore, the knowledge of ozone mixing ratio at different altitudes is important for accurate atmospheric calibration.

Unlike water vapor whose spectra often appears as quasi-continuum, ozone are usually observed with complete line profiles because of their relatively narrow line widths compared with the bandwidth of the receiver. Therefore, it is possible to fit both the scaling and skew factors (see Section 2.4) of ozone distribution.

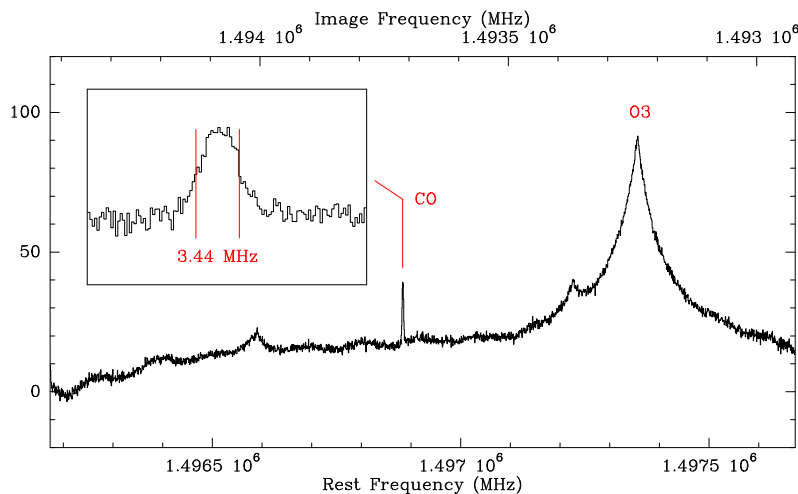


Figure 6.1: Atmospheric ozone and CO lines of an observation towards NGC 7023 using the GREAT L1 channel. The figure shows the spectra over the whole passband with signal (image) frequencies marked on the lower (upper) axes. The measured sky brightness at the edge of the passband may have large errors. The temperatures are in double-sideband scale with a sideband ratio of 1:1. Same below for observed atmospheric spectra.

The knowledge of an accurate stratospheric pressure-temperature profile is needed to fit the the vertical profile of ozone distribution from the observed line profiles. This is particularly important because the absorption of the solar emission by ozone has overwhelming influence over the stratospheric temperature. As shown in Figure 3 of Revathy et al. (2001), the temperatures of the low- and mid-stratosphere can be different by more than 40 K during early morning and late afternoon. The reference P-T profile from the CIRA used by *kalibrate* is a monthly average. It is probably not a good approximation of the actual P-T profile above the SOFIA aircraft, which usually flies in the early morning before sunrise. A strong ozone line, such as the one in Figure 6.1, might cause a calibration error of more than a few percent over the whole passband if its spectral power were significantly overestimated by using the reference P-T profile. Therefore, it is often necessary to fit the additional parameter added to the stratospheric temperature gradient (see Section 2.10) of the reference atmosphere. As saturated ozone lines are accurate probes to the stratospheric temperature, it is recommended to include them

in the observed passband during observation planning if, and only if ozone absorption is non-negligible for the given observation.

### *CO and other minor species*

The CO line absorption at the line centers are comparable to the collision induced absorption by molecular oxygen and nitrogen and the water vapor absorption in the atmospheric windows in typical GREAT observations, e.g., as shown in Figures 6.1. Since the FWHM of the CO lines are very narrow, they usually do not step into the frequency ranges of the source spectra. The total power of the collision induced emission by nitrogen and oxygen, and the emission of water vapor, ozone, and etc. across the passband is significantly higher than the spectral power of the CO lines. Therefore, the fitted parameters are virtually unaffected by the inaccuracy of CO vertical distribution in the static atmospheric model. We do not fit the vertical distribution of CO at present<sup>7</sup>, and only use the estimated values from Section 2.5.

The effects of other minor species, such as N<sub>2</sub>O and CH<sub>4</sub>, are negligible at the S/N ratio of typical GREAT observations. No effort was made for GREAT atmospheric calibration to model these species accurately.

### *Atomic oxygen*

The GREAT H channel is dedicated to [OI] observations. The current version of the AM atmospheric model (8.1) does not have [OI] lines included<sup>8</sup>. However, the atmospheric [OI] line at 4.74 THz only occupies about 3% of the receiver bandwidth and did not affect the calibration of the doppler-shifted source signals. Although *kalibrate* can properly calibrate current [OI] observations, modeling of the atmospheric [OI] lines still needs to be implemented in the future.

### *The P-T profile*

Because SOFIA flies around the tropopause, the part of the tropopause above the telescope is thin, and is expected to have only a small temperature gradient most of the time. There is usually no need to fit the tropospheric temperature gradient.

As explained above, an accurate P-T profile of the stratosphere is important for water vapor and ozone modeling. It is also important for modeling other components of the atmospheric absorption, such as the collision induced absorption, molecular and atomic oxygen lines. Observations by Revathy et al. (2001) have shown that the temperature gradient of the ozone layer can have a diurnal change

<sup>7</sup> Fitting the vertical profile of CO mixing ratio may need better S/N ratio than that in Figure 6.1. We leave this work to the future.

<sup>8</sup> After the submission of this thesis, [OI] lines have been included in AM version 9.0 mainly to facilitate GREAT calibration.

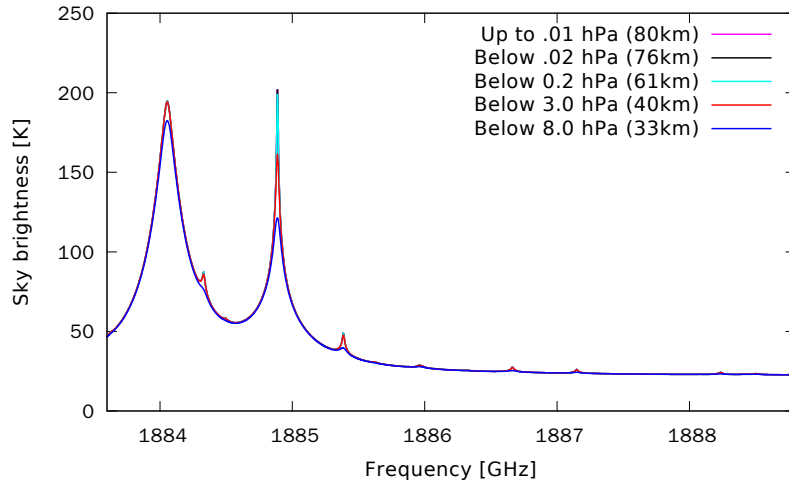


Figure 6.2: Modeled sky brightness with static atmospheric models from the SOFIA flight altitude up to different altitudes. The model parameters are based on the fit result of a real SKY scan (scan number 11722, taken on the 21st of January, 2015),

from 10 to over 30 K/km. However, the bottom altitude of the ozone layer is mostly controlled by the Brewer-Dobson circulation, which is a slow process. Therefore, the altitude of the tropopause temperature minimum stays more or less constant. For this reason, we rely on the reference atmosphere for an estimate of the tropopause altitude, and add an additional constant to the stratospheric P-T profile. This additional temperature gradient can be positive or negative, and can be obtained particularly from ozone observations because a saturated ozone line can be used to measure the temperature of the mid-stratosphere in conjunction with a strong water line as a secondary probe, as shown in Figure 6.2.

The mesospheric P-T profile mostly affects the CO lines. Because atmospheric CO is not properly modeled at present anyway, we also do not attempt to fit the mesospheric P-T profile.

### Summary

For SOFIA / GREAT observations, it is often necessary to fit many more parameters of the static atmospheric model than for NANTEN2 / SMART. The more important parameters are the scaling factor of water vapor distribution, the scaling and skew factors of ozone distribution, and the stratospheric temperature gradient (P-T profile). The P-T profile can be derived when fitting a saturated ozone or water line. For fitting the P-T profile, it will be beneficial to include a strong ozone or water line in the observed passband on either the image or the signal sideband, as long as the source signal remains in the range of low receiver temperature.

### 6.3 SOFIA/GREAT specific considerations for the radiative transfer model

#### Broadband collision induced absorption (CIA)

The broadband CIA from  $N_2$  and  $O_2$  is on the same order or even higher than water vapor absorption in the frequency range of GREAT, as shown in Figure 6.3.

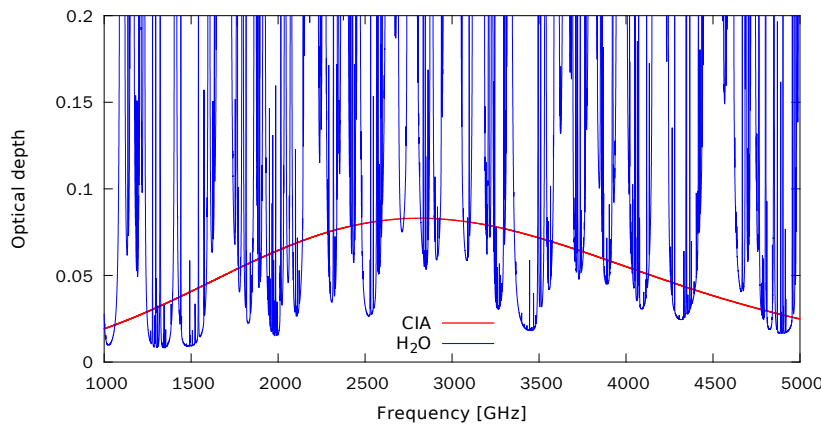


Figure 6.3: Water vapor absorption and broadband CIA from  $N_2$  and  $O_2$  in the GREAT L (1.2 to 1.9 THz), M (2.5 to 2.7 THz), and H (4.7 THz) bands in a typical SOFIA observation computed for an elevation of  $40^\circ$ .

The discrepancy of a few percent between lab measurements and the CIA computed with the AM model (Paine, 2014) is large enough to affect the modeled pwv. Whether the discrepancy comes from measurement errors or from the formulae in the AM model<sup>9</sup> can be distinguished by observations specifically targeted to atmospheric water vapor and P-T profile. These observations are analyzed in Section 6.4.

<sup>9</sup> For the formulae used by the AM model to compute CIA, see page 39 and references therein.

#### Computing time limitation of online calibration

Because the atmospheric CO lines are mainly thermally broadened, they are broader for GREAT observations than for NANTEN2 / SMART observations. The frequency resolution needed for the atmospheric model is therefore reduced. While the receiver bandwidths are not proportionally wider, less spectral channels are needed to model the atmospheric transmission. Online calibration of GREAT data using the AM model has been tested and is usable even without OpenCL acceleration.

## 6.4 Application of kalibrate to SOFIA/GREAT

### Receiver temperature stability: Test and effect

As explained in Section 5.5, the fluctuations of receiver noise temperature may result in very large errors in the measured sky brightness. The sky brightness in SOFIA / GREAT observations is typically only half of that for NANTEN2 / SMART. At the same time, the receiver temperature of GREAT is an order of magnitude higher than that of SMART. Therefore, the requirement of receiver temperature stability for GREAT is much higher. For example, a  $T_{rec}$  change of less than 0.5 ~ 1%, or about ten Kelvins in the L1 and L2 bands between HOT and SKY measurements leads to the same amount of error in  $T_{A,sky}$ . This is already marginal for accurate atmospheric calibration of the source signal, and can result in up to 100% error of the modeled pwv.

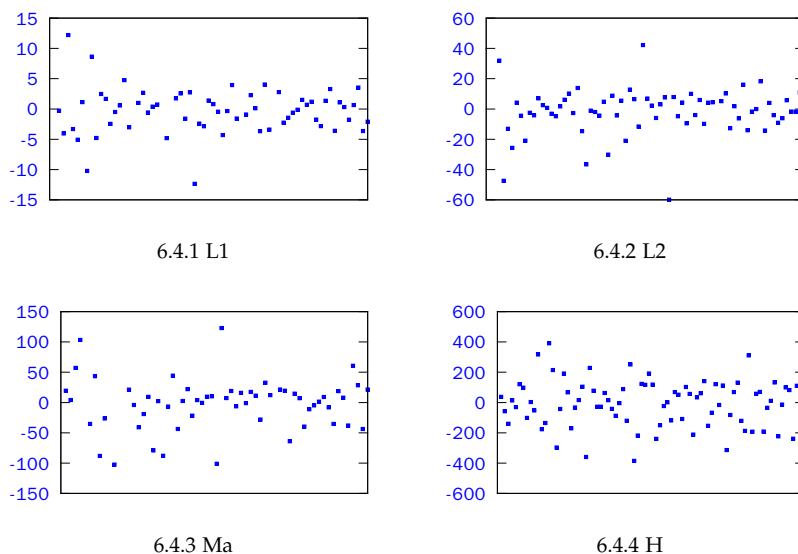


Figure 6.4: Receiver temperature stability check for GREAT (similar as Figure 5.8 on page 60, which is for SMART) showing the drift of  $T_{rec}$  in Kelvins across 100 seconds. Typical intervals between successive LOAD scans are about ten minutes. Additional figures to be found in Appendix B.

The actual drifts of  $T_{rec}$  in Figure 6.4 shows that calibration with the atmospheric transmission derived from OFF measurements is possible only for the L1 channel. Accurate atmospheric transmission can be calculated from OFF measurements of load switch observations (see Section 4.2) for both the L1 and L2 channels. The M and H channel data are not accurate enough to be used for atmospheric modeling.

### Gain stability: Test and effect

The hot-cold load temperature difference derived from "load calibration" (as explained in Section 5.5) and that from the temperature

sensors attached to the loads are not exactly the same due to receiver instability. Their discrepancies vary with receiver channels, as shown in Figure 6.5. The gain drifts of the L1, L2, Ma, and H channels are typically less than 0.5%, 1%, 5%, and 10%, respectively. The stability of the Ma and H channels need to be improved. The M and H channel data are not used for atmospheric modeling in the following analysis.

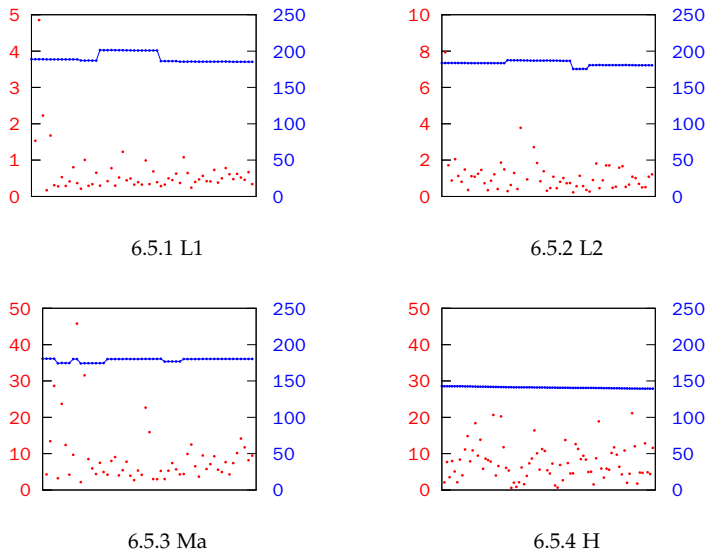


Figure 6.5: Result of load calibration (similar as Figure 5.6 on page 58) for the GREAT L1, L2, Ma, and H channels during one flight. Red dots: RMS error; Blue dotted lines: Temperature difference between hot and cold loads (jump indicates tuning to a different frequency). All numbers are in Kelvins. Additional figures to be found in Appendix B.

The amount of gain drift in the L-band receivers will give an error of a few percent in the sky brightness in typical observations where the LOAD is measured about every ten minutes. For the typical atmospheric transmission of 80%, this results in about 1% calibration error, which is usually not a problem. The error is even lower when the atmospheric transmission is calculated from SKY scans described in Section 4.2 because the measurement of  $T_{A,sky}$  is done less than half a minute after the HOT and COLD measurements. The discussions over the model parameters in the following sections of this chapter are based on the analysis of SKY scans with the GREAT L1 and L2 channels, and are therefore not affected by the instability of the receivers.

#### *Fitting GREAT data with the atmospheric model*

In Cycle I and Cycle II observations with GREAT, a number of SKY scans have been made to probe the properties of the part of the atmosphere above SOFIA, in particular the stratosphere.

Among the parameters of the static atmospheric model described in Chapter 2, the P-T profile is most important because its accuracy affects the absorption by all the species at all frequencies.

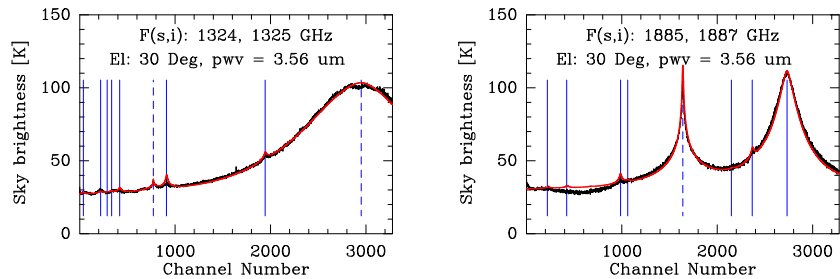


Figure 6.6: Observed (black) and fitted (red) atmospheric emission (in Kelvins) in scan 11722 of a GREAT observations on the 21st of January, 2015.

The L1 and L2 spectra are fitted simultaneously with the same model parameters. Dashed blue lines mark water lines, and solid blue lines mark ozone lines. Additional figures to be found in Appendix B. The date, time and geographical locations of these observations are recorded both in the raw data of spectrometer output as FITS (Wells et al., 1981) header variables, and in the reduced data shown in these figures as GILDAS/CLASS (Pety et al., 2015) header variables.

In the example shown in Figure 6.6, we have observed a saturated water line with the L1 channel and a saturated ozone line with the L2 channel to probe the temperatures of the low- to mid-stratosphere. A strong water line which probes the temperatures up to the stratopause is also observed with the L2 channel. Because of the different vertical distributions between water vapor and ozone, the saturated water and ozone lines have different peak brightnesses. The peaks are fitted consistently with the same stratospheric temperature gradient shown in Figure 6.7.

When fitting the observations in Figure 6.6, the water vapor scaling factor, ozone scaling and skew factors are also fitted. The water vapor scaling factor  $P_s$  mostly affects the slope of the wing of the saturated water line in the L1 channel and the peak brightness of the strong water line in the L2 channel. Both spectral features are fitted consistently with the same  $P_s$ .

Adjustment to the ozone scaling and skew factors mostly affect the wing shape of the saturated ozone line. The stratospheric temperature gradient, the scaling factor of water vapor distribution, the scaling and skew factors of ozone are fairly independent parameters in the static atmospheric model.

The fit result in Figure 6.7 indicates that SOFIA was flying below the tropopause, therefore  $P_s$  is a large positive value. The very high temperature maximum around 320 K, or 70 K higher than that in the reference atmosphere at 36.7°N, 120.6°W on 21st of January, 2015 is a result of the intense stratopause heating due to the descending stratopause in the winter hemisphere (von Zahn et al., 1998, and references therein).

Because the stratopause heating event lasts for only a few days, as is visible from Figure 1 of von Zahn et al. (1998), a SKY scan shown in Figure 6.8 that took place two days after the one in Figure 6.6 did not show such a hot stratopause with the fitted model parameters in Figure 6.9. The fitted water vapor scaling factor is a very small positive value, indicating that the telescope is very closely below the tropopause.

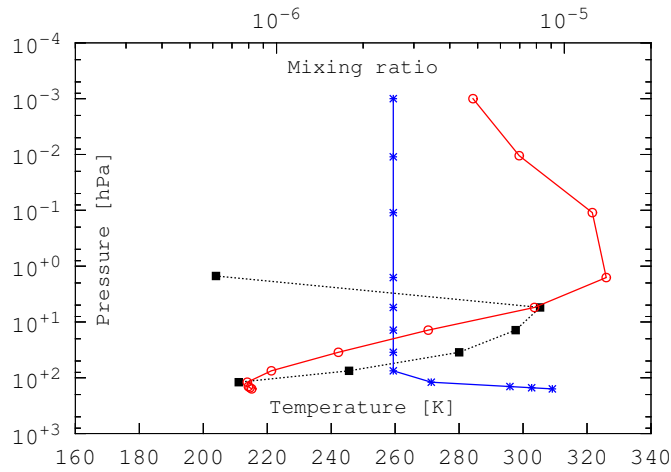


Figure 6.7: Fitted model parameters of the same observation as in Figure 6.6. Red line / circles: air temperature of each layer; Blue line / stars: water vapor mixing ratio; Black line / squares: ozone mixing ratio. The parameters, especially the P-T profile, above the stratopause may have very large errors. However, their effect on calibration is minimal due to the small air-mass above such an altitude. Additional figures to be found in Appendix B.

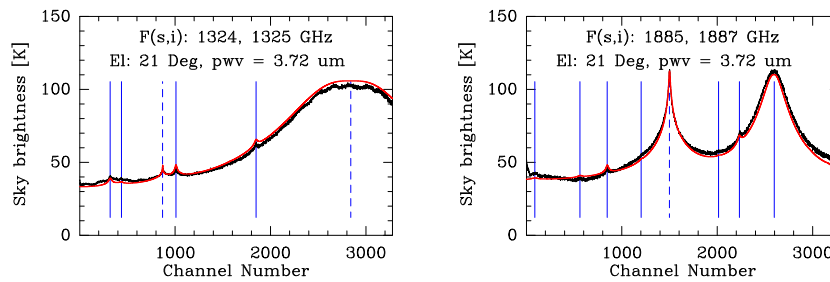


Figure 6.8: Same as Figure 6.6 but for an observed (black) and fitted (red) atmospheric emission in scan 11923 of a GREAT observation on 23rd of January, 2015.

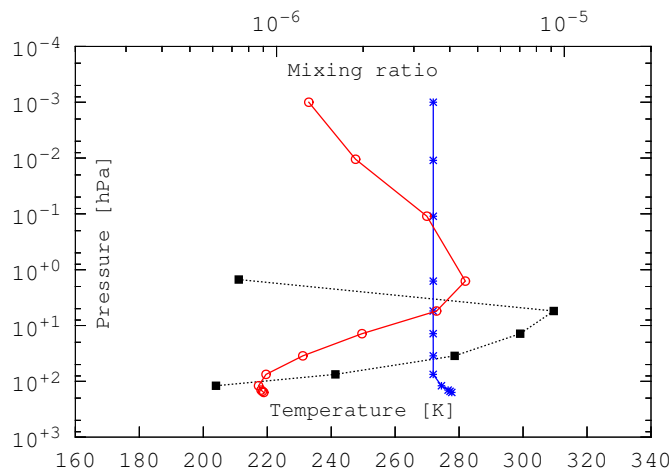


Figure 6.9: Same as Figure 6.7 but for the observation of scan 11923 shown in Figure 6.8.

An accurate stratospheric water vapor mixing ratio can be obtained more easily by observing above the tropopause. An observation on 13th of April, 2013 at 46.3°N, 112.5°W is such a case.

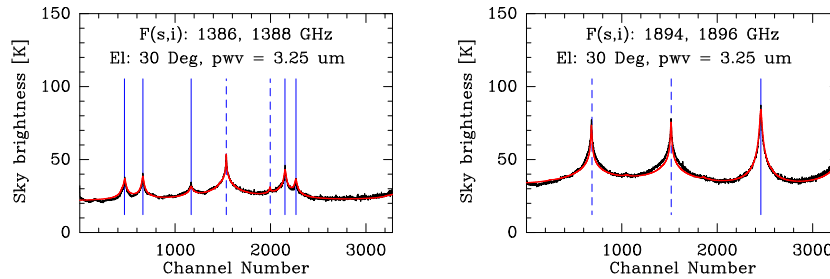


Figure 6.10: Same as Figure 6.6 but for an observed (black) and fitted (red) atmospheric emission in scan 7519 of a GREAT observations on 13th of April, 2013.

The fitted water vapor vertical distribution between 100 and 1 hPa shown in Figure 6.11 is consistent with HALOE observations on the order of magnitude (Harries et al., 1996). The fitted residue water vapor mixing ratio  $x_c$  is much higher than the default value of 2.5 ppm. This level of  $x_c$  is possible according to the observations by the Odin sub-mm radiometer (Orsolini et al., 2010).

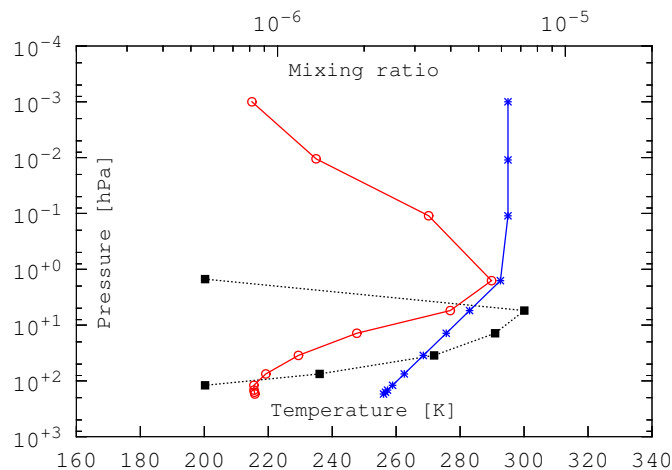
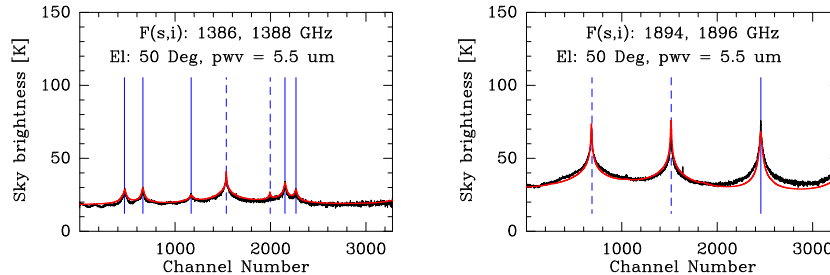


Figure 6.11: Same as Figure 6.7 but for the observation of scan 7519 shown in Figure 6.10.

The application of our atmospheric model and calibration procedure on the atmospheric observations using SKY scans with GREAT is successful in the sense that consistent sky brightnesses from the model and observation are obtained all telescope elevations from the same model parameters for both the L1 and L2 bands, and that the fitted parameters are reasonable according to dedicated meteorological observations.

### Consistency problems and analysis

Although the model fit of the atmospheric observations above usually works well, there are cases where a single set of model parameters do not give consistent fit between different frequency bands.



Take scan 7518 in Figure 6.12 for example: This scan was observed immediately before scan 7519, which is shown in Figures 6.10 and 6.11. They are close in both time and location. However, the fitted pwv from scan 7518 ( $5.5 \mu\text{m}$ ) is significantly higher than that from scan 7519 ( $3.25 \mu\text{m}$ ). A closer look shows that the fitted sky brightnesses in Figure 6.12 are inconsistent between the L1 and L2 bands. The modeled spectrum is stronger than the observed in the L1 band, and weaker than the observed in the L2 band across the whole pass-band.

By checking the gain stability of the receivers around the time of these scans, we can quickly tell from Figure 6.13 that the system gain jumped up and down around scan 7518. During the rapid boost, the system gain calculated from the HOT and COLD measurements of scan 7518 may have already changed by a non-negligible amount when the system switched the beams from the hot load to integrate on the sky signal.

Figure 6.12: Same as Figure 6.6 but for an observed (black) and fitted (red) atmospheric emission in scan 7518 of a GREAT observations on 13th of April, 2013. Unlike in Figure 6.10 where the fit was consistent for both the L1 and L2 bands, the modeled sky emission here is stronger than observed in the L1 band but weaker in the L2 band.

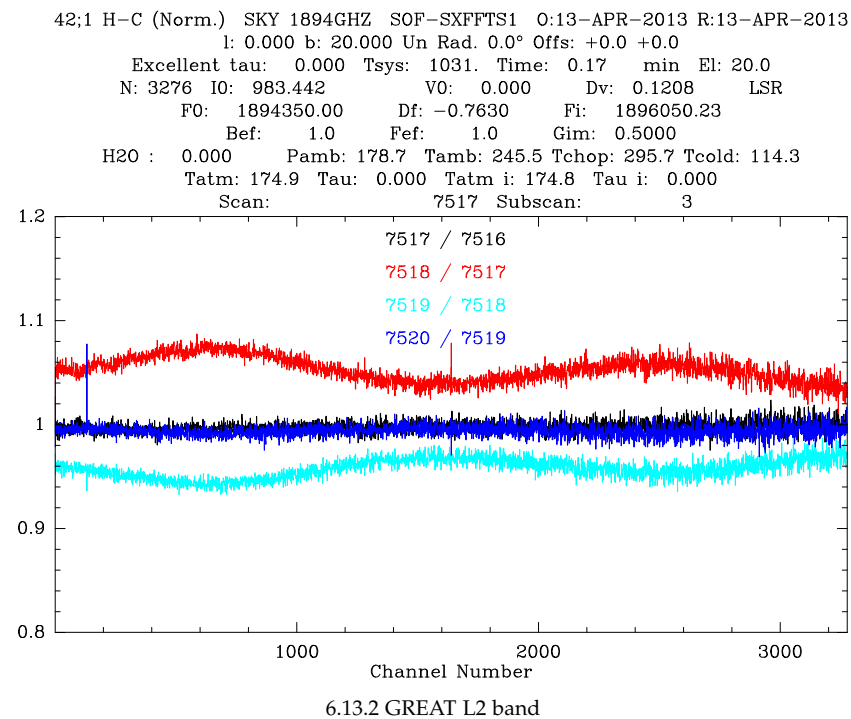
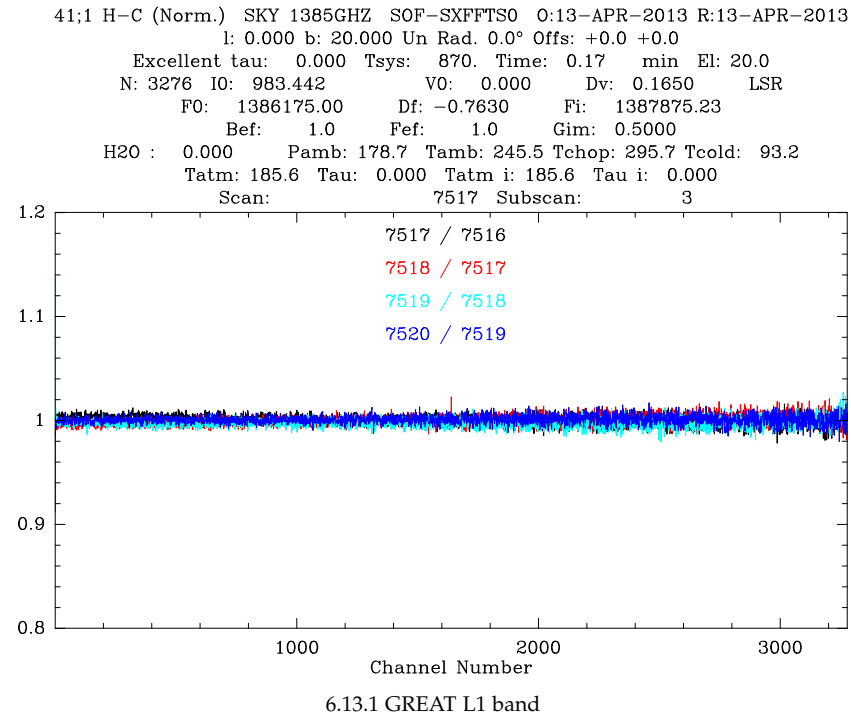


Figure 6.13: “Load calibration” (receiver stability check) for GREAT Cycle-I atmospheric observations (scans 7516 ~ 7520). The hot and cold load measurements are reduced using previous load scans. The difference between hot and cold load temperatures across the bandpass is divided by (normalized with) the expected difference derived from the temperature sensor’s read out. A relative error of about 5% is observed for scan 7518, while the system gain is stable from scan 7516 to 7517, and 7519 to 7520. Additional figures to be found in Appendix B.

This rapid fluctuation of the system gain can render SKY scans – the most reliable observing mode to derive atmospheric transmission – unreliable. Finding out the cause to such fluctuation is a problem for receiver experts.

Apart from the problems of the delicate receiver, the telescope servo which is built on mature technology can also fail. Both of the atmospheric spectra measured by the L1 and L2 channel receivers are incredibly higher than usual in scan 11719, shown in Figure 6.14.

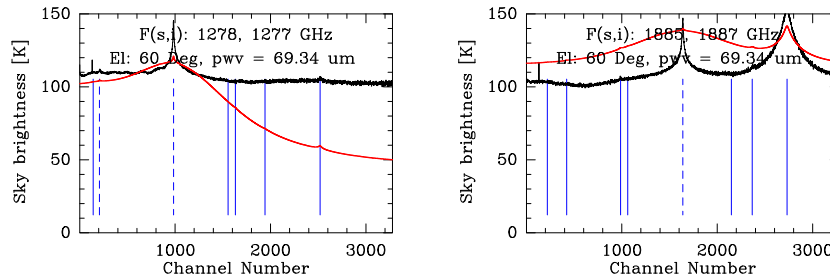


Figure 6.14: Same as Figure 6.6 but for an observed (black) and fitted (red) atmospheric emission in scan 11719 of a GREAT observations on the 21st of January, 2015.

A change of atmospheric emission cannot account for the extraordinarily high continuum level together with the strong and narrow water and ozone lines in Figure 6.14. It appears that the spectra in Figure 6.14 come from an incomplete switching of a mirror that caused the first  $\sim 30\%$  of the integration time of the SKY measurement, which was the last step of the COLD / HOT / SKY sequence in a SKY scan, was spent on the hot load whose temperature was 291.8 K. This kind of hardware malfunction should be investigated and corrected in order to reduce future problems.

For the SKY scans taken on the 21st of January, 2015, (scans 11711 to 11725) it is sometimes necessary to “correct” the values of the cold load temperature by a few Kelvins before gain calibration in order to get consistent fitting between the L1 and L2 band data with the atmospheric model. Once the cold load temperatures correction have been applied, the atmospheric model fits consistently between the two bands for a contiguous range of scans independent of telescope elevation and sky brightness. However, the amount of correction is non-repeatable for observations that are long time apart at the same LO frequency. The cause of this cold load temperature “error” may be a mechanical problem or something alike since the observations done two days later (scans 11916 to 11925) do not have this problem.

In addition to this rather random cold load temperature correction that needs to be applied to the whole bandpass, there is another kind of consistent calibration error that only appears in a narrower band. The observed atmospheric spectra have a dip of several Kelvins between 1.8853 and 1.8872 THz (left third of the bandpass in

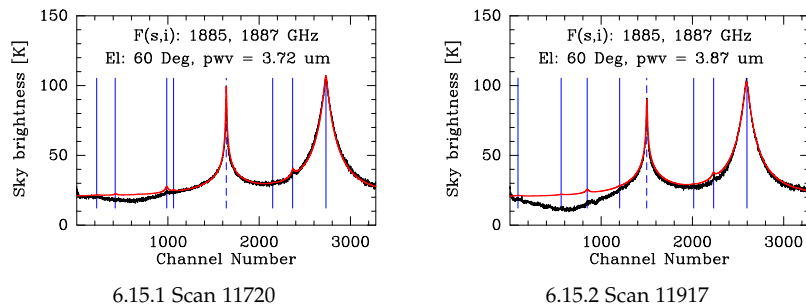


Figure 6.15: Same as Figure 6.6 but for atmospheric emission observed with the GREAT L2 channel receiver (black) and fitted with an atmospheric model (red) for scans 11720 and 11917.

Figure 6.15). This systematic error (dip) is always present in the SKY scans done on the 21st and 23rd of January, 2015. It may come from the error in the effective cold load temperature or other effects that can be determined with further test measurements.

## 6.5 Summary

The M and H channels of GREAT are not stable enough for atmospheric modeling. For the purpose of atmospheric calibration, the parameters of the atmospheric model must be derived from the L band data.

Even for the L1 and L2 channels, there are occasionally fast fluctuations of the system gain on a timescale of  $10^1$  seconds. This problem needs to be solved. Otherwise, even the most reliable observing mode to derived the sky transmission – the SKY scans – may result in large errors.

Using the static atmospheric model described in Chapter 2, the observed spectra of the atmospheric emission on the L1 and L2 bands of GREAT can be fitted consistently with the same set of parameters, including the total pwv, the water vapor scaling factor, the ozone scaling and skew factors, and the stratospheric temperature gradient. A depleted ozone layer that should give a spectrum of atmospheric emission like that in Figure 6.16 had not been observed.

The values of the effective cold load temperatures must be changed by a few Kelvins for some observation flights but not for others in order to get consistent model fittings in both of the L1 and L2 bands at all elevations.

The calibrated sky brightness is found to be consistently too low by up to  $\sim 10$  K from 1.8853 to 1.8872 THz. Whether this error comes from the calibration facility (e.g., window transmission curve that modulates the cold load emission) or something else should be investigated.

In order to achieve reliable, accurate atmospheric calibration at the lowest cost on observing time overhead with the currently sup-

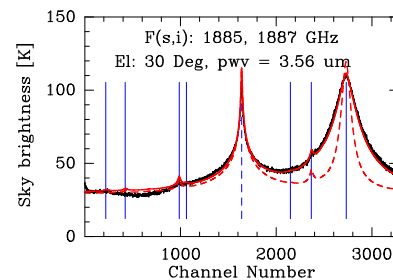


Figure 6.16: Same as Figure 6.6 but additionally shows the modeled emission with a depleted ozone layer (red dashed line). The hypothetical depleted ozone profile is based on the relative amount of decrease of Antarctic ozone in early spring of 2005 to 2013 shown by World Meteorological Organization (2014).

ported observing modes of SOFIA / GREAT, it is suggested that the atmospheric model always be fitted to the observed empty sky which is closest in time to the calibration scan. Alternatively, a measurement on the hot load can be inserted before or after the OFF-source measurement in order to mitigate the effect of receiver temperature change, though this would consume additional time and reduce the observing efficiency.



## 7

### *Summary and outlook*

Accurate calibration of sub-mm ground based and airborne astronomical observations relies on a stable receiver system with accurate parameters such as the effective cold load temperature, the correct choice of observing mode, and a proper static atmospheric model.

In order to achieve satisfactory accuracy of measured atmospheric emission which is used to derive the atmospheric transmission, the hot load measurement must be as close to the measurement of atmospheric emission as possible. This requires that the data used for atmosphere modeling must come from either SKY scans or load switch observations. Of these two approaches, deriving the atmospheric transmission from SKY scan is more time efficient, and has the additional advantage that the value of system gain used for calibrating the atmospheric emission is more precise because the SKY measurement is very close to the HOT and COLD measurements.

It is possible for a multi-pixel and / or multi-band receiver system that not all pixels are stable enough for use with atmospheric modeling. The pixels that are less stable can benefit from the modeling result from the data of the other pixels, and have better calibration accuracy than if calibrated independently. In the particular cases of SMART and GREAT, the 810 GHz SMART data should be calibrated using the atmospheric transmission derived from the 460 / 490 GHz data, and the M / H band data of GREAT should be calibrated using the atmospheric transmission derived from the L band data.

Using the static atmospheric model described in Chapter 2 with the AM radiative transfer model can fit the observed spectra with consistent model parameters for different frequency bands, pixels, and telescope elevations. However, the parameters of the static atmospheric model (except the pwv) must be fitted manually at present. Automatic fitting of the parameters requires additional work, e.g., automatic identification of the ozone lines used to probe the temperature of the mid-stratosphere.

Although little discrepancy is found between the fitted and ob-

served spectra of atmospheric emission, it would be beneficial to improve the model of ozone and water vapor vertical distribution. For ozone, a season and geographical location dependent model should be used. The prominent depletion of ozone at some locations should also be considered. For water vapor, a second scaling factor should be added in order to model both the tropospheric and stratospheric altitude dependency of mixing ratio.

The work of this thesis uses the atmospheric emission spectra computed with the AM atmospheric model. The speed of the original model code is marginally acceptable when running on a powerful<sup>1</sup> server computer. The same speed was achieved using OpenCL acceleration with a low power consumer grade graphics card. The OpenCL support of AM, which is part of this thesis, is rather preliminary, and can be optimized for a performance boost of another order of magnitude with a little effort (see Appendix D). This should be done as soon as possible to facilitate the analysis of the problems of the telescope and receiver system, further optimization of the static atmospheric model, and the migration of our routine calibration from the less accurate radiative transfer model using the atm-table.

<sup>1</sup> Measured by both price and electrical power consumption.

# *Acknowledgements*

First of all, I want to thank my principal advisor, Prof. Dr. Jürgen Stutzki, for his support and help from various aspects. He took time to read through many versions of this thesis draft, and gave valuable advices.

Our respectable colleague, Martin Miller, who is now working on the CCOSMA telescope (the relocated KOSMA telescope), introduced the KOSMA group to me ten years ago. I learnt many things from him about observing with radio telescopes. Our discussions, no matter on which topic, were always interesting.

Nicola Schneider read the complete draft of this thesis and gave comprehensive comments and suggestion.

Robert Simon gave valuable comments on the draft, and provided great linguistic assistance.

The detailed comments from Silke Andree-Labsch on a large part of the draft of this thesis are vitally important in that she not only gave suggestions but also pointed out critical errors.

Thanks LIU Xunchuan for detecting an inconsistency between Equation 2.1, which has been corrected now, and the actual formula used for calibration.

Thank Ronan Higgins and OKADA Yoko for comments and corrections.

The timely help from Urs U. Graf and Netty Honingh clarified matters about the receivers.

Particularly, this thesis could not have been finished without the help from Christof Buchbender and Frank Schlöder, who set up the necessary computing environment.

The support from our secretaries, Bettina Krause, Steffi Krämer, et al. are essential to this work.

This thesis work is carried out within the Collaborative Research Centre 956, sub-project A3, funded by the Deutsche Forschungsgemeinschaft (DFG).



# Appendices



# A

## *Additional figures for Chapter 5*

Appendix A contains figures that are similar to those shown in Chapter 5 but for all receiver pixels and additional observing days.

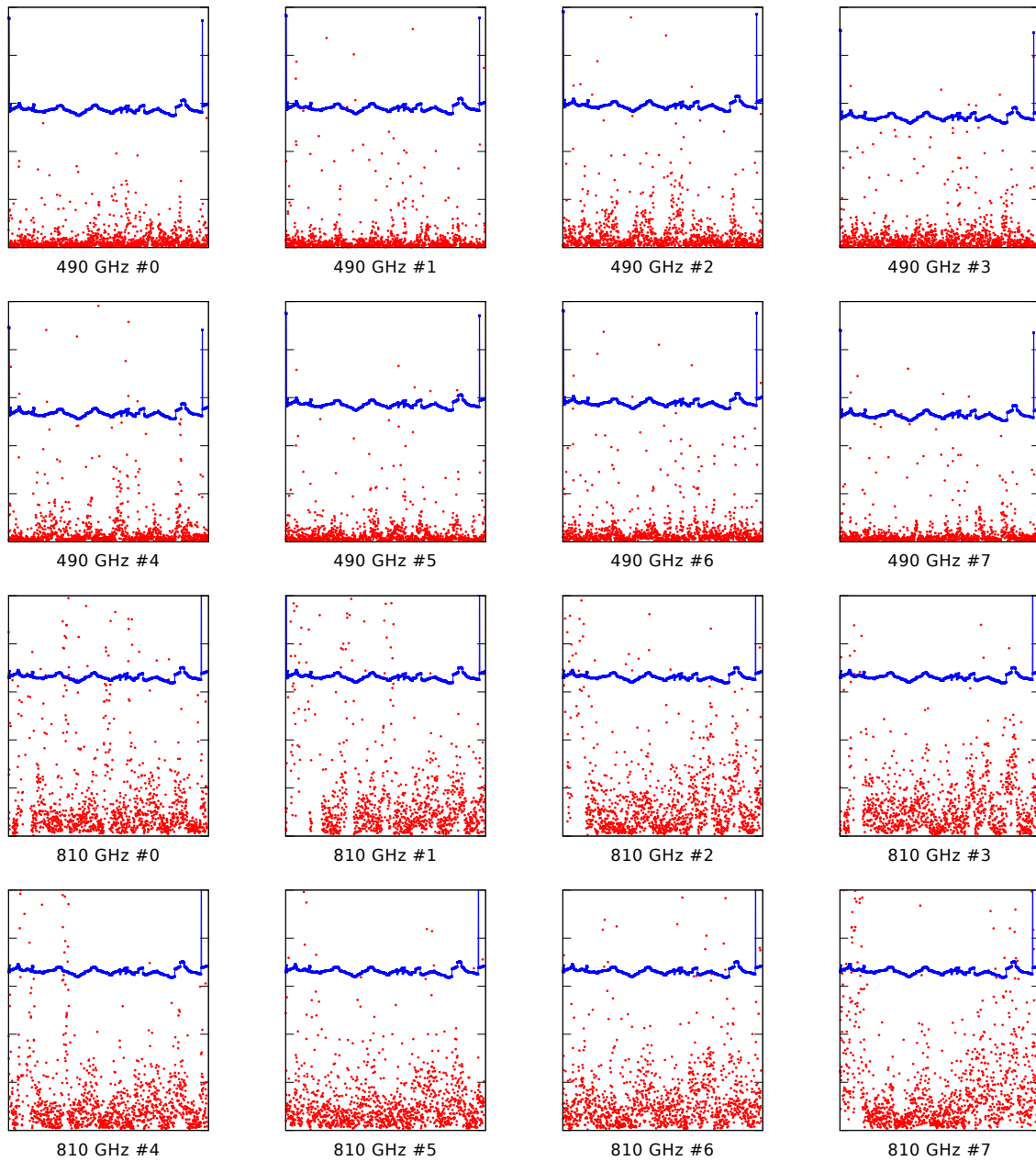


Figure A.1: Same as Figure 5.6 but for all pixels of SMART during the observing days from 2014-05-17 to 2014-06-17. The legends and axes limits are the same as in Figure 5.6.

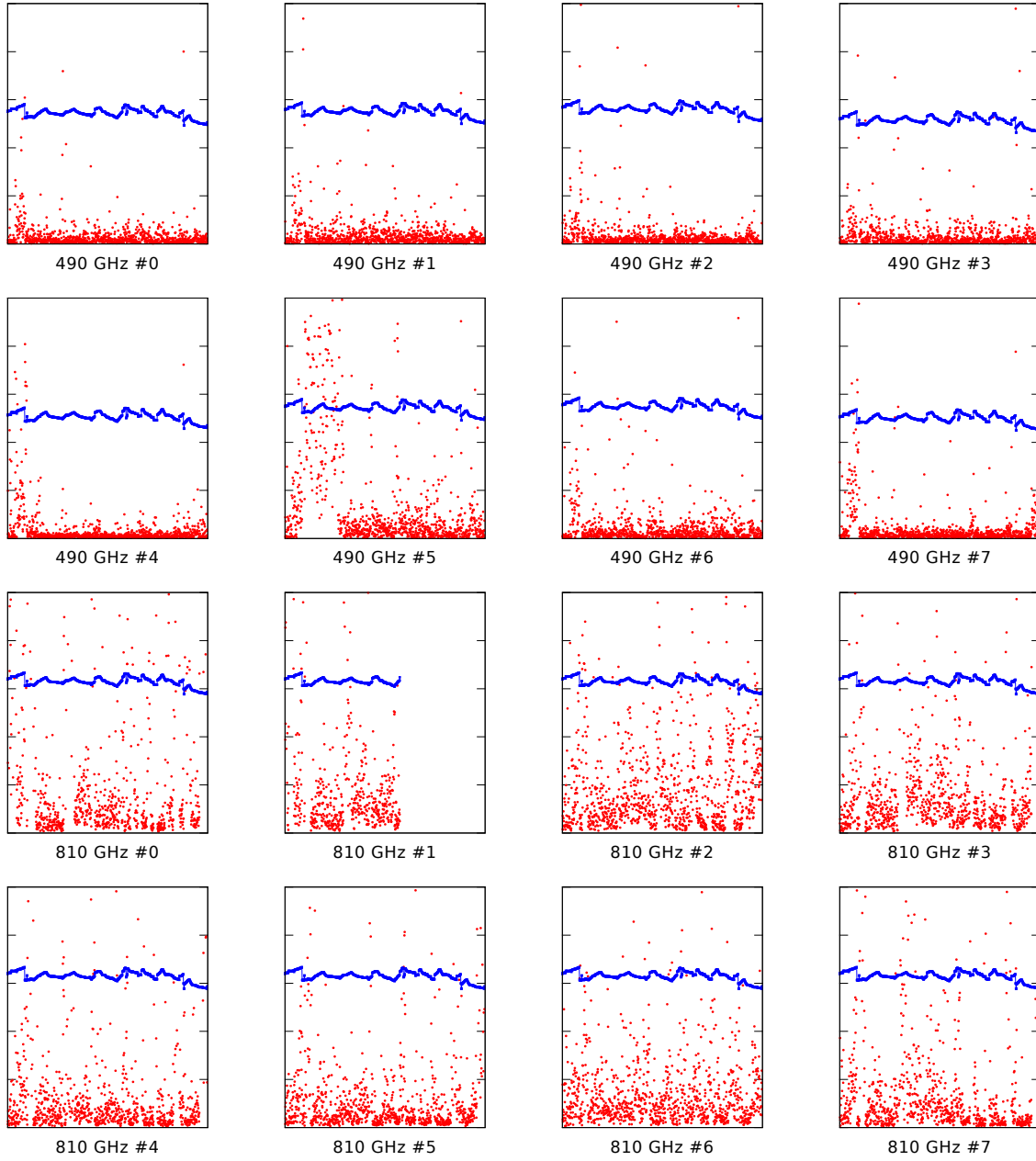


Figure A.1: Continued, for the observing days from 2014-06-22 to 2014-07-25.

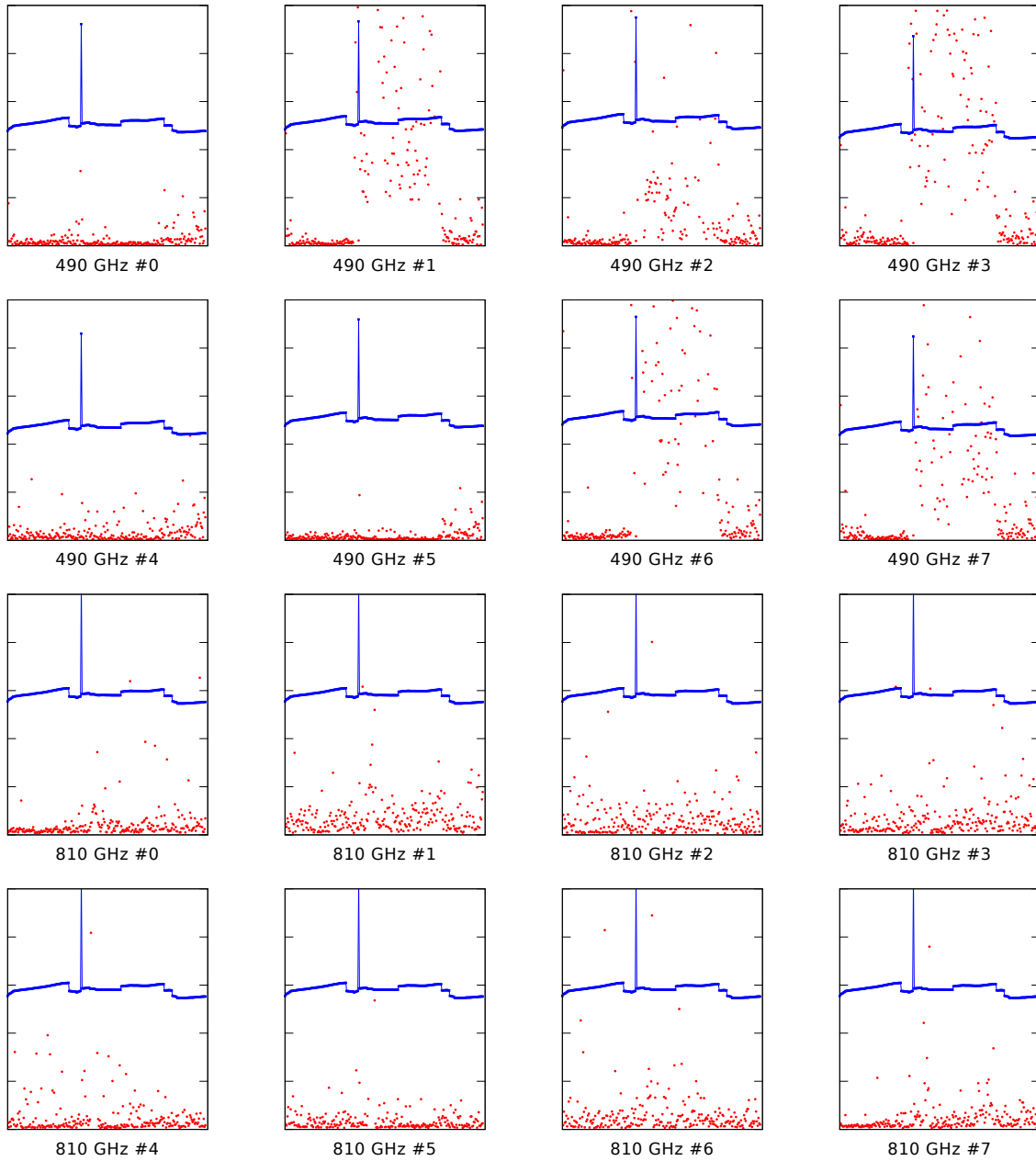


Figure A.1: Continued, for the observing days from 2014-09-21 to 2014-10-09.

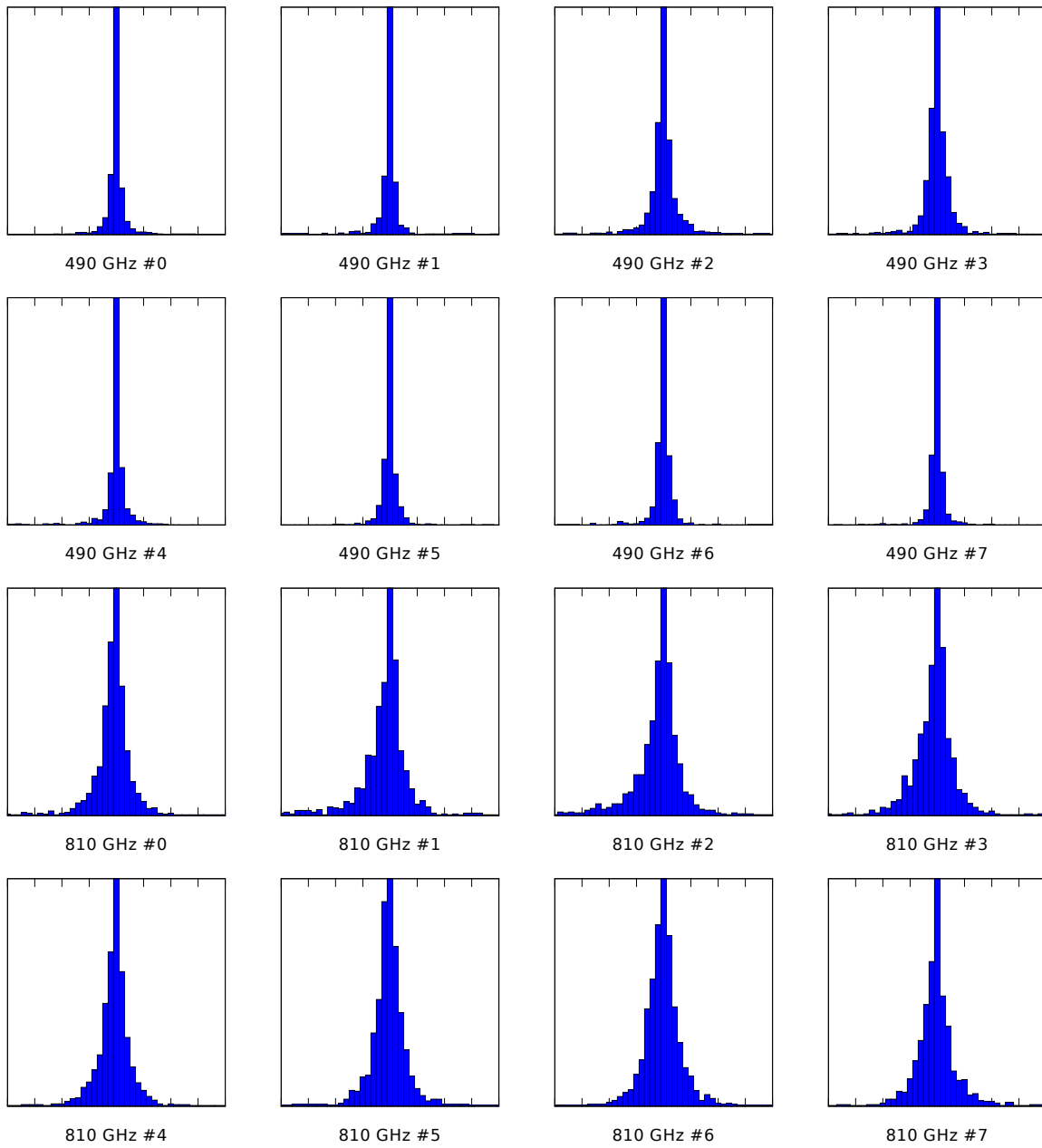


Figure A.2: Same as Figure 5.7 but for all pixels of SMART during the observing days from 2014-05-17 to 2014-06-17. The axes limits are the same as in Figure 5.7.

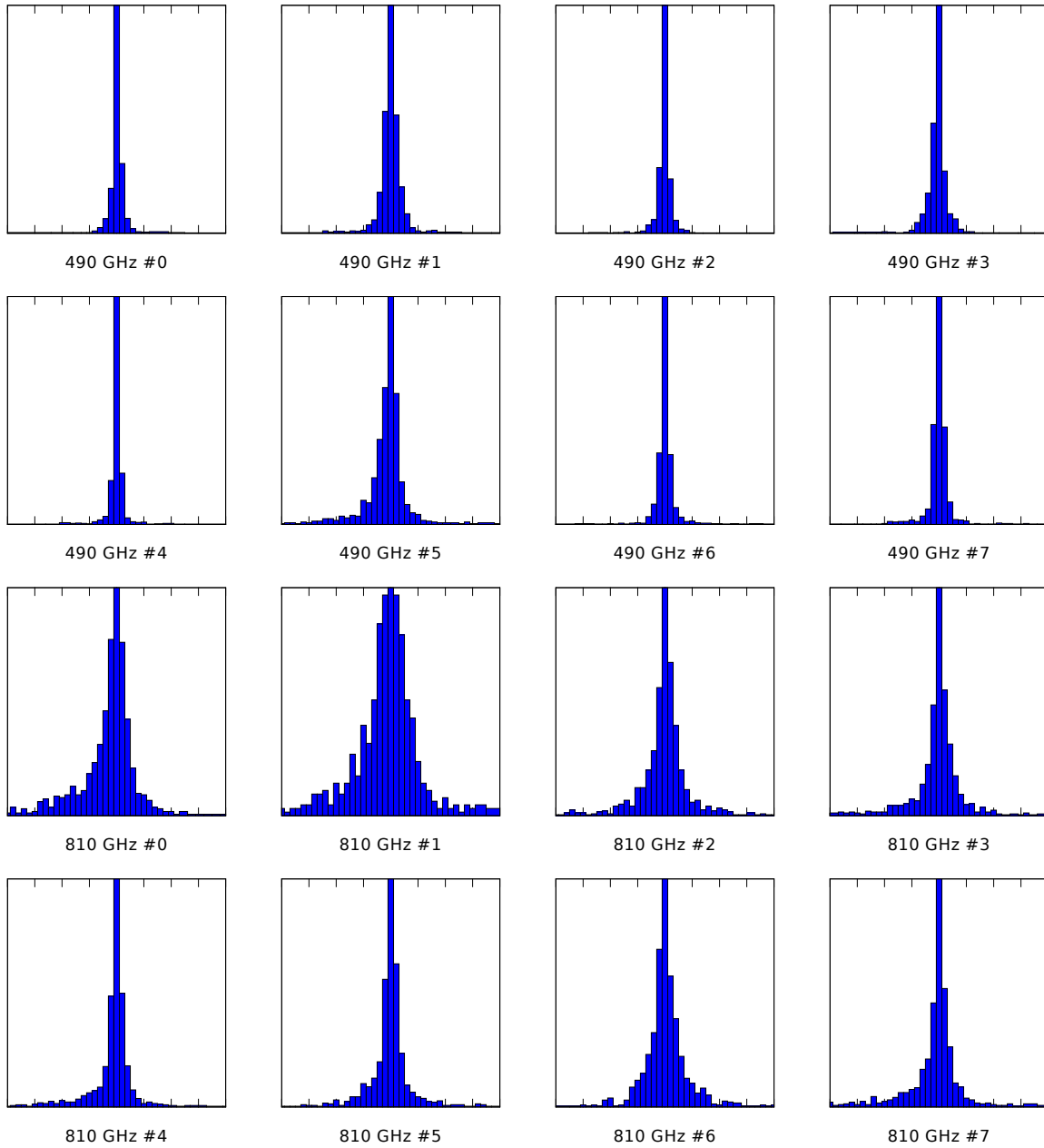


Figure A.2: Continued, for the observing days from 2014-06-22 to 2014-07-25.

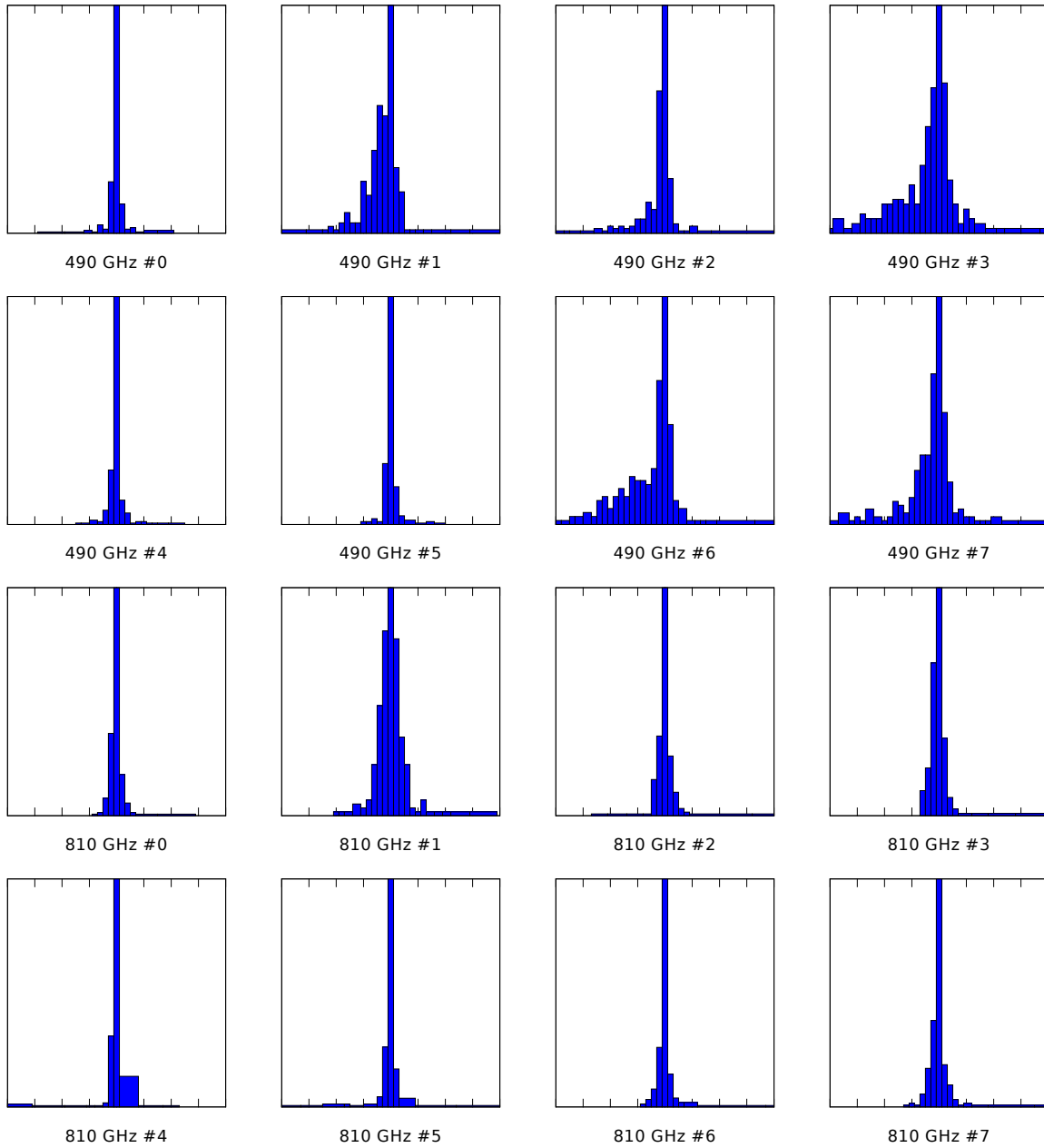


Figure A.2: Continued, for the observing days from 2014-09-21 to 2014-10-09.

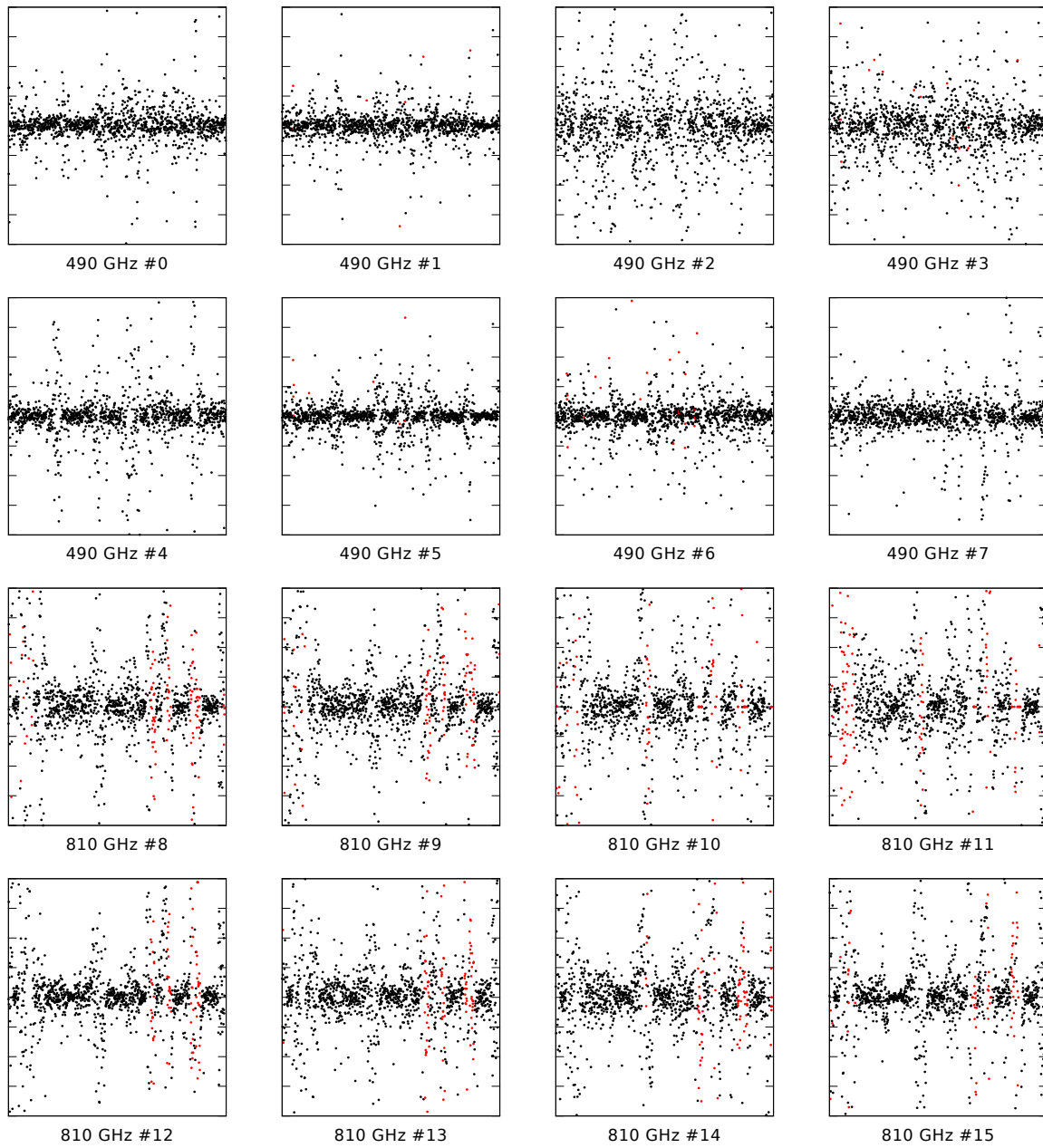


Figure A.3: Same as Figure 5.8 but for all pixels of SMART during the observing days from 2014-05-17 to 2014-06-17. The legends and axes limits are the same as in Figure 5.8.

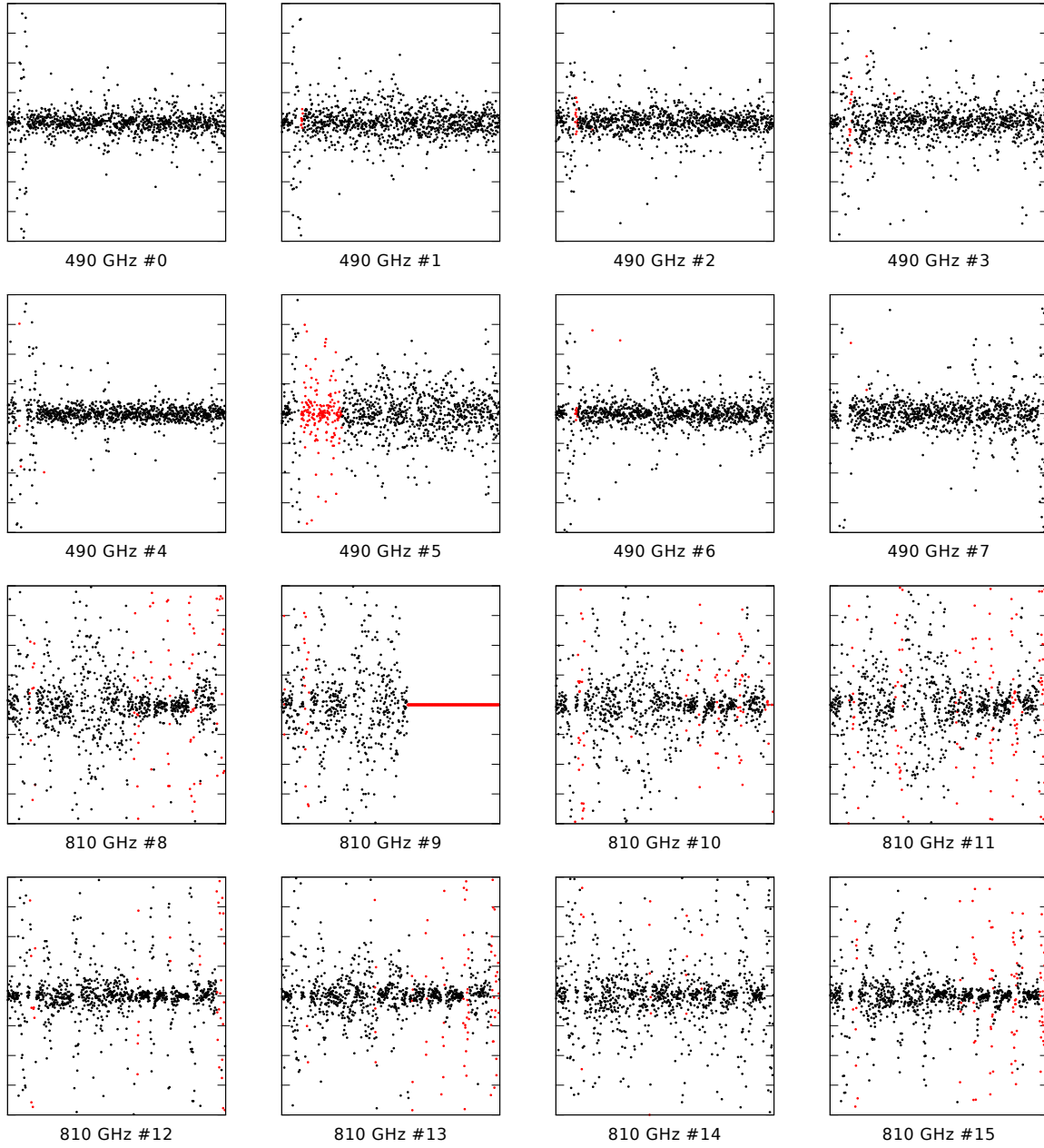


Figure A.3: Continued, for the observing days from 2014-06-22 to 2014-07-25.

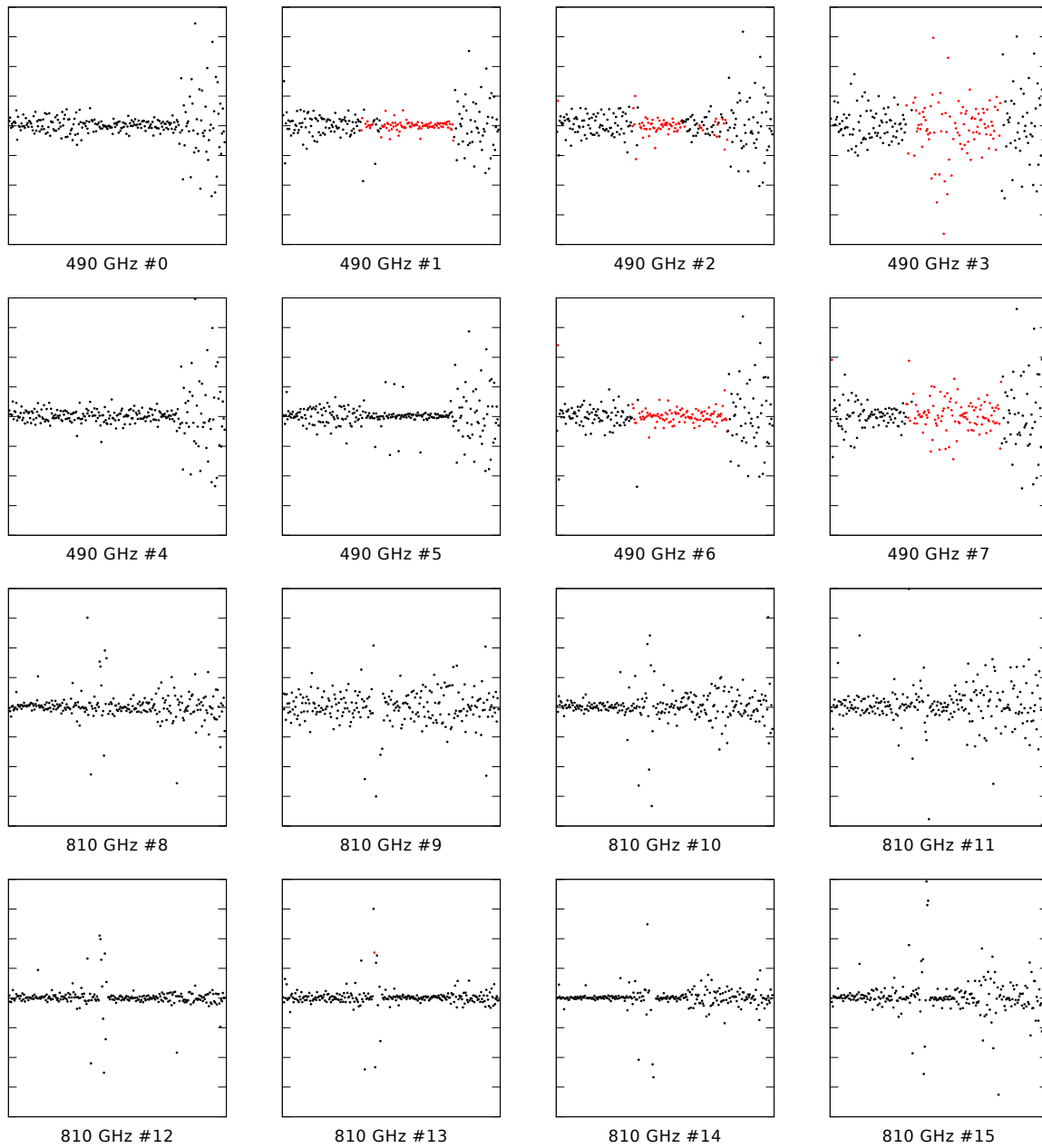


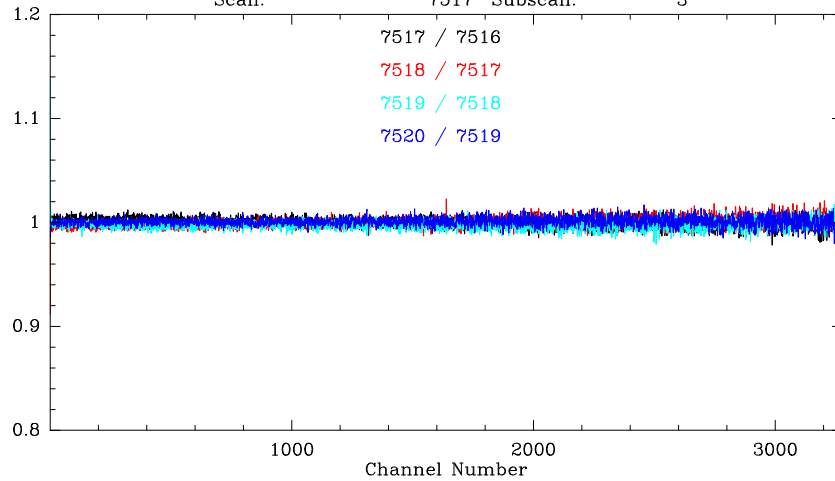
Figure A.3: Continued, for the observing days from 2014-09-21 to 2014-10-09.

## *B*

### *Additional figures for Chapter 6*

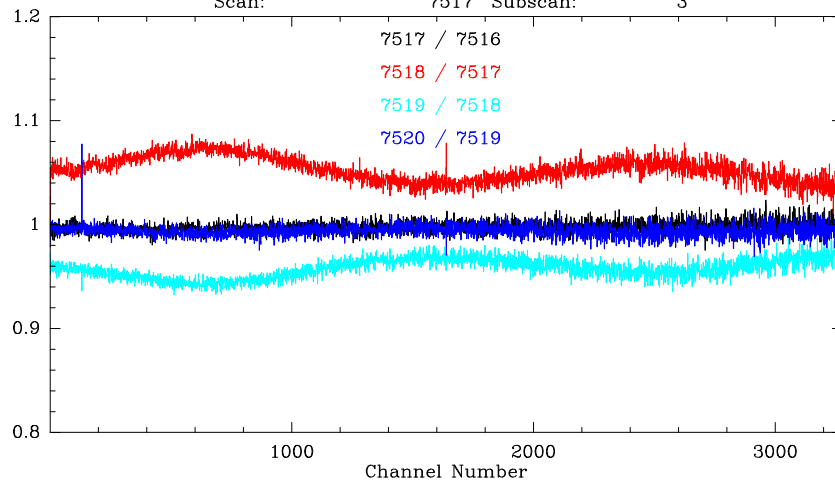
Appendix B contains figures that are similar to those shown in Chapter 6 but for more observations. The date, time and geographical locations of these observations are recorded both in the raw data of spectrometer output as FITS (Wells et al., 1981) header variables, and in the reduced data shown in these figures as GILDAS/CLASS (Pety et al., 2015) header variables.

41;1 H-C (Norm.) SKY 1385GHZ SOF-SXFFTS0 0:13-APR-2013 R:13-APR-2013  
 l: 0.000 b: 20.000 Un Rad. 0.0° Offs: +0.0 +0.0  
 Excellent tau: 0.000 Tsys: 870. Time: 0.17 min El: 20.0  
 N: 3276 IO: 983.442 VO: 0.000 Dv: 0.1650 LSR  
 F0: 1386175.00 Df: -0.7630 Fi: 1387875.23  
 Bef: 1.0 Fef: 1.0 Gim: 0.5000  
 H2O : 0.000 Pamb: 178.7 Tamb: 245.5 Tchop: 295.7 Teold: 93.2  
 Tatm: 185.6 Tau: 0.000 Tatm i: 185.6 Tau i: 0.000  
 Scan: 7517 Subscan: 3



B.1.1 GREAT L1 band

42;1 H-C (Norm.) SKY 1894GHZ SOF-SXFFTS1 0:13-APR-2013 R:13-APR-2013  
 l: 0.000 b: 20.000 Un Rad. 0.0° Offs: +0.0 +0.0  
 Excellent tau: 0.000 Tsys: 1031. Time: 0.17 min El: 20.0  
 N: 3276 IO: 983.442 VO: 0.000 Dv: 0.1208 LSR  
 F0: 1894350.00 Df: -0.7630 Fi: 1896050.23  
 Bef: 1.0 Fef: 1.0 Gim: 0.5000  
 H2O : 0.000 Pamb: 178.7 Tamb: 245.5 Tchop: 295.7 Teold: 114.3  
 Tatm: 174.9 Tau: 0.000 Tatm i: 174.8 Tau i: 0.000  
 Scan: 7517 Subscan: 3

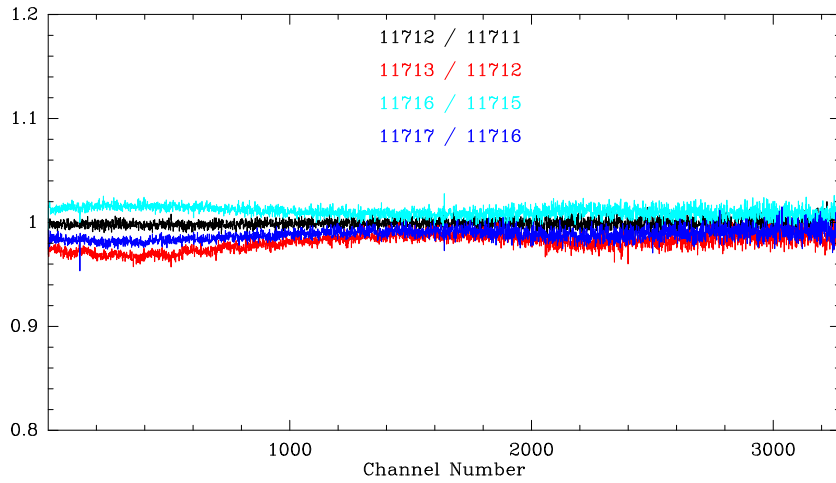


B.1.2 GREAT L2 band

Figure B.1: This is basically a repeat of Figure 6.13 (for GREAT Cycle-I Leg-2 atmospheric observations), just for the completeness of the figures in this chapter.

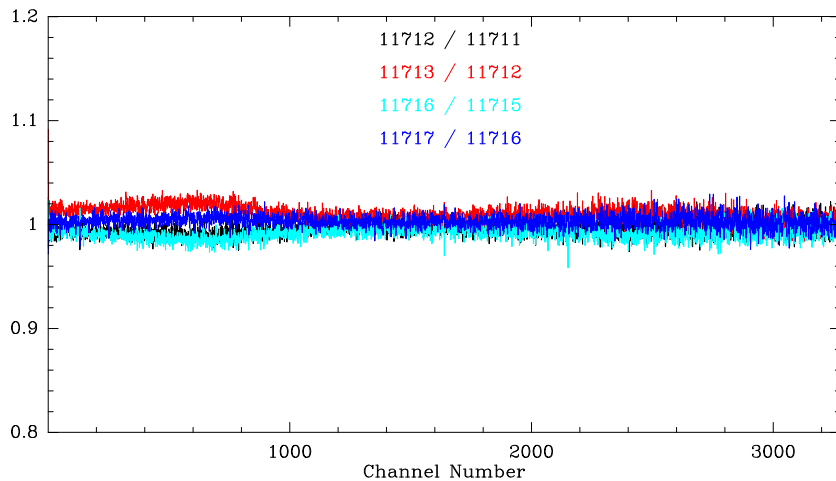
242;1 H-C (Norm.) Goeran 1 SOF-SXFPTS0 0:21-JAN-2015 R:21-JAN-2015  
 l: 0.000 b: 19.471 Un Rad. 0.0° Offs: +0.0 +0.0  
 Excellent tau: 0.000 Tsys: 938. Time: 0.17 min El: 19.5  
 N: 3276 IO: 983.442 VO: 0.000 Dv: -0.1790 LSR  
 F0: 1278266.00 Df: 0.7630 Fi: 1276565.91

Figure B.2: Same as Figure B.1 but for GREAT Cycle-II Leg-9 atmospheric observations.



B.2.1 GREAT L1 band

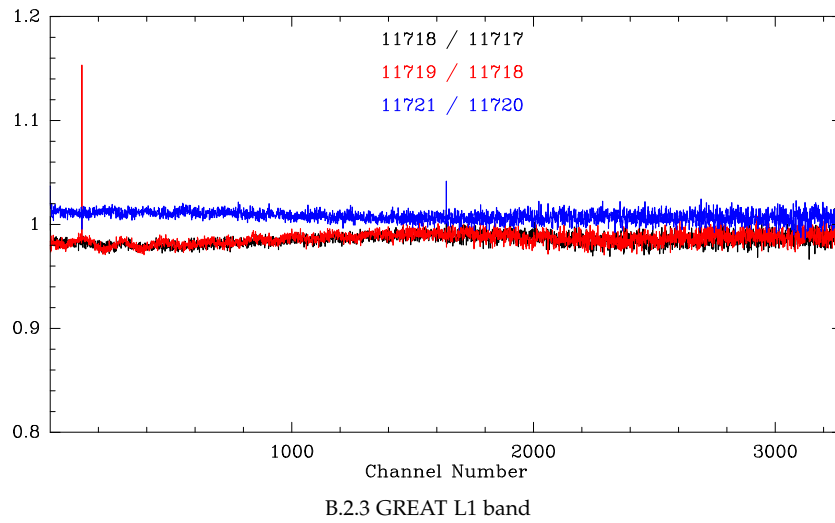
243;1 H-C (Norm.) Goeran 3 SOF-SXFPTS1 0:21-JAN-2015 R:21-JAN-2015  
 l: 0.000 b: 19.471 Un Rad. 0.0° Offs: +0.0 +0.0  
 Excellent tau: 0.000 Tsys: 1113. Time: 0.17 min El: 19.5  
 N: 3276 IO: 983.442 VO: 0.000 Dv: 0.1213 LSR  
 F0: 1885388.00 Df: -0.7630 Fi: 1887088.09



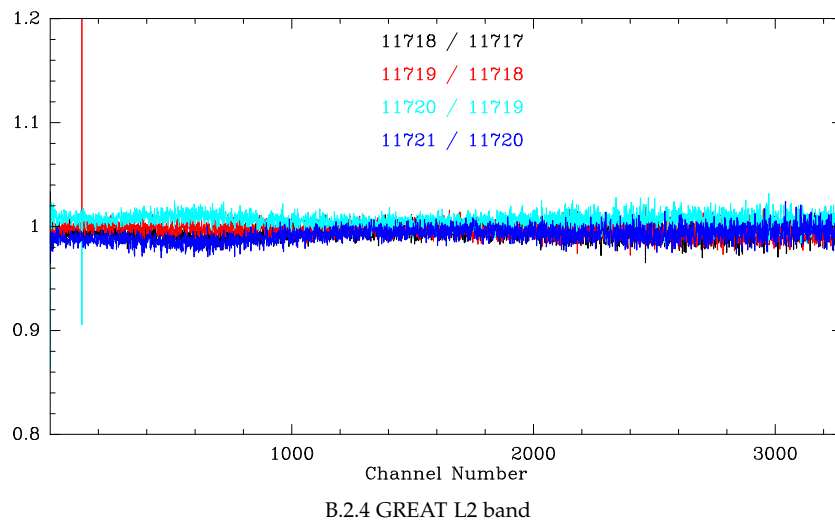
B.2.2 GREAT L2 band

262;1 H-C (Norm.) Goeran 1 SOF-SXFPTS0 0:21-JAN-2015 R:21-JAN-2015  
 l: 0.000 b: 41.810 Un Rad. 0.0° Offs: +0.0 +0.0  
 Excellent tau: 0.000 Tsys: 902. Time: 0.17 min El: 41.8  
 N: 3276 IO: 983.442 VO: 0.000 Dv: -0.1789 LSR  
 F0: 1278266.00 Df: 0.7630 Fi: 1276566.00

Figure B.2: Continued.

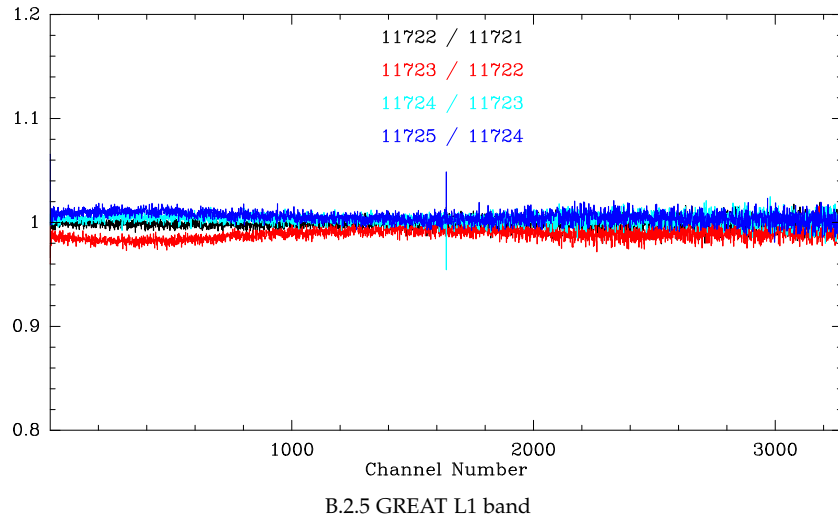


263;1 H-C (Norm.) Goeran 3 SOF-SXFPTS1 0:21-JAN-2015 R:21-JAN-2015  
 l: 0.000 b: 41.810 Un Rad. 0.0° Offs: +0.0 +0.0  
 Excellent tau: 0.000 Tsys: 1117. Time: 0.17 min El: 41.8  
 N: 3276 IO: 983.442 VO: 0.000 Dv: 0.1213 LSR  
 F0: 1885388.00 Df: -0.7630 Fi: 1887088.00

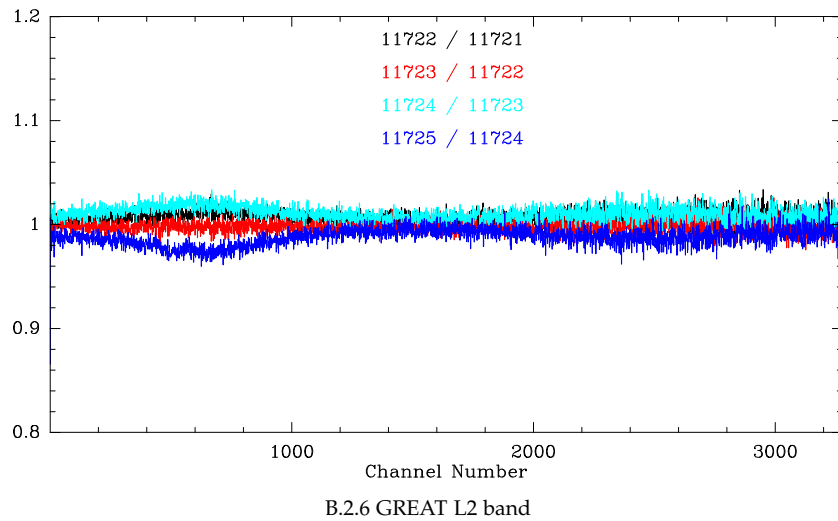


277;1 H-C (Norm.) Goeran 2 SOF-SXFFTS0 0:21-JAN-2015 R:21-JAN-2015  
 l: 0.000 b: 30.000 Un Rad. 0.0° Offs: +0.0 +0.0  
 Excellent tau: 0.000 Tsys: 972. Time: 0.17 min El: 30.0  
 N: 3276 IO: 983.442 VO: 0.000 Dv: 0.1728 LSR  
 F0: 1323565.00 Df: -0.7630 Fi: 1325265.00

Figure B.2: Continued.

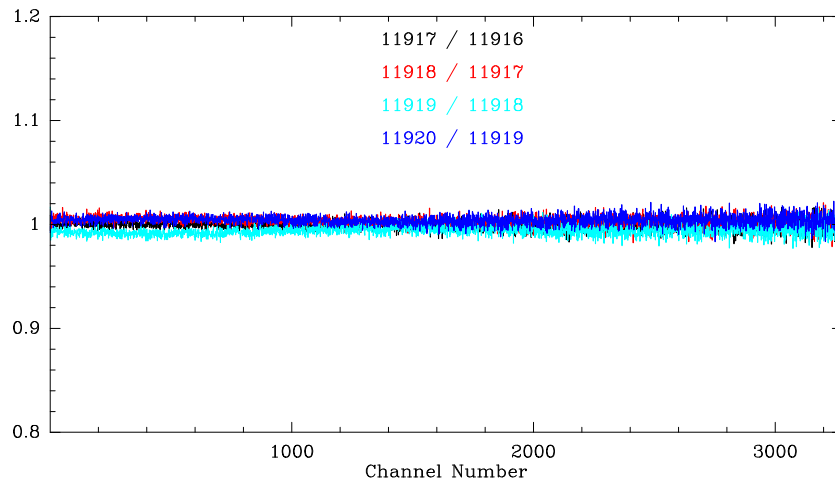


278;1 H-C (Norm.) Goeran 3 SOF-SXFFTS1 0:21-JAN-2015 R:21-JAN-2015  
 l: 0.000 b: 30.000 Un Rad. 0.0° Offs: +0.0 +0.0  
 Excellent tau: 0.000 Tsys: 1132. Time: 0.17 min El: 30.0  
 N: 3276 IO: 983.442 VO: 0.000 Dv: 0.1213 LSR  
 F0: 1885388.00 Df: -0.7630 Fi: 1887088.00



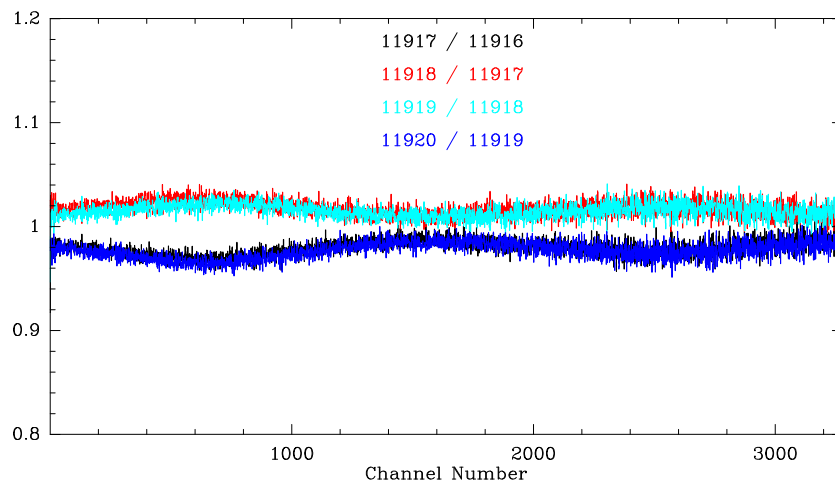
204;1 H-C (Norm.) Goeran 2 SOF-SXFPTS0 0:23-JAN-2015 R:23-JAN-2015  
 l: 0.000 b: 60.408 Un Rad. 0.0° Offs: +0.0 +0.0  
 Excellent tau: 0.000 Tsys: 923. Time: 0.17 min El: 60.5  
 N: 3276 IO: 983.442 VO: 0.000 Dv: 0.1728 LSR  
 F0: 1323565.00 Df: -0.7630 Fi: 1325265.10

Figure B.3: Same as Figure B.1 but for GREAT Cycle-II Leg-11 atmospheric observations.



B.3.1 GREAT L1 band

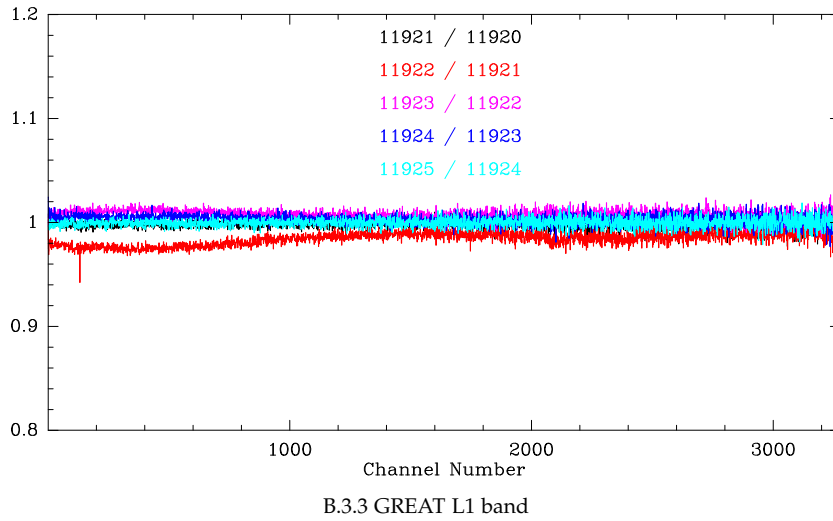
205;1 H-C (Norm.) Goeran 3 SOF-SXFPTS1 0:23-JAN-2015 R:23-JAN-2015  
 l: 0.000 b: 60.408 Un Rad. 0.0° Offs: +0.0 +0.0  
 Excellent tau: 0.000 Tsys: 1126. Time: 0.17 min El: 60.5  
 N: 3276 IO: 983.442 VO: 0.000 Dv: 0.1213 LSR  
 F0: 1885388.00 Df: -0.7630 Fi: 1887088.10



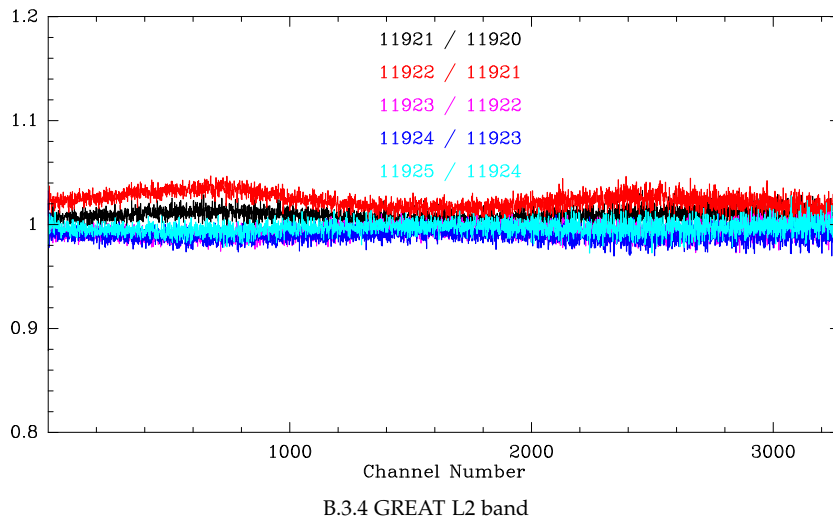
B.3.2 GREAT L2 band

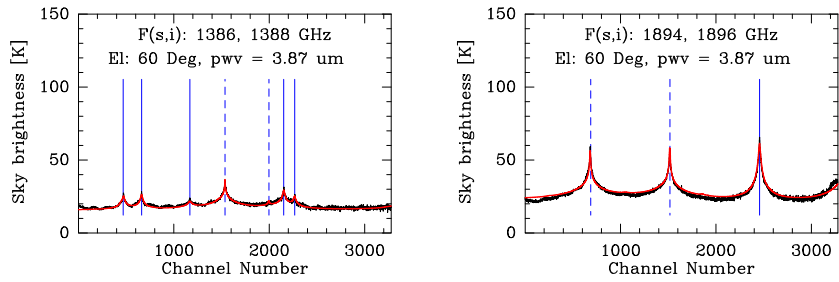
220;1 H-C (Norm.) Goeran 2 SOF-SXFFTS0 0:23-JAN-2015 R:23-JAN-2015  
 l: 0.000 b: 21.324 Un Rad. 0.0° Offs: +0.0 +0.0  
 Excellent tau: 0.000 Tsys: 926. Time: 0.17 min El: 21.4  
 N: 3276 IO: 983.442 VO: 0.000 Dv: 0.1728 LSR  
 F0: 1323565.00 Df: -0.7630 Fi: 1325265.10

Figure B.3: Continued.

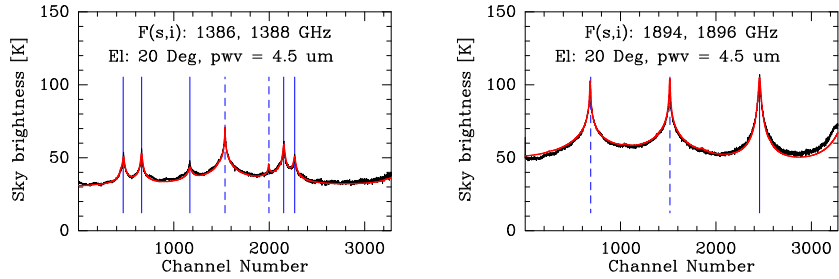


221;1 H-C (Norm.) Goeran 3 SOF-SXFFTS1 0:23-JAN-2015 R:23-JAN-2015  
 l: 0.000 b: 21.324 Un Rad. 0.0° Offs: +0.0 +0.0  
 Excellent tau: 0.000 Tsys: 1142. Time: 0.17 min El: 21.4  
 N: 3276 IO: 983.442 VO: 0.000 Dv: 0.1213 LSR  
 F0: 1885388.00 Df: -0.7630 Fi: 1887088.10

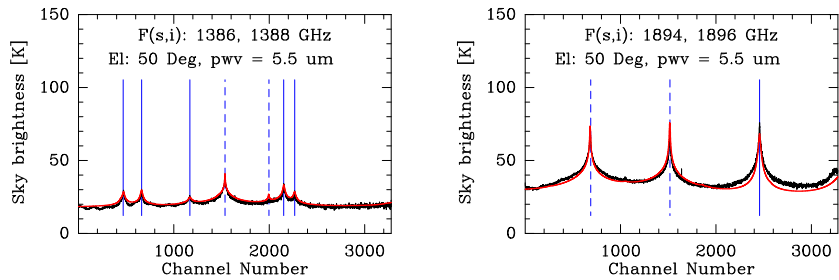




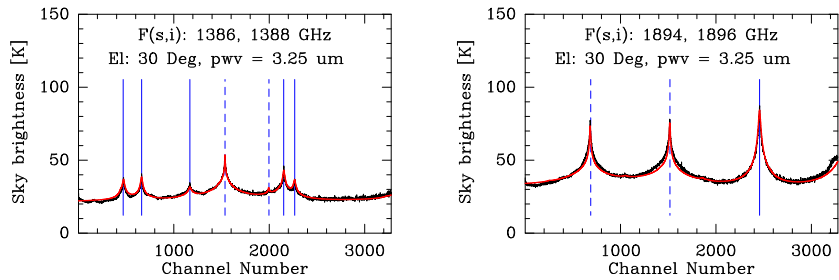
B.4.1 Scan 7516



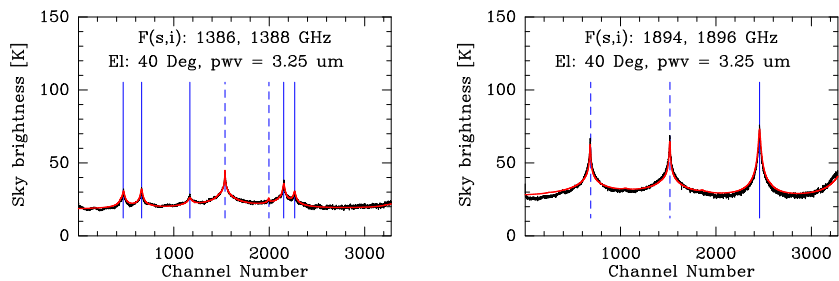
B.4.2 Scan 7517



B.4.3 Scan 7518

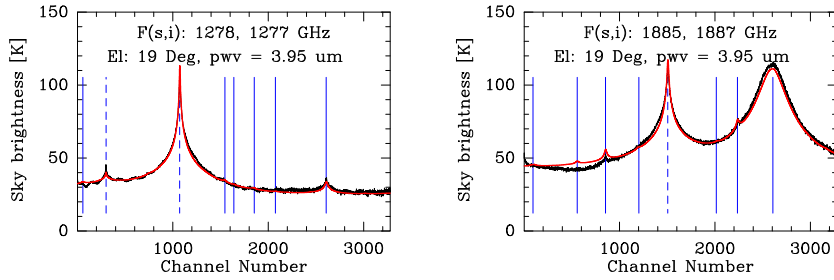


B.3.4 Scan 7519

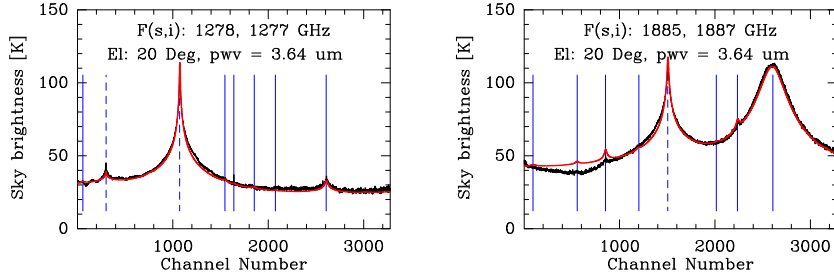


B.3.5 Scan 7520

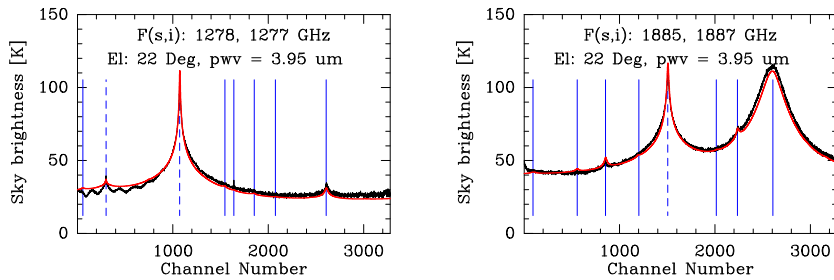
Figure B.4: Same as Figure 6.6 but for GREAT Cycle-I Leg-2 atmospheric observations.



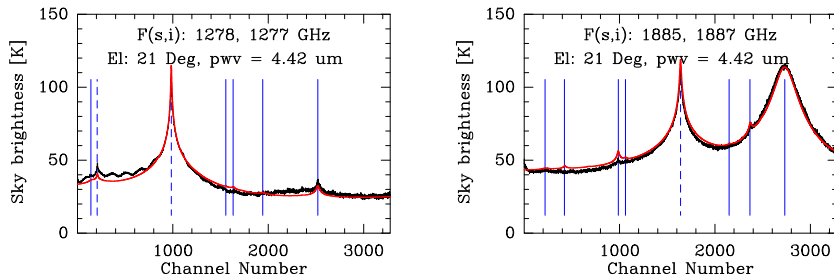
B.5.1 Scan 11711



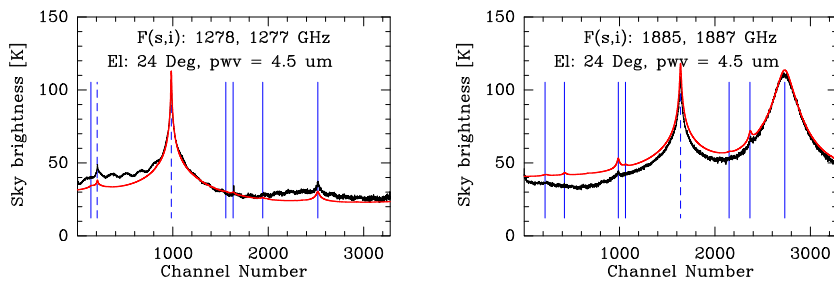
B.5.2 Scan 11712



B.5.3 Scan 11713

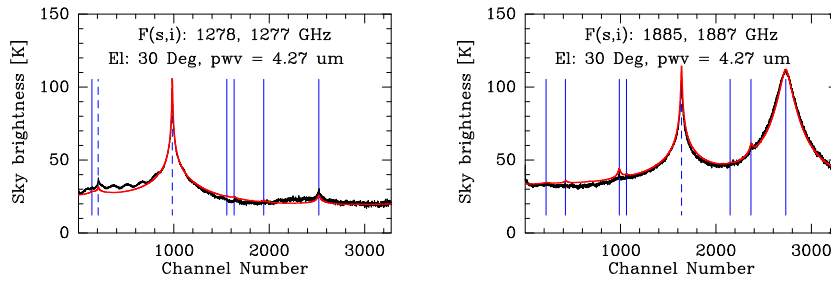


B.4.4 Scan 11715

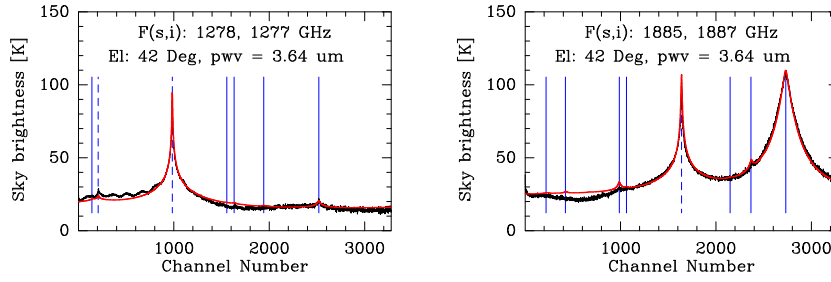


B.4.5 Scan 11716

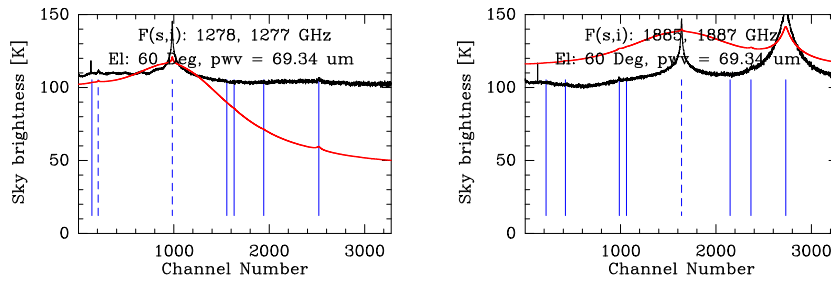
Figure B.5: Same as Figure B.4 but for GREAT Cycle-II Leg-9 atmospheric observations.



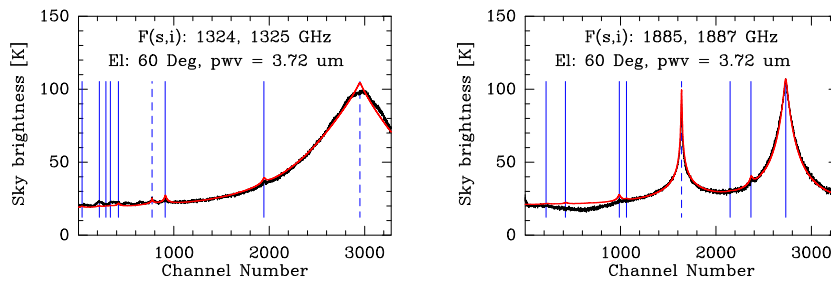
B.5.6 Scan 11717



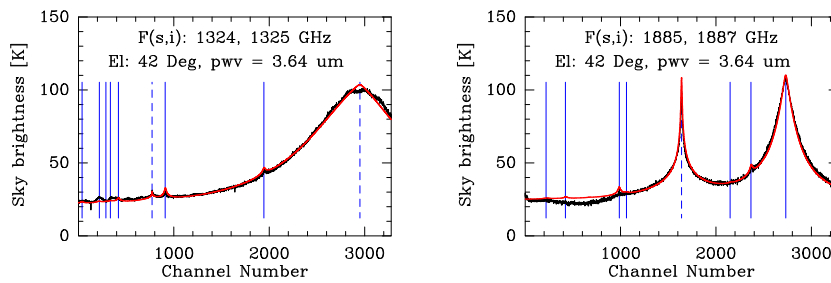
B.5.7 Scan 11718



B.5.8 Scan 11719

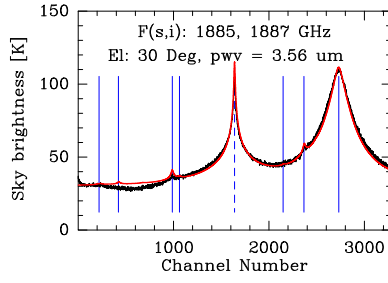
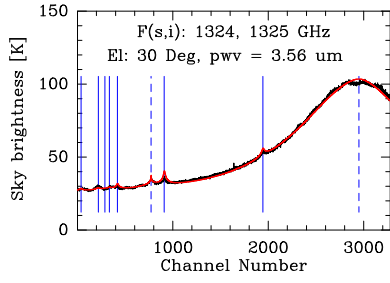


B.5.9 Scan 11720



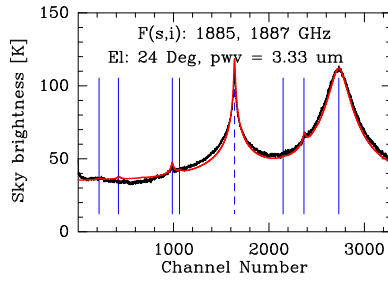
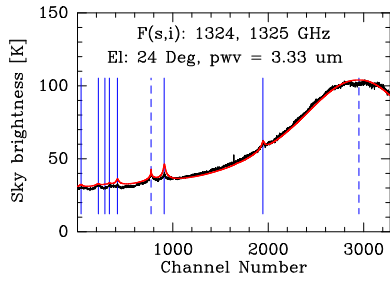
B.5.10 Scan 11721

Figure B.5: Continued.

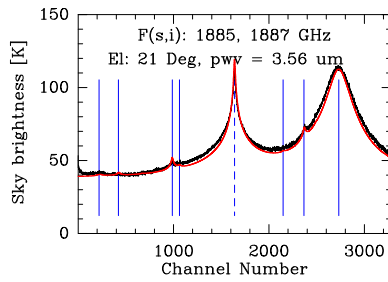
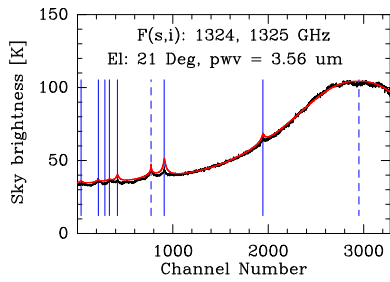


B.5.11 Scan 117122

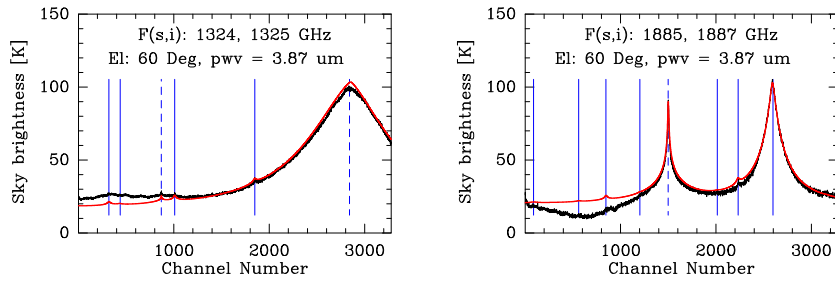
Figure B.5: Continued.



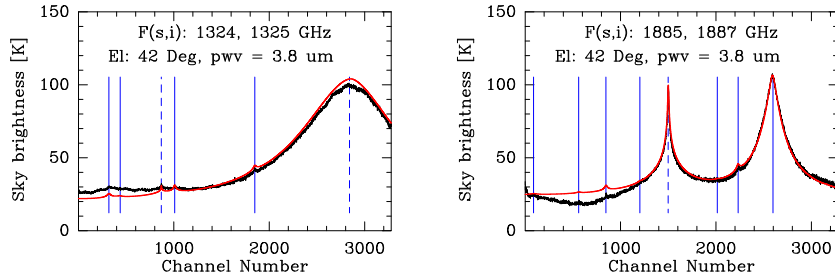
B.5.12 Scan 11723



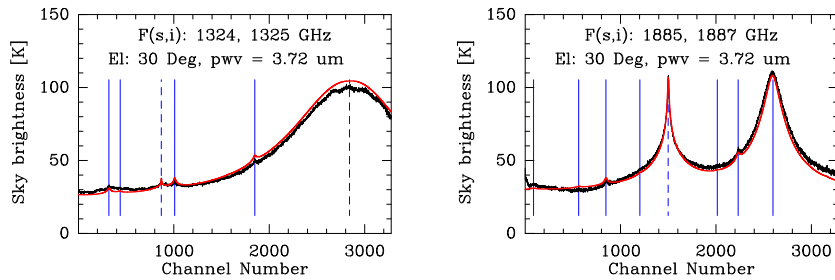
B.5.13 Scan 11724



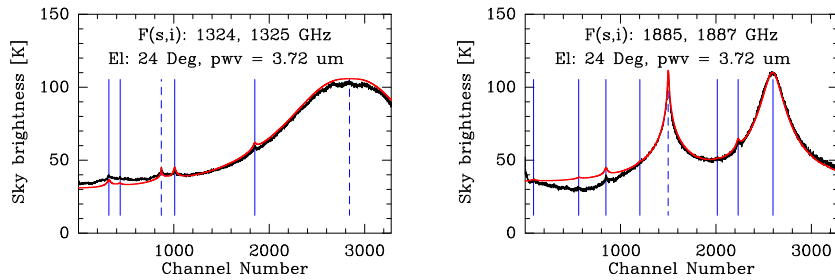
B.6.1 Scan 11917



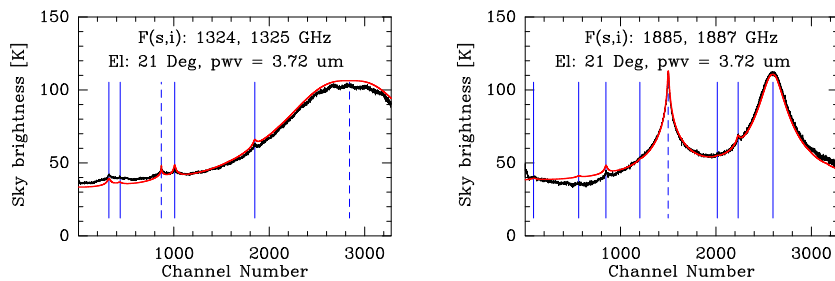
B.6.2 Scan 11918



B.6.3 Scan 11919

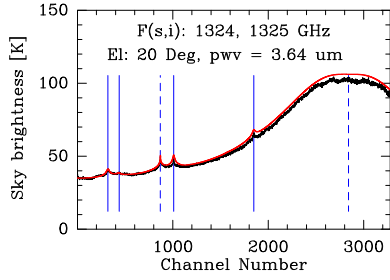


B.5.4 Scan 11920



B.5.5 Scan 11921

Figure B.6: Same as Figure B.4 but for GREAT Cycle-II Leg-11 atmospheric observations.



B.6.6 Scan 11922

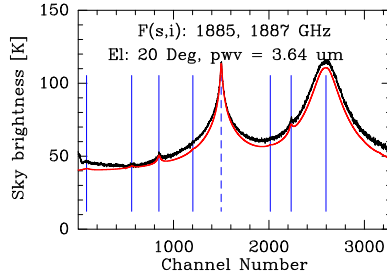
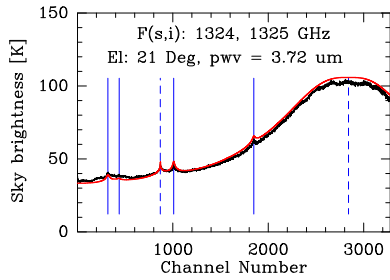
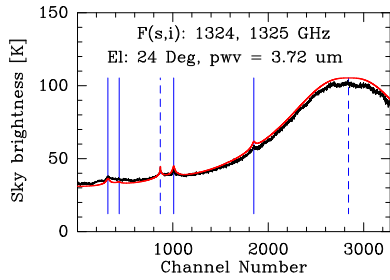
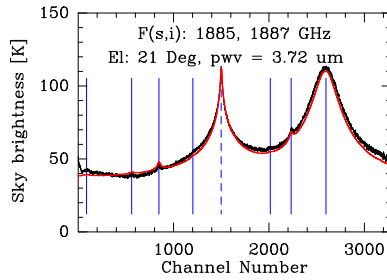


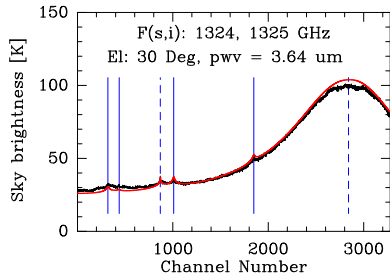
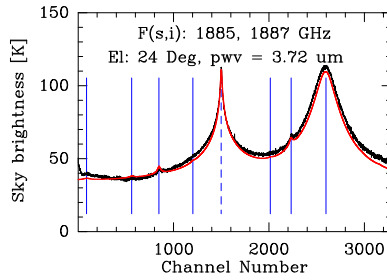
Figure B.6: Continued.



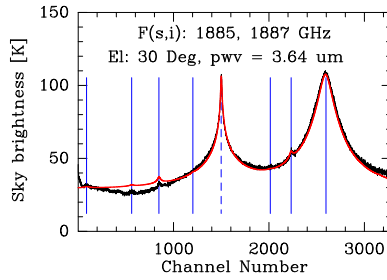
B.6.7 Scan 11923

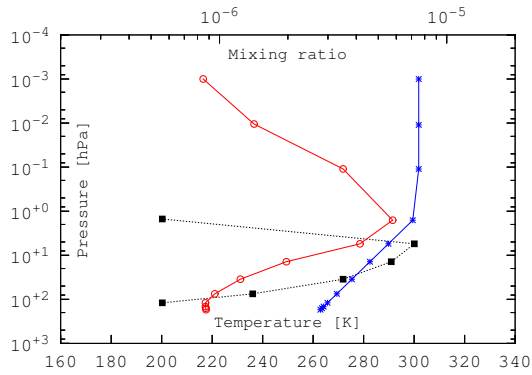


B.6.8 Scan 11924

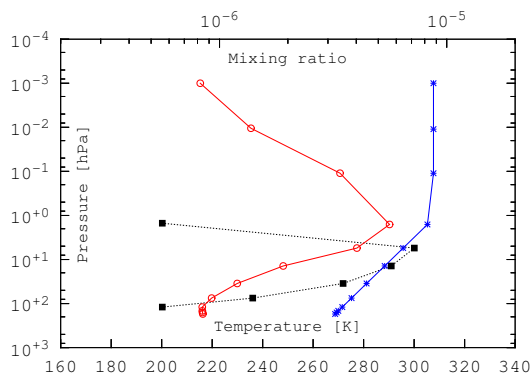


B.6.9 Scan 11925

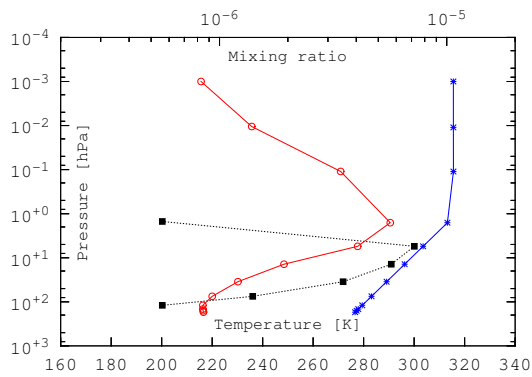




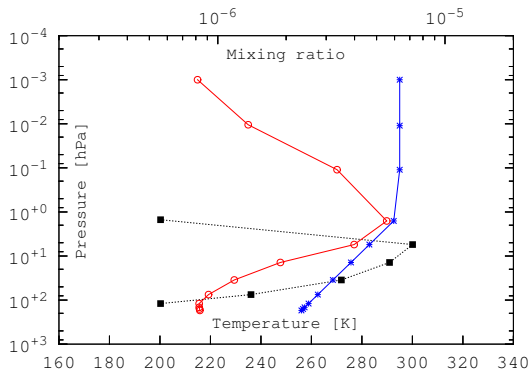
B.7.1 Scan 7516



B.7.2 Scan 7517

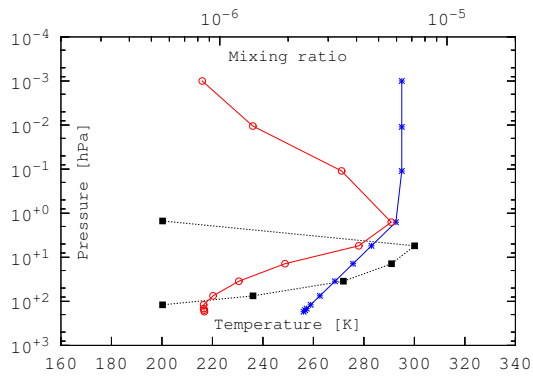


B.7.3 Scan 7518



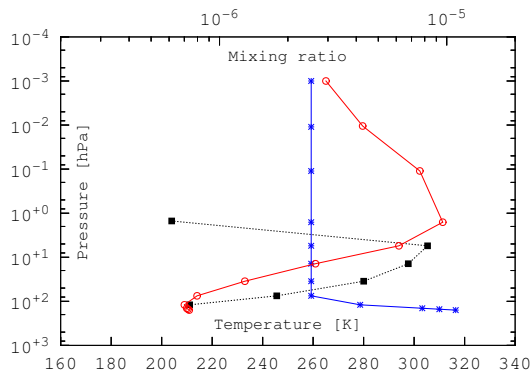
B.7.4 Scan 7519

Figure B.7: Fitted model parameters of GREAT Cycle-I Leg-2 atmospheric observations. The legends are the same as in Figure 6.7.

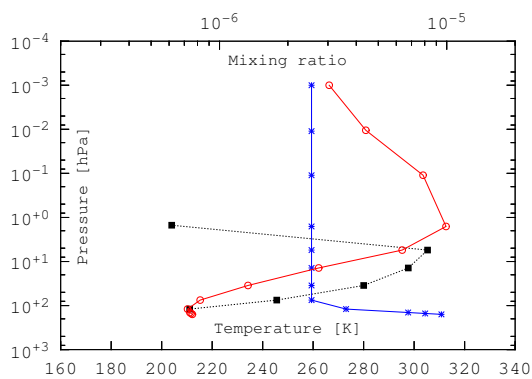


B.7.5 Scan 7520

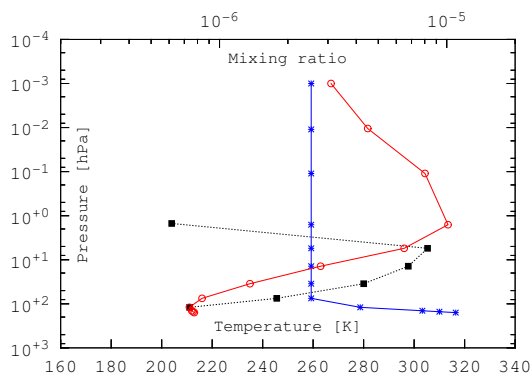
Figure B.7: Continued.



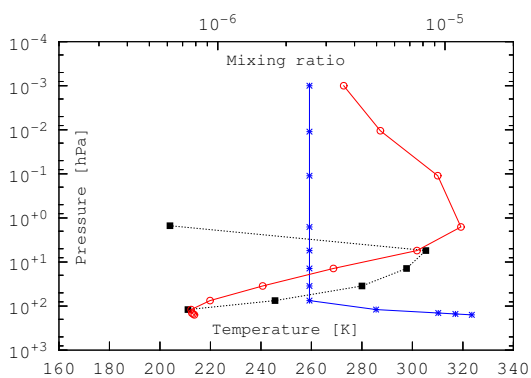
B.8.1 Scan 11711



B.8.2 Scan 11712



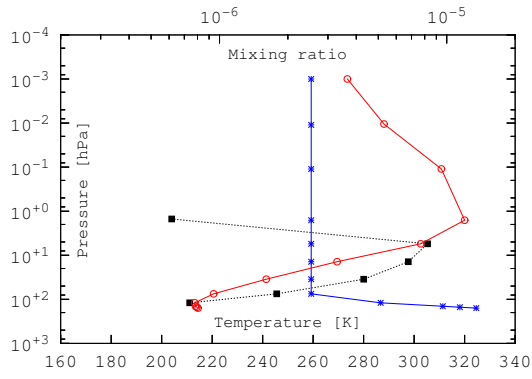
B.8.3 Scan 11713



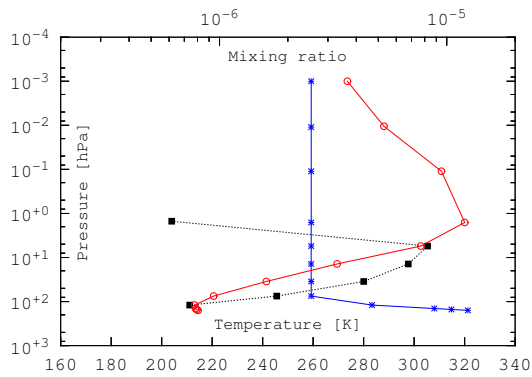
B.8.4 Scan 11715

Figure B.8: Same as Figure B.7 but for GREAT Cycle-II Leg-9 atmospheric observations. Scan 11719 is omitted because the fitted parameters are meaningless due to the hardware malfunction during the observation, as explained on page 79. The fitted parameters may have large errors especially in the mesosphere.

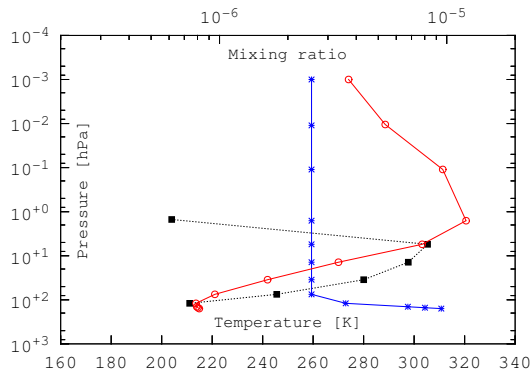
Figure B.8: Continued.



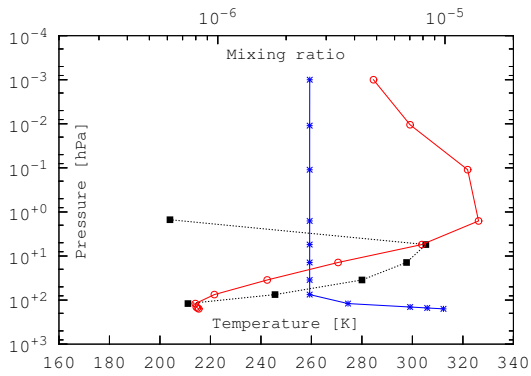
B.9.1 Scan 11716



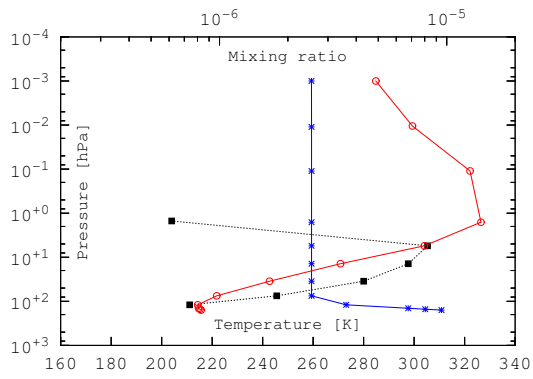
B.9.2 Scan 11717



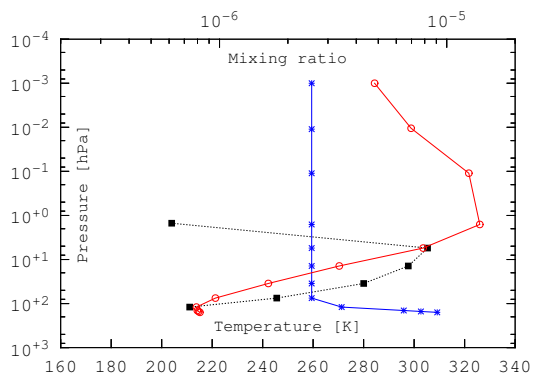
B.9.3 Scan 11718



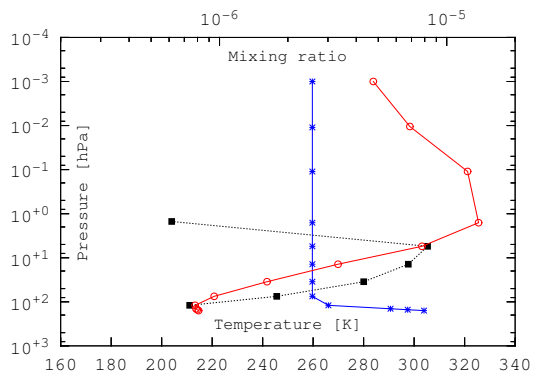
B.9.4 Scan 11720



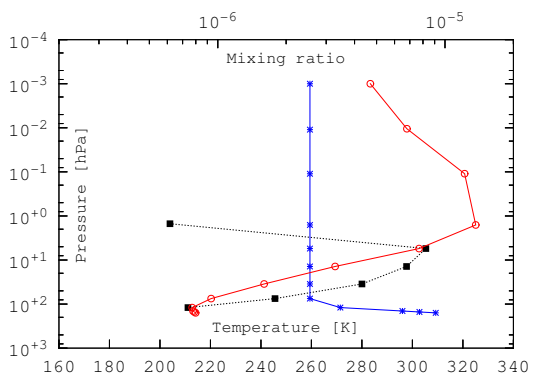
B.8.5 Scan 11721



B.8.6 Scan 11722

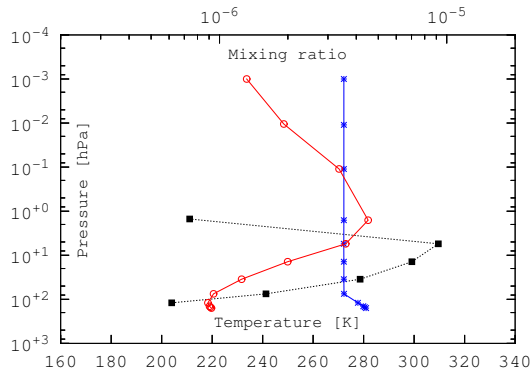


B.8.7 Scan 11723

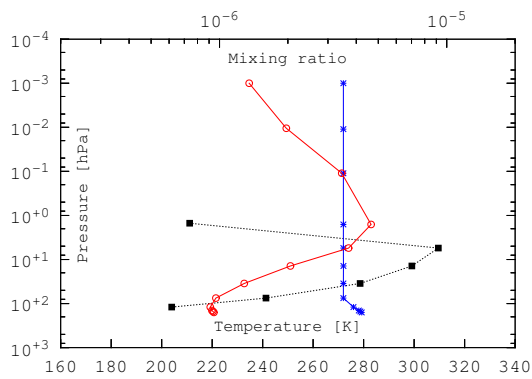


B.8.8 Scan 11724

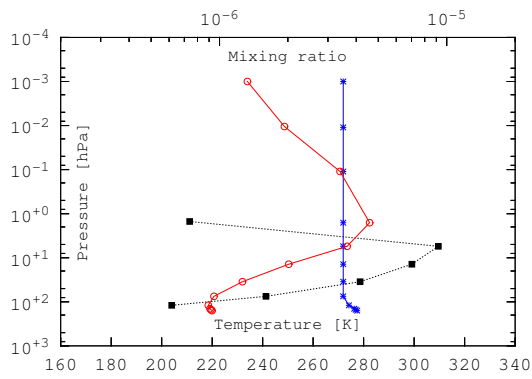
Figure B.8: Continued.



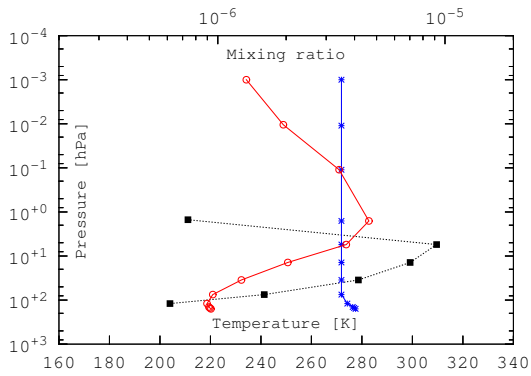
B.9.1 Scan 11917



B.9.2 Scan 11918

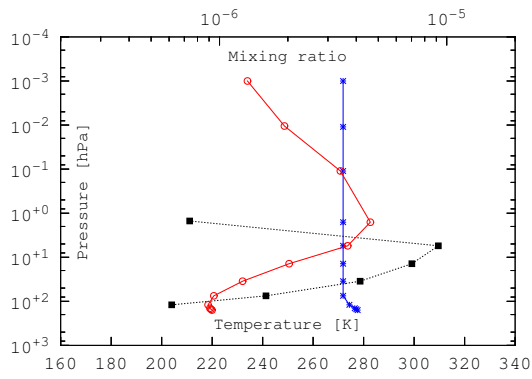


B.9.3 Scan 11919

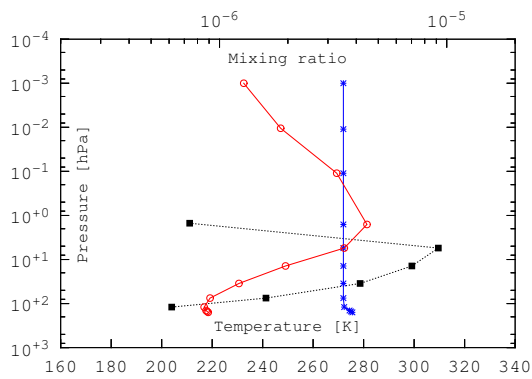


B.9.4 Scan 11920

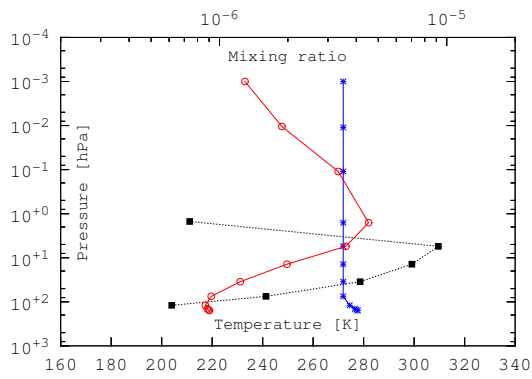
Figure B.9: Same as Figure B.7 but for Cycle-II Leg-11 atmospheric observations.



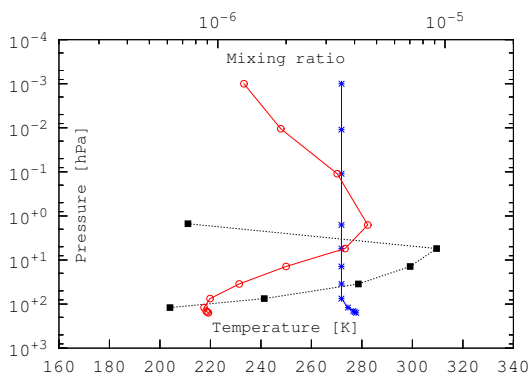
B.9.5 Scan 11921



B.9.6 Scan 11922



B.9.7 Scan 11923



B.9.8 Scan 11924

Figure B.9: Continued.

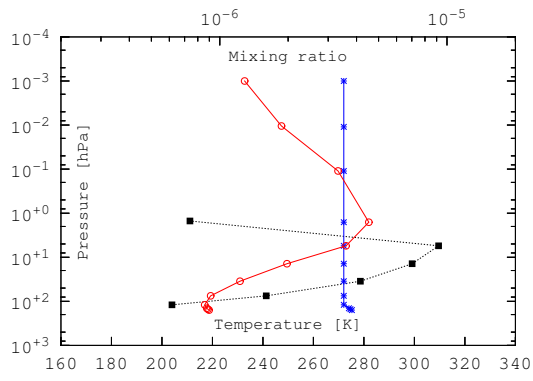


Figure B.9: Continued.

B.9.9 Scan 11925



# C

## Program structure of *kalibrate*

This chapter is intended to serve as a start-up guide for new developers of *kalibrate*. The calibration tool of *KOSMA-Software*, *kalibrate*, is open source software. The source code is available from the CVS repository<sup>1</sup> on request to I. Physikalisches Institut der Universität zu Köln. The *kalibrate* program is written in a self-documented style. The code is standardized on C++98, Python 2.x, and the GNU dialect of Fortran 77.

The Fortran code is under the *libkefeng* and *libhiyama* subdirectories, and contains the legacy implementations of using the *atmtable* for atmospheric modeling, which has been implemented before, and has been extended by this thesis work to make use of multi-processing with OpenMP. The rest of the program is implemented in C++. The C++ procedures and data structures are exposed to Python via related interface functions in *script.cpp* and *fits\_io.cpp* in the *kalibrate* subdirectory. The system-wide configuration file of *kalibrate* is *kalibrate.rc*. This file is written in Python and executed by *kalibrate* on start-up. The system-wide configuration file executes the user specific configuration file, *\$HOME/.kalibraterc*, and the local configuration file, *\$PWD/.kalibraterc*<sup>2</sup> in turn. The modular structure of *kalibrate* is shown in Figure C.1.

<sup>1</sup> The descriptions here apply to the 30th of November 2015 snapshot of the *mpi* branch of *kalibrate*, which can be checked out by running “*cvs update -D 2015-11-30 -r mpi -d*” under the top level directory of the *kalibrate* source tree.

<sup>2</sup> *\$HOME* is the home directory, and *PWD* is the current working directory of *kalibrate*.

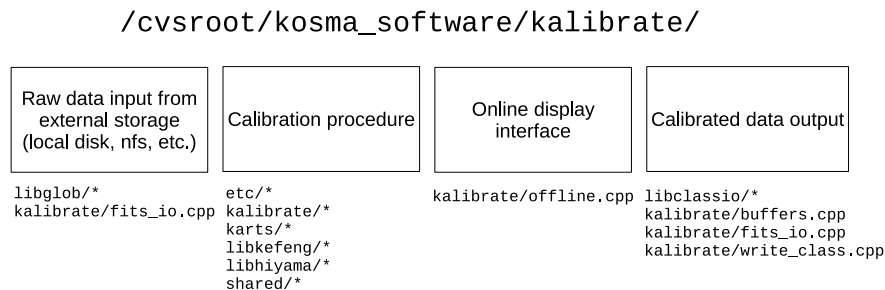


Figure C.1: Overall structure of *kalibrate*.

The functional part “calibration procedure” in Figure C.1 contains

the implementation of the method in Chapters 2 and 3. Its detailed structure (callgraph) is shown in Figure C.2. Because the radiative transfer model is compute intensive, it is possible to offload the computation to a server machine that also has *kalibrate* installed through the Message Passing Interface (MPI).

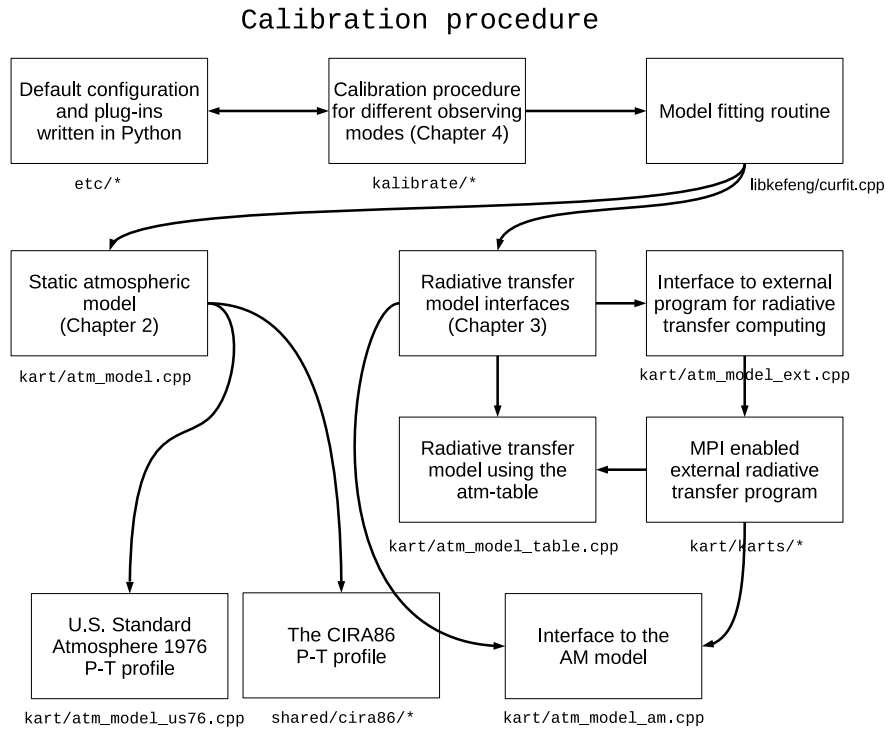


Figure C.2: Detailed structure of the calibration procedure of *kalibrate*.

In order to do the calibration, the raw data must be read in, and the calibrated data must be written out. The procedure to select of the raw data files for the given scan can take up more than half of the running time of *kalibrate* is the files were selected using standard library function `glob(3)`. The *kalibrate* program uses a notification<sup>3</sup> driven, integer scan / subscan number to file name map to store the content of the raw data directory.

<sup>3</sup> The `inotify` mechanism is used if available. Otherwise, the full content of the raw data directory is reloaded each time the `offline_cal` function, which is the main loop of calibration, is called.

### Raw data input from external storage (local disk, nfs, etc.)

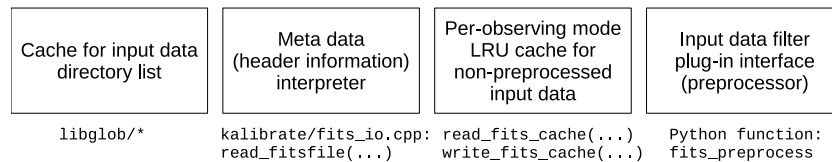


Figure C.3: Structure of the raw data input stage of *kalibrate*.

As shown in Figure C.3, the freshly read-in spectra and meta data (ambient pressure, telescope position, etc.) can be processed before fed into the calibration procedure. The raw data cache is used to reduced the overhead introduced by reading in the same LOAD scans and OFF measurements repeatedly.

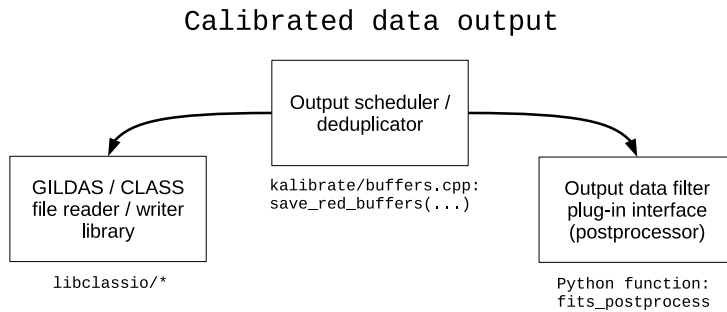


Figure C.4: Structure of the calibrated data output facility of *kalibrate*.

Similar as the preprocessor for raw data input, the observations can be postprocessed before being written into the GILDAS / CLASS file, as shown in Figure C.4. For guaranteed performance and stability of functionality, an internal library to write output data in the GILDAS / CLASS format is developed for *kalibrate*. This library, namely `libclassio`, also supports writing the SOFIA “user section (Pety et al., 2015)” that contains user defined meta data of the observation, including the static atmospheric model used for calibration, which can be retrieved from the CLASS data file via the correspond library routine in GILDAS / CLASS, which is also developed as part of this thesis, to read the SOFIA “user section”.



# D

## *OpenCL support of the AM atmospheric model*

When used to compute atmospheric transmission or sky brightness, the bottleneck of the AM model is the `linsum` function. The `linsum` function sums up the absorption coefficients of the spectral lines, i.e., it does not compute the collision induced absorption and the water continuum. The `linsum` function has been ported to OpenCL as part of this thesis work. The modified AM model is, like *kalibrate*, available from the *KOSMA-Software* CVS repository. Performance benchmarks of two computers are presented in this chapter.

### 1. Computer 1

CPU: Intel Core 2 Duo E7400; GPU: AMD/ATI R7 260X;  
gcc 4.8.4; AMD Catalyst 14.12, AMD APP SDK 2.9.1.

### 2. Computer 2

CPU: Intel E5-2640 × 2; gcc 4.8.2.

Tested configuration file (static atmospheric model) for AM:

```
f 1200 GHz 1400 GHz 1 MHz
za 0 deg
tol 0.0001
T0 2.7 K
PTmode Pbase Tbase
output f tau Trj
layer
Pbase 140 mbar
Tbase 210 K
lineshape Voigt-Kielkopf o3
column o3 hydrostatic 1.e-6
column n2air hydrostatic
column o2air hydrostatic
column o2 hydrostatic
column h2o 0.01 mm_pwv
```

Table D.1. AM benchmark: OpenCL vs. OpenMP

Computer	Tolerance	linesum time [s]	Total time [s]	Compute interface for linesum
1	0	935.4	941	OpenMP (CPU)
1	0	2.12	8.73	OpenCL (GPU)
2	0	30.15	31.12	OpenMP (CPU)
1	0.0001	130.5	136.1	OpenMP (CPU)
1	0.0001	1.11	7.80	OpenCL (GPU)
2	0.0001	4.51	5.29	OpenMP (CPU)

As shown in Table D.1, the speed up by using OpenCL GPU acceleration is significant. However, the performance gain will decrease when computing an atmospheric model that has many layers. This is due to the long latency of calling the GPU code. The problem can be solved by coalescence of the model layers before feeding the data to GPU code. This is future work.





# Bibliography

- Barnett, J. J. and Chandra, S. (1990). COSPAR International Reference Atmosphere grand mean. *Advances in Space Research*, 10:7.
- Bertie, J. E. and Lan, Z. (1996). Infrared intensities of liquids XX: The intensity of the OH stretching band of liquid water revisited, and the best current values of the optical constants of H<sub>2</sub>O(l) at 25 °C between 15,000 and 1 cm<sup>-1</sup>. *Applied Spectroscopy*, 50:1047.
- Boisssolesa, J., Bouletb, C., Tipping, R. H., et al. (2003). Theoretical calculation of the translation-rotation collision-induced absorption in N<sub>2</sub>-N<sub>2</sub>, O<sub>2</sub>-O<sub>2</sub>, and N<sub>2</sub>-O<sub>2</sub> pairs. *Journal of Quantitative Spectroscopy and Radiative Transfer*, 82:505.
- Borysow, A. and Frommhold, L. (1986). Collision-induced rototranslational absorption spectra of N<sub>2</sub>-N<sub>2</sub> pairs for temperatures from 50 to 300 K. *Astrophysical Journal*, 311:1043.
- Borysow, A. and Frommhold, L. (1987). Collision-induced rototranslational absorption spectra of N<sub>2</sub>-N<sub>2</sub> pairs for temperatures from 50 to 300 K: Erratum. *Astrophysical Journal*, 320:437.
- Brewer, A. W. (1949). Evidence for a world circulation provided by the measurements of helium and water vapour distribution in the stratosphere. *Quarterly Journal of the Royal Meteorological Society*, 75:351.
- Buck, A. L. (1981). New Equations for Computing Vapor Pressure and Enhancement Factor. *Journal of Applied Meteorology*, 20(12):1527.
- Callies, J., Corpaccioli, E., Eisinger, M., et al. (2000). GOME-2 – Metop's Second Generation sensor for Operational Ozone Monitoring. ESA Bulletin.
- Carter, M., Lazareff, B., Maier, D., et al. (2012). The EMIR multi-band mm-wave receiver for the IRAM 30-m telescope. *Astronomy & Astrophysics*, 538:89.
- Disterhoft, P., Kiedron, P., and Stierle, S. (2008). NOAA-EPA UV and Ozone Monitoring Network: NEUBrew. In *Quadrennial Ozone Symposium, Tromso, Norway*.
- Dobson, G. M. B. (1956). Origin and Distribution of the Polyatomic Molecules in the Atmosphere. *Proceedings of the Royal Society of London. Series A*, 236:187.
- Downes, D. (1989). *Radio Astronomy Techniques*. IRAM Grenoble.
- Dupuy, É., Urban, J., Ricaud, P., et al. (2004). Strato-mesospheric measurements of carbon monoxide with the Odin Sub-Millimetre Radiometer: Retrieval and first results. *Geophysical Research Letters*, 21:20101.

- Fabian, P., Borchers, R., Weiler, K. H., et al. (1979). Simultaneously measured vertical profiles of H<sub>2</sub>, CH<sub>4</sub>, CO, N<sub>2</sub>O, CFCl<sub>3</sub>, and CF<sub>2</sub>Cl<sub>2</sub> in the mid-latitude stratosphere and troposphere. *Journal of Geophysical Research*, 84:3149.
- Forkman, P., Christensen, O. M., Eriksson, P., et al. (2012). Six years of mesospheric CO estimated from ground-based frequency-switched microwave radiometry at 57° N compared with satellite instruments. *Atmospheric Measurement Techniques*, 5:2827.
- Gehrz, R. D. and Becklin, E. E. (2010). The Stratospheric Observatory for Infrared Astronomy (SOFIA). In *21st International Symposium on Space Terahertz Technology*, page 18.
- Graf, U. U., Honingh, C. E., Jacobs, K., et al. (2008). Upgrade of the SMART Focal Plane Array Receiver for NANTEN2. In *19th International Symposium on Space Terahertz Technology*, page 488.
- Graf, U. U., Honingh, C. E., Jacobs, K., and Stutzki, J. (2015). Terahertz Heterodyne Array Receivers for Astronomy. *Journal of Infrared, Millimeter, and Terahertz Waves*, 36:896.
- Guan, X., Stutzki, J., Graf, U. U., et al. (2012). GREAT/SOFIA atmospheric calibration. *Astronomy & Astrophysics*, 542:L4.
- Harries, J. E., Russell, J. M., Tuck, A. F., et al. (1996). Validation of measurements of water vapor from the Halogen Occultation Experiment (HALOE). *Journal of Geophysical Research (Atmosphere)*, 101:10205.
- Herbin, H., Hurtmans, D., Clerbaux, C., et al. (2009). H<sub>2</sub><sup>16</sup>O and HDO measurements with IASI/MetOp. *Atmospheric Chemistry and Physics*, 9:9433.
- Heyminck, S., Graf, U. U., Güsten, R., et al. (2012). GREAT: the SOFIA high-frequency heterodyne instrument. *Astronomy & Astrophysics*, 542:L1.
- Hiyama, S. (1998). Seitenbandkalibration Radioastronomischer Linienbeobachtungen.
- Hoffmann, C. G., Raffalski, U., Palm, M., et al. (2011). Observation of strato-mesospheric CO above Kiruna with ground-based microwave radiometry - retrieval and satellite comparison. *Atmospheric Measurement Techniques*, 4:2389.
- Kawamura, A., Mizuno, N., Yonekura, Y., et al. (2005). NANTEN2: A Submillimeter Telescope for Large Scale Surveys at Atacama. In *Symposium of the International Astronomical Union*, page 275.
- Kielkopf, J. F. (1973). New approximation to the Voigt function with applications to spectral-line profile analysis. *Journal of Optics Soc. America*, 63:987.
- Klein, R., Poglitsch, A., Raab, W., et al. (2006). FIFI LS: the far-infrared integral field spectrometer for SOFIA. In *Proc. SPIE 6269, Ground-based and Airborne Instrumentation for Astronomy*.
- Kutner, M. L. and Ulich, B. L. (1981). Recommendations for calibration of millimeter-wavelength spectral line data. *Astrophysical Journal*, 250:341.
- Lobanov, Y., Tong, C., Blundell, R., et al. (2009). A Study of Direct Detection Effect on the Linearity of Hot Electron Bolometer Mixers. In *20th International Symposium on Space Terahertz Technology*, page 282.
- Lord, S. D. (1992). A New Software Tool for Computing Earth's Atmospheric Transmission of Near- and Far-Infrared Radiation. NASA-TM-103957.

- Lovas, F. J. (2004). NIST Recommended Rest Frequencies for Observed Interstellar Molecular Microwave Transitions-2002 Revision. *Journal of Physical and Chemical Reference Data*, page 177.
- Masterbrook, H. J. (1968). Water Vapor Distribution in the Stratosphere and High Troposphere. *Journal of Atmospheric Sciences*, 25:299.
- Müller, H. S. P., Schlöder, F., Stutzki, J., and Winnewisser, G. (2005). The Cologne Database for Molecular Spectroscopy, CDMS: a useful tool for astronomers and spectroscopists. *Journal of Molecular Structure*, 742:215.
- Müller, H. S. P., Thorwirth, S., Roth, D. A., and Winnewisser, G. (2001). The Cologne Database for Molecular Spectroscopy, CDMS. *Astronomy & Astrophysics*, 370:L49.
- NASA (1976). U.S. Standard Atmosphere, 1976. NASA-TM-X-74335.
- Orsolini, Y. J., Urban, J., Murtagh, D. P., et al. (2010). Descent from the polar mesosphere and anomalously high stratopause observed in 8 years of water vapor and temperature satellite observations by the Odin Sub-Millimeter Radiometer. *Journal of Geophysical Research (Atmospheres)*, 115:12305.
- Paine, S. (2014). The *am* atmospheric model. SMA technical memo #152.
- Pardo, J. R., Cernicharo, J., and Serabyn, E. (2001). Atmospheric Transmission at Microwaves (ATM): An Improved Model for Millimeter/Submillimeter Applications. *IEEE Transactions on Antennas and Propagation*, 49:1683.
- Pascale, E. (2012). The Balloon-borne Large Aperture Submillimetre Telescope (BLAST) and BLASTPol. *IAU Symposium*, 288:154.
- Pety, J., Bardeau, S., Guilloteau, S., et al. (2015). GILDAS. <http://www.iram.fr/IRAMFR/GILDAS>.
- Picone, J. M., Hedin, A. E., Drob, D. P., and Aikin, A. C. (2002). NRLMSISE-00 empirical model of the atmosphere: Statistical comparisons and scientific issues. *Journal of Geophysical Research (Space Physics)*, 107:1468.
- Planesas, P. (2013). The Joint ALMA Observatory: brief history and first scientific results. In *Highlights of Spanish Astrophysics VII*.
- Pumphrey, H. C., Filipiak, M. J., Livesey, N. J., et al. (2007). Validation of middle-atmosphere carbon monoxide retrievals from the Microwave Limb Sounder on Aura. *Journal of Geophysical Research (Atmospheres)*, 112:24S38.
- Pütz, P., Buchel, D., Honingh, C., et al. (2013). Hot electron bolometer waveguide mixers up to 4.7 THz for the upGREAT focal plane array receiver on SOFIA. In *38th International Conference on Infrared, Millimeter, and Terahertz Waves*.
- Radiometer-Physics GmbH (2011). *RPG-XFFTS eXtended bandwidth Fast Fourier Transform Spectrometer Technical Specification*.
- Randel, W. J., Wu, F., Vömel, H., et al. (2006). Decreases in stratospheric water vapor after 2001: Links to changes in the tropical tropopause and the Brewer-Dobson circulation. *Journal of Geophysical Research (Atmospheres)*, 111:12312.

- Revathy, K., Prabhakaran Nayar, S. R., and Krishna Murthy, B. V. (2001). Diurnal variation of tropospheric temperature at a tropical station. *Annales Geophysicae*, 19:1001.
- Rezac, L., Hartogh, P., Güsten, R., et al. (2015). First detection of the 63  $\mu\text{m}$  atomic oxygen line in the thermosphere of Mars with GREAT/SOFIA. *Astronomy & Astrophysics*, 580:L10.
- Rothman, L. S., Gordon, I. E., Barbe, A., et al. (2009). The HITRAN 2008 molecular spectroscopic database. *Journal of Quantitative Spectroscopy and Radiative Transfer*, 110:533.
- Russell, James M., I., Gordley, L. L., Park, J. H., et al. (1993). The Halogen Occultation Experiment. *Journal of Geophysical Research*, 98:10777.
- Ruzmaikin, A., Lee, J. N., and Wu, D. L. (2014). Patterns of carbon monoxide in the middle atmosphere and effects of solar variability. *Advances in Space Research*, 54:320.
- Schneider, N., Urban, J., and Baron, P. (2009). Potential of radiotelescopes for atmospheric line observations: I. Observation principles and transmission curves for selected sites. *Planetary and Space Science*, 57:1419.
- Sebring, T. A., Giovanelli, R., Radford, S., et al. (2006). Cornell Caltech Atacama Telescope (CCAT): a 25-m aperture telescope above 5000-m altitude. *SPIE*, 6267:75.
- Sims, G., Ashley, M. C. B., Cui, X., et al. (2012). Precipitable Water Vapor above Dome A, Antarctica, Determined from Diffuse Optical Sky Spectra. *Publications of the Astronomical Society of the Pacific*, 124:74.
- Steinbrecht, W., Claude, H., Schönborn, F., et al. (2006). Long-term evolution of upper stratospheric ozone at selected stations of the Network for the Detection of Stratospheric Change (NDSC). *Journal of Geophysical Research (Atmospheres)*, 111:10308.
- Strong, K., Wolff, M. A., Kerzenmacher, T. E., et al. (2008). Validation of ACE-FTS  $\text{N}_2\text{O}$  measurements. *Atmospheric Chemistry and Physics*, 8:4759.
- Taylor, F. W., Dudhia, A., and Rodgers, C. D. (1996). Reference model for methane and nitrous oxide. *Advances in Space Research*, 18:91.
- Tremblin, P., Schneider, N., Minier, V., et al. (2012). Worldwide site comparison for submillimetre astronomy. *Astronomy & Astrophysics*, 548:A65.
- Urban, J., Baron, P., Lautié, N., et al. (2004). Moliere (v5): a versatile forward- and inversion model for the millimeter and sub-millimeter wavelength range. *Journal of Quantitative Spectroscopy and Radiative Transfer*, 83:529.
- von Zahn, U., Fiedler, J., Naujokat, B., et al. (1998). A note on record-high temperatures at the northern polar stratopause in winter 1997/98. *Geophysical Research Letters*, 25:4169.
- Wang, P. H., Cunnold, D. M., Treppe, C. R., et al. (2006). Ozone variability in the midlatitude upper troposphere and lower stratosphere diagnosed from a monthly SAGE II climatology relative to the tropopause. *Journal of Geophysical Research (Atmospheres)*, 111:21304.
- Warren, S. G. and Brandt, R. E. (2008). Optical constants of ice from the ultraviolet to the microwave: A revised compilation. *Journal of Geophysical Research (Atmospheres)*, 113:14220.

Wells, D. C., Greisen, E. W., and Harten, R. H. (1981). FITS - a Flexible Image Transport System. *Astronomy & Astrophysics Supplement*, 44:363.

World Meteorological Organization (2014). Scientific Assessment of Ozone Depletion: 2014.

# Erklärung

Ich versichere, dass ich die von mir vorgelegte Dissertation selbstständig angefertigt, die benutzten Quellen und Hilfsmittel vollständig angegeben und die Stellen der Arbeit – einschließlich Tabellen, Karten und Abbildungen –, die anderen Werken im Wortlaut oder dem Sinn nach entnommen sind, in jedem Einzelfall als Entlehnung kenntlich gemacht habe; dass diese Dissertation noch keiner anderen Fakultät oder Universität zur Prüfung vorgelegen hat; dass sie – abgesehen von unten angegebenen Teilpublikationen – noch nicht veröffentlicht worden ist sowie, dass ich eine solche Veröffentlichung vor Abschluss des Promotionsverfahrens nicht vornehmen werde.

Die Bestimmungen der Promotionsordnung sind mir bekannt. Die von mir vorgelegte Dissertation ist von Prof. Dr. Jürgen Stutzki betreut worden.

Nachfolgend genannte Teilpublikationen liegen vor:

Guan, X.; Stutzki, J.; Graf, U. U.; Güsten, R.; Okada, Y.; Requena-Torres, M. A.; Simon, R.; Wiesemeyer, H. *GREAT/SOFIA atmospheric calibration*, *Astronomy & Astrophysics*, 542, L4

Ich versichere, dass ich alle Angaben wahrheitsgemäß nach bestem Wissen und Gewissen gemacht habe und verpflichte mich, jedmögliche, die obigen Angaben betreffenden Veränderungen, dem Dekanat unverzüglich mitzuteilen.

# Lebenslauf

Name, Vorname: Guan, Xin  
Geburtstag: 1981-05-29  
Geburtsort: Beijing  
Staatsangehörigkeit: chinesisch

Schulbildung:	ISCED 2011	Bildungssystem in Deutschland	Dauer
	Level 1	Grundschule	1987 ~ 1993
	Level 2	<i>nicht definiert</i>	1993 ~ 1996
	Level 3	<i>nicht definiert</i>	1996 ~ 1999

Studium:	Universtät	Institut / Grad	Dauer / Zeitpunkt
	Tsinghua University	Dept. Electrical Engineering / Bachelor of Engineering	1999 ~ 2003 2003
	Peking University	School of Physics / Master of Science	2004 ~ 2007 2008
	Universtät zu Köln	I. Physikalisches Institut	Beginn dieser Arbeit 2009